SURFACE PROPERTIES OF ADVANCED MATERIALS AND THEIR

APPLICATIONS IN BALLISTICS

A Thesis

by

HUISUNG YUN

Submitted to the Office of Graduate Studies of
Texas A&M University
in partial fulfillment of the requirements for the degree of

MASTER OF SCIENCE

August 2010

Major Subject: Mechanical Engineering

SURFACE PROPERTIES OF ADVANCED MATERIALS AND THEIR

APPLICATIONS IN BALLISTICS

A Thesis

by

HUISUNG YUN

Submitted to the Office of Graduate Studies of
Texas A&M University
in partial fulfillment of the requirements for the degree of

MASTER OF SCIENCE

Approved by:

Chair of Committee,	Hong Liang
Committee Members,	Ramesh Talreja
	Xinghang Zhang
Head of Department,	Dennis O'Neal

August 2010

Major Subject: Mechanical Engineering

ABSTRACT

Surface Properties of Advanced Materials and Their Applications in Ballistics.

(August 2010)

Huisung Yun, B.E., Korea Military Academy

Chair of Advisory Committee: Dr. Hong Liang

This thesis research investigates the surface properties and performances of gold nanoparticles, microarc oxidation coating, and epitaxial nano-twinned copper film. The research aims to understand the critical behavior of material surfaces in order to facilitate design and development of new materials for tribological applications. The research will focus on improving of the gun barrel performances. Experimental approaches will be used for combining analysis with basic thermal energy transfer principles. Results obtained here will be used for developing new materials to be used in facilitating gun barrels.

Experimental approach includes scanning calorimetry-thremogravimetric analysis, tribological testing, and potentiodynamic polarization.

The fundamental understanding obtained here will be beneficial for the gun barrel design, manufacturing, and military technologies followed by the results of experiments with different three types of materials.

The results of this research showed that the coatings with microarc oxidation and nano-twinned structure improved wear resistance from the tribological examinations and size of AuNPs affected their thermal behaviors measured by differential scanning calorimetry and thermogravimetric analysis method.

DEDICATION

To my mother country and my family

ACKNOWLEDGEMENTS

TABLE OF CONTENTS

LIST OF FIGURES

Page

Page

LIST OF TABLES

Page

CHAPTER I

INTRODUCTION

This chapter introduces basics needed for the present research. To describe the importance and application of the research, ballistics will be explained to show the behaviors of a projectile. A projectile, which has gyroscopic stabilization, is described in terms of interior, exterior, and terminal ballistics. A gun barrel is one of the most important parts of a launching weapon assembly that determines the projectile behavior. The gun barrel determines the projectile's initial conditions such as velocity and launching direction. Here, the gun barrel's failure mechanisms are summarized and tribological principles involved in the same is discussed. At the end, advanced materials that are potentially beneficial for the mentioned failure are suggested.

1.1. Ballistics

Ballistics is the study of projectile behavior. Ballistics is used in designing guns and other launching weapons. This study is classified into three categories: interior, exterior, and terminal ballistics [1-3]. There are two kinds of projectiles which have no self propulsion; fin stabilized projectile, and gyroscopic motion stabilized projectile [4-6]. Here, the three categories of ballistics are explained by the projectile that is stabilized

_____

This thesis follows the style of Wear.

by the gyroscopic motion because the projectile is usually used for small arms to howitzers.

1.1.1. Interior ballistics

Interior ballistics interprets the projectile's behavior in a weapon's launching system [7]. **Fig.1-1** illustrates the schematic description of a projectile launching system. When ammunition is loaded and the breechblock closes the breech, the ammunition is ready to be fired. As the pounder in the breechblock hits the percussion cap, sensitive gunpowder inside the primer ignites. The flame formed from the ignition connects to the explosion of the propellant, which is charged in the cartridge. The explosion generates high pressure caused by gas and the cartridge extends to meet the wall of breech and breechblock. The pressure starts to accelerate the projectile the same manner that a car engine's piston is pushed by the fuel's explosion. During the acceleration of the projectile, rifling forces the projectile's surface to be worn and indented. Then, the rifling forces the projectile to rotate along the axis of the projectile's launching direction. The worn surface and indentation of a projectile is compared to the non-fired projectile in **Fig.1-2** and **1-3**. At the point the projectile evades from the end of the gun barrel, muzzle blast and vibration of the gun barrel affect the projectile's behaviors [8-11].
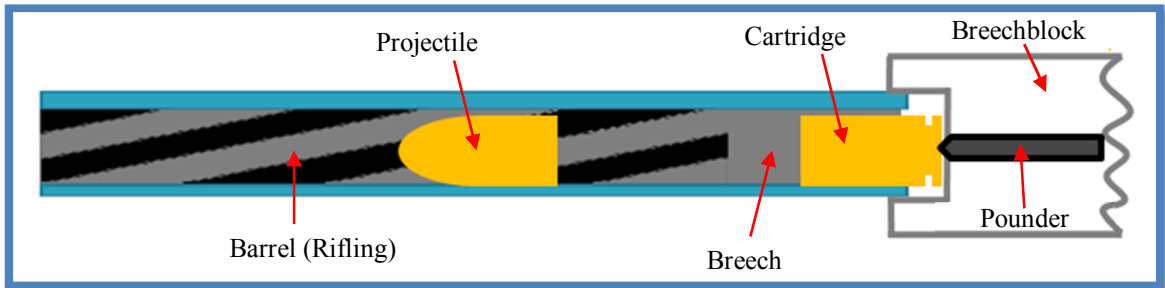
Fig.1-1. Schematic description of a projectile launching assembly.
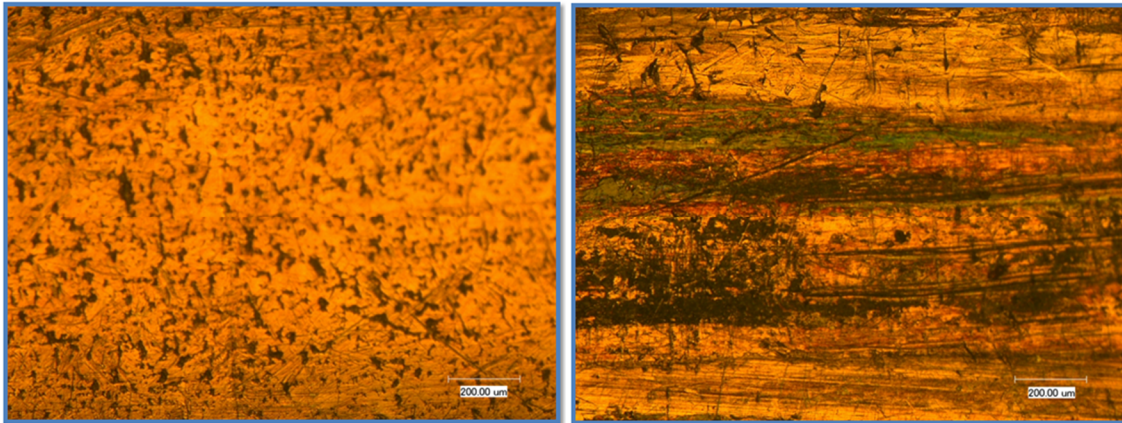
Fig.1-2. Projectiles' surface comparison. The optical micrograph of the right shows the worn surface compared to the non-fired projectile's surface (left). The projectile is 9×19 mm parabellum ammunition. The ammunition was fired by a Glock 17 handgun. The micrographs were taken by a Keyence VHX-600K optical microscope with 200 magnification.
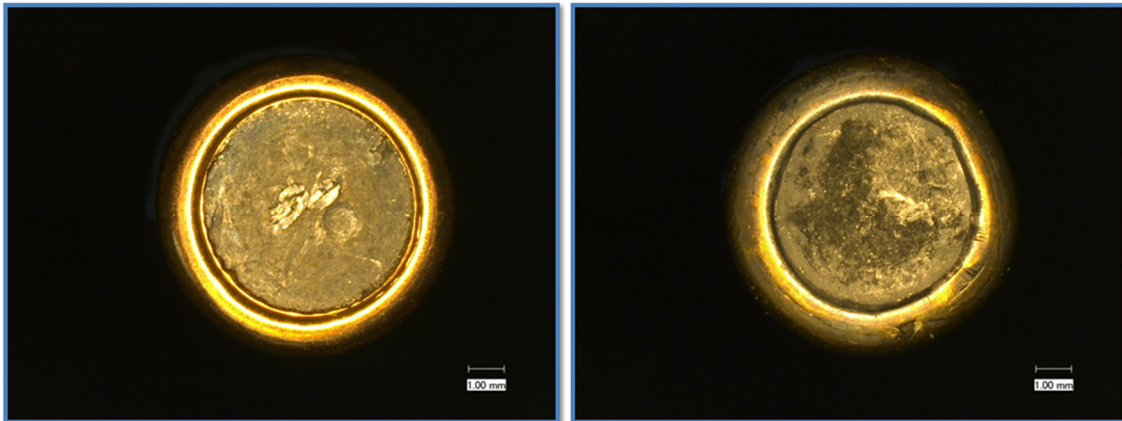
Fig.1-3. Projectiles' micrographs taken from the rear. The micrograph of the left shows the boundary between lead shaft and the brass cap is circular. However, the projectile after firing (right) shows extortion caused by the experience from the gun barrel's rifling. The projectile is 9×19 mm parabellum ammunition. The ammunition was fired by a Glock 17 handgun. The micrographs were taken by a Keyence VHX-600K optical microscope with 20 magnification.

1.1.2. Exterior ballistics

Exterior ballistics explains a projectile's behavior in the flying medium such as air or water [12]. This describes the trajectory considering the gravitational field and the medium's drag force, etc. The projectile's stabilization motion is considered in exterior ballistics as well as the trajectory of the projectile. The rotational motion, imposed by the gun barrel's rifling, stabilizes the projectile's pose in the flying medium [6]. **Fig.1-4** illustrates the free body diagram of a projectile in the flying medium. There are two force factors having different acting points in general: a center of pressure (CP) and a center of weight (CW). The center of pressure is the point of pressure caused by the medium's drag force, and the center of weight is the projectile's center of mass. When a CP is positioned in front of a CW as shown in **Fig.1-4**, the moment, which causes the projectile's nose to be turned backward, is generated. Once the projectile is turned

backward, the drag force increases dramatically and the trajectory of the projectile becomes unstable. To address this problem, the angular motion caused by the barrel's rifling is adopted. By combining the translational and the angular motion, the projectile's motion is described as a precessional motion as described in **Fig.1-5**. The center of the precession **C** can be located either inside or outside of the projectile.
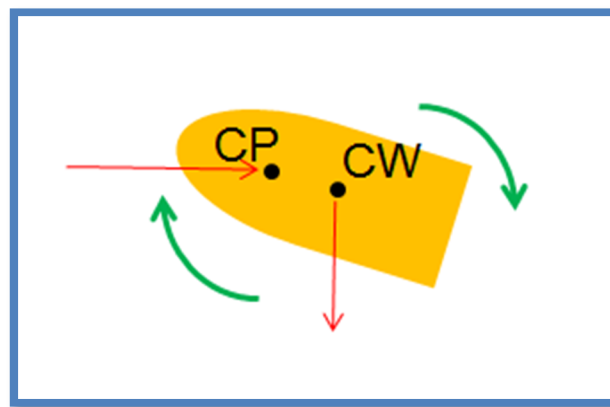
Fig.1-4. A simplified free body diagram of the projectile in exterior ballistics.
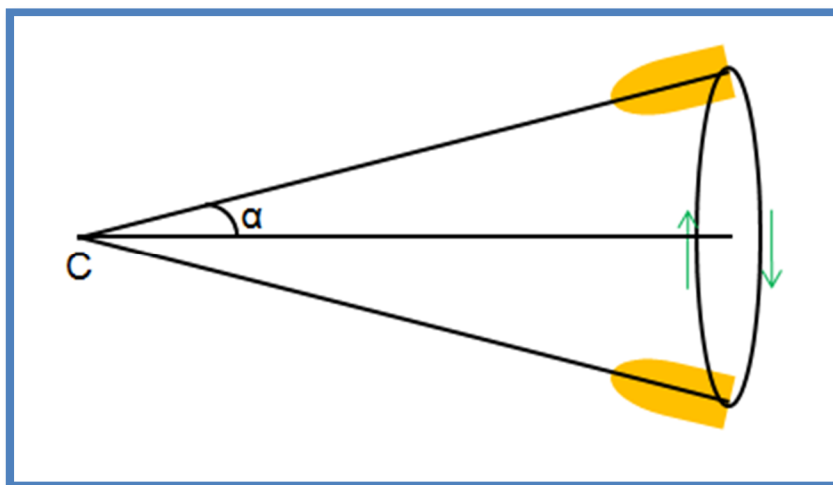
Fig.1-5. Precessional motion of a gyroscopically stabilized projectile.

1.1.3. Terminal ballistics

Terminal ballistics studies the behaviors of a projectile on a target. This study can be different from the projectile's detonating properties and the targets' properties. In general, small arms have no detonation system in the projectile. However, for the warheads of mortars and howitzers, there are fuses controlling the detonation method. For example, a fuse can be activated when the projectile contacts a target, inserted time is done, or a prolonged time after contacting a target. As targets, fixed material, e.g. concrete, metallic, and composite wall, and human body are considered [13-19]. This study extends to the bullet-proof or body-armor materials [20-21]. **Fig.1-6** depicts projectiles' penetrating types when the projectile is intruding perpendicular to the target surface's plane. These types are decided by the projectile and the target's material properties and the projectile's motion (velocity) [2].
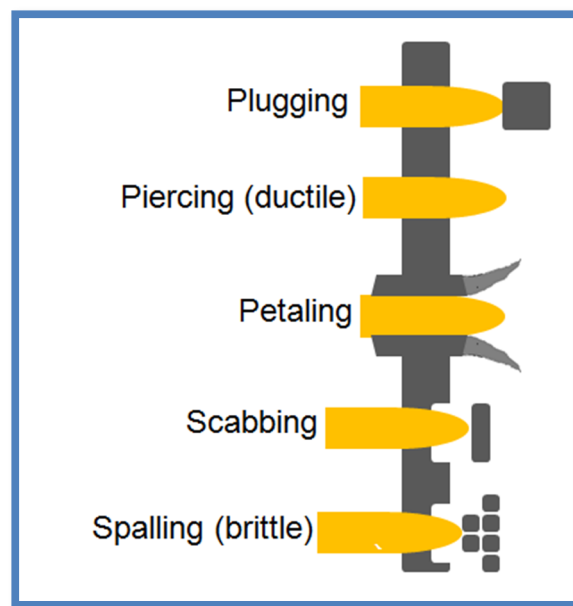
Fig.1-6. Projectiles penetrating types intruding perpendicular to the target's surface plane.

1.2. Gun Barrel

1.2.1. Importance of the gun barrel

For launching weapons such as small arms, tank cannon, and howitzers, the initial launching condition is decisive to construct the desired trajectory in exterior ballistics. In order to make up the ballistic initial condition, the function of a gun barrel is important. The gun barrel sustains the gas pressure, guides the projectile to the desired direction, and stabilizes projectiles using the rifling. Therefore, the gun barrel is significant in deciding maximum range, accuracy, and life span of the weapon system.

The requirements of launching weapon systems consist of longer maximum range, higher accuracy, and longer life span. To satisfy the requirement of longer maximum range, heavier projectile and higher gas pressure are the prerequisites. For instance, due to these prerequisites, the gun barrel's requirement in mechanical performance should be enhanced. To ensure projectile behavior consistency regardless of the weapon system's number of launches, the gun barrel should be well protected from its failure mechanisms.

The actual gun barrel was taken from the breechblock to front in **Fig.1-7**, which shows riflings engraved along the inner barrel wall.
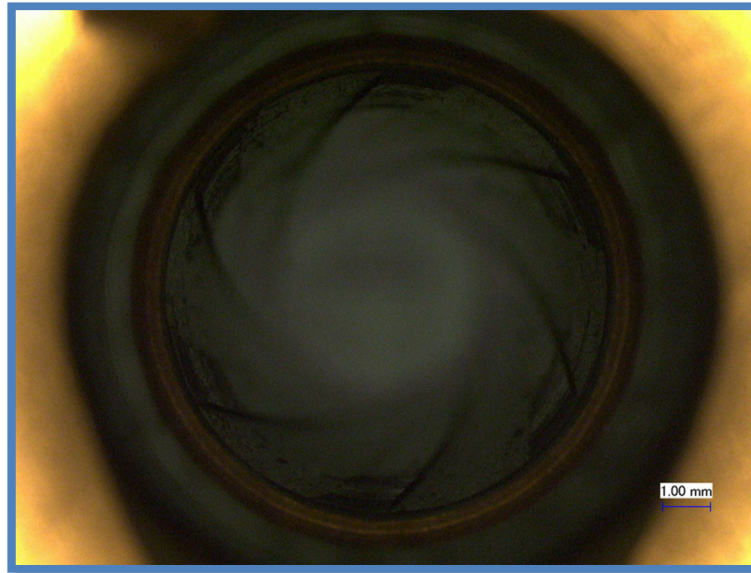
Fig.1-7. A micrograph of a gun barrel taken viewed from breech to front. The barrel is from Storm Lake Company for the model Glock 17 handguns. The micrographs were taken by a Keyence VHX-600K optical microscope with 20 magnification. Six lines of rifling lines are shown and they are proceeding anti-clockwise to the front.

1.2.2. Failure mechanisms of the gun barrel

The failure mechanism of the gun barrel is different from other weapon systems. For an example of interior ballistic condition, 120 mm main battle tank gun barrel increases the inner barrel surface more than 1300 °C, the maximum muzzle velocity of the projectile is 1637 m/s, and the maximum gas pressure inside of the gun tube is 490 MPa [22-23]. However, the commonly discovered mechanisms are wear, erosion, and fatigue [24-29]. Wear is caused by the friction between the gun barrel's inner surface and a projectile. For instance, in the case of 105 mm howitzer, extremely high temperature and chemical reaction between non-combusted gunpowder generates a white layer, which is weak in mechanical properties and results in wear by the frictional

forces. During the launching process, gas particles and extra particles, caused by incomplete combustion, are created. The high gas pressure forces the particles to move fast and collide with the wall of the gun barrel, and this is indicative of erosion. The high gas pressure, temperature, and the projectile inside the barrel force the gun barrel to extend along its radial direction. The repetition of extension and shrink cause fatigue and the fatigue is detected by the type of crack. In addition, high temperature generation in a short time generates instability stress distribution caused by the thermal extension irregularity and this assists these failure mechanisms [23, 30-33]. By observing the failure mechanism, tribological examination is one of the indices in selecting materials because wear and erosion are the primary failure mechanisms of gun barrels.

1.3. Tribology

Tribology is the study of friction, wear, and lubrication of materials. In material selection, tribological properties are one of the important criteria [34]. For example, in designing a brake disk, the material with high frictional force and low wear is selected. Bearing ball materials need low friction and low wear. For tribological properties, the empirical result is significant because the tribological properties predicted by several parameters, e.g., hardness, roughness, temperature, and lubrication condition, are incomplete [35]. Coefficient of friction and wear rate are used for the evaluation of the tribological behavior. Coefficient of friction is calculated by frictional force divided by applied normal force as shown in equation (1.1) [36]. Wear rate is computed using worn

volume, applied load, and scanned distance during the tribotest [37]. The function for calculating the wear rate is shown in equation (1.2).

$$\text{Friction Coefficient } (\mu) \ = \ \frac{\text{Frictional Force } (F_f)}{\text{Applied Normal Force } (F_n)} \qquad (1.1)$$

$$\text{Wear Rate} \ = \ \frac{\text{Worn Volume}}{\text{Applied Load} \times \text{Scanned Distance}} \qquad (1.2)$$

In addition to the equations above, different wear mechanisms decide the tribological behaviors of materials. There are several wear mechanisms: abrasive, adhesive, erosive, corrosive, and fatigue wear [38-41]. Abrasive wear occurs when two sliding materials have equal or unequal hardness, and it entails plastically impressed grooves and particles form of microchips. Adhesive wear induces severe wear. It is generated by bond or adhesion between contact surfaces. Tear or adhesion spots are detected on the surface of adhesion wear. Erosive wear is observed when particles collide with a surface of material in high velocity. Corrosive wear occurs when a layer caused by chemical reaction is combined with tribological contact. In fatigue wear, the contact between two surfaces generates local stress and the stress results in crack propagation. More than one wear mechanisms are often seen in a tribological process.

In designing a gun barrel, wear resistance is utterly necessary as proven from the tribological test result. In addition, the projectile needs a mixture of high and low wear resistant materials. Low wear resistance is required for the surfaces of the projectile that contact to lands of rifles because valleys should be formed by wearing the projectile's

surfaces. Meanwhile, non-contacted surfaces of the projectile are required to be geared with the lands of the rifles (high wear resistance). The geared projectile is illustrated in **Fig.1-8**.
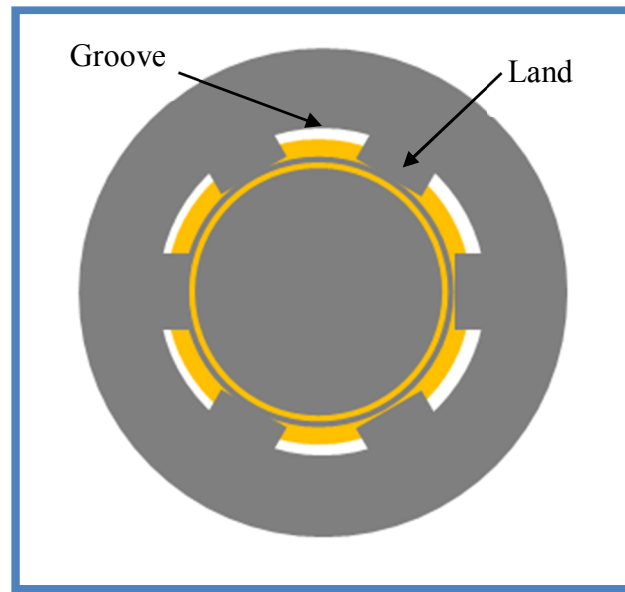
Fig.1-8. Description of a geared projectile by the barrel's rifling. The picture is viewed from the breech of the gun barrel.

1.4. Gun Barrel Reinforcing Strategies

1.4.1. Heat dissipation apparatus

Heat is generated during gun fire inside the gun barrel. Combustion of gunpowder and friction between the projectile and the barrel's wall are the major causes for heat generation. The generated heat is dissipated by ejection of gas to the muzzle, conduction through the barrel wall to the radial direction, and ejection of cartridge [32]. Meanwhile, the heat generation is operated for merely a millisecond unit of time.

However, the heat dissipation cannot follow the firing cycle. This trend is becoming problematic for machine guns, automated loading howitzers and tank guns.

In 19th and early 20th centuries, water was used as a cooling agent for machine guns such as M1917 Browning and Maxim machine guns [42]. Due to weight limitation, air was used as the cooling agent. This cooling method is not effective to cool gun barrel. Alternating gun barrels is usually used for today's machine gun practice. For example, using M60 general purpose machine gun needs to change its barrel every 10 minutes in the case of sustained fire [43]. This is inconvenient to carry an additional gun barrel in the combat operations.

Increasing the surface area is expected to increase the heat dispersion. Adopting cooling fins can be an answer to address this heat transfer problem. However, the size of gun barrel is too small to attach the cooling fins that are used in regular machines such as car engines. Nanoparticles have high surface-to-bulk ratio that is expected to be beneficial for thermal and energy application. Those particles have specific properties caused by extremely increased surface area. Gold nanoparticles have been used in catalyst, drug delivery, and chemical detectors [44]. If the outer surface of the gun barrel is coated with nanoparticles, heat dissipating ability can be enhanced. To date, general thermal examination of the nanoparticles has not been reported.

1.4.2. Surface coating methods

The surface coating has effective to change surface's properties [45]. To enhance the wear resistance of a gun barrel, coating methods have been used. Ceramic materials

such as a SiC coating were reported [46-47]. Crack generation was found due to their brittleness during fast operation cycled fires [48]. The other method is to coat the surface with other wear resistant metallic materials. One of the methods is a cylindrical magnetron sputtering (CMS) coating of tantalum [49-50].

To address the above issues, we propose to study model materials that are expected to have high wear resistance. We will focus on microarc oxidation coating as a ceramic material, and nano-twin structured film. Microarc oxidation is one of the promising plasma electrolysis methods because it is effective in cost and coating process [51]. Nano-twinned films have specific properties e.g., high thermal stability and strength [52-54]. For the purpose of applying these materials to the gun barrel reinforcement, tribological examination should be a prerequisite.

1.5. Summary

To understand launching weapon systems, ballistics was introduced. Ballistics was explained in terms of three different categories: interior, exterior, and terminal ballistics. Due to the high ballistic performances, the gun barrel must be well protected from its failure mechanisms. A gun barrel's failure mechanisms are wear, erosion, and fatigue. In addition, heat generation resulting in high temperature facilitates failure. The present research addresses these problems through advanced materials such as nanoparticles and coating materials.

CHAPTER II

MOTIVATION AND OBJECTIVES

As discussed in Chapter I, the surface properties are important for design and improvement of ballistic weapons. This research aims to examine three different advanced surface materials: nano particles, microarc oxidation coatings, and nano-twin structured films. The long term goal in this research is to study the failure mechanisms of gun barrel materials.

This research firstly develops model material systems in order to understand how gun barrel works. For thermal and heat transfer of the gun barrel, nanoparticles are selected to be the model system. There are asperities and particles generated during a gun shot. Thermal behaviors of nanoparticles could be followed from the understanding of the same. Specifically, the size dependence of nanoparticles will be examined. In addition, surface coatings will be studied.

There are two coatings systems to be investigated here, the microarc oxidation coating and nano-twin structured film. Understand obtained there is expected to benefit surface design and performance improvement of weapons.

There are three objectives in this research:

1. Obtain understanding of heat dissipation mechanisms in the gun barrels. The research utilizes a simplified model of nanoparticles to analyze the thermal behavior dependent on the nanoparticles' sizes.

2. Obtain understanding in friction and wear behavior of gun barrels and projectile surfaces by applying microarc oxidation coating on the inside of a barrel in order to understand its behaviors.

3. Obtain understanding of rifling functions and mechanisms by applying nano-twinned copper film to the cap of a projectile.

These objectives are important for enhancing the gun barrel's performance as the first step for searching enhanced material application.

This research is expected to enhance the performance of guns by suggesting new and advanced materials, which will improve the surface properties of the same.

CHAPTER III

EXPERIMENTAL PROCEDURE

This chapter describes materials used for the present research. The gold nanoparticles (AuNPs), microarc oxidation coating of magnesium, and nano-twinned copper film were prepared fabricated and samples were prepared. Thermal analysis was conducted on AuNPs by differential scanning calorimetry and thermogravimetric analysis (DSC-TGA). For coating materials, pin-on-disk tribotests were carried out. Furthermore, the miroarc oxidation coatings were examined using potentiodynamic polarization.

3.1. Gold Nanoparticles

3.1.1. Synthesis of AuNPs

The well known Turkevich method [55] was applied to the synthesis of gold nanoparticles (AuNPs). The synthesized Au particles were stabilized and separated from each other by the negatively charged tri-sodium citrate molecules. The detailed preparation process is as follows.

For particle synthesis, these chemicals were used: deionized (DI) water, tri-sodium citrate dihydrate ($Na_3C_6H_5O_7 \cdot 2H_2O$, purchased from Sigma-Aldrich), and hydrogen tetrachloroaurate tri-hydrate ($HAuCl_4 \cdot 3H_2O$, 99.9 %wt, Sigma-Aldrich) were used for the entire synthesis process. Hydrogen tetrachloroaurate tri-hydrate was used as

the source of Au precursor for the synthesis process. Tri-sodium citrate dihydrate solution acted as a reducing agent which can also control the growth of the particles. Here tri-sodium citrate acted as a reducing agent together with stabilizing agent for the formation of Au particles. The procedure of making the particle is as follows:

1. The amount of 1.25 ml of 10^{-2} (M) aqueous gold chloride ($HAuCl_4 \cdot 2H_2O$) solution was taken to 100 ml sized flask and 48.35 ml of deionized water was added (by concentration of the aqueous gold chloride and the volume, the mass of the gold was calculated as 0.246208211 g).

2. The above solution was vigorously stirred and heated at 80 °C.

3. The amount of 1 wt% tri-sodium citrate was added with different volume (depending on the desired size of particle solution) in the continuous process of stirring and heating.

4. In the process, the color of the solution changed in the following order; light blue, faint yellow, clear grey, purple, deep purple, and wine-red.

5. As the color of the solution was observed as wine-red, the stirring and heating was continued for an additional 10-15 min.

6. De-ionized water was added to make the total volume of the solution 50 ml.

Each sample was differently processed by adding different volume of tri-sodium citrate; 1.3 ml, 0.75 ml, 0.50 ml, and 0.30 ml for the samples from 1 to 4, respectively.

Fig.3-1 is the image of sample 3, citrate stabilized AuNPs Solution.
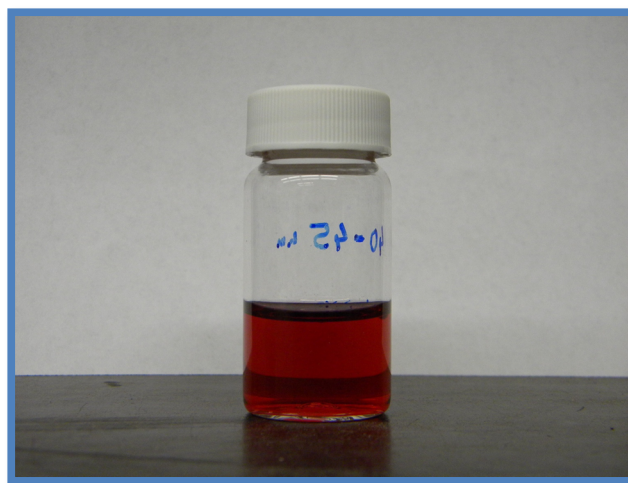
Fig.3-1. Synthesized gold nanoparticles solution.

3.1.2. Characterization of AuNPs

After the synthesis, the particle sizes were measured through the micrographs of the transmission electron microscopy (TEM). The TEM (JEOL 2010) was used at 200 keV. In order to evaluate the accuracy of size measurement, particle sizes were measured under different magnifications. The particle images from the micrographs were analyzed with the 'image J' imaging program. The sizes of the particles were statistically analyzed in terms of major and minor-axis lengths.

The particle size was measured from the length unit matching procedure, whose objective was to convert the length unit from pixel to nm. The conversion was calculated by measuring the scale bar of each micrograph in pixel (**Fig.3-2**) and using the function 'Set Scale' (**Fig.3-3**). The program measured the dimensional length in nm after this setting.
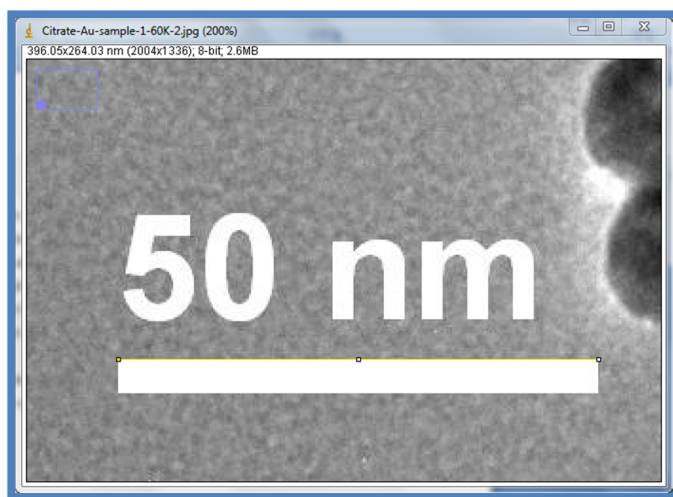
Fig.3-2. Measuring the scale bar by the pixel unit.
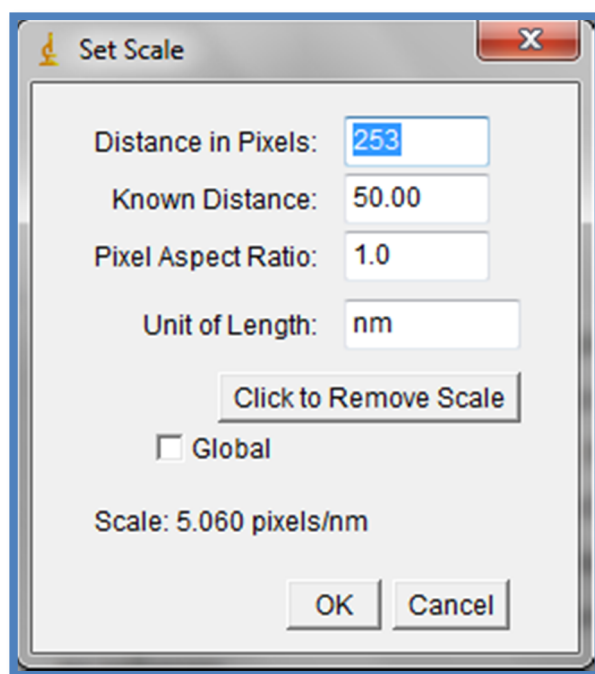
Fig.3-3. Setting the length unit from pixel to nm.

After setting the length unit, the size of each particle was measured. Though the particles were regarded as spheres, the images showed that they were elliptical. For that reason, the diameter of a particle was measured from the major and minor-axes (**Fig.3-4**). The two sizes measured were averaged by geometric mean value to preserve the surface area of the particle as if the particles were spheres. The particles were numbered on the hard-copied micrographs so as not to measure the same particle repetitively. The measured data were arranged in accordance with the sample and the magnification of the images.
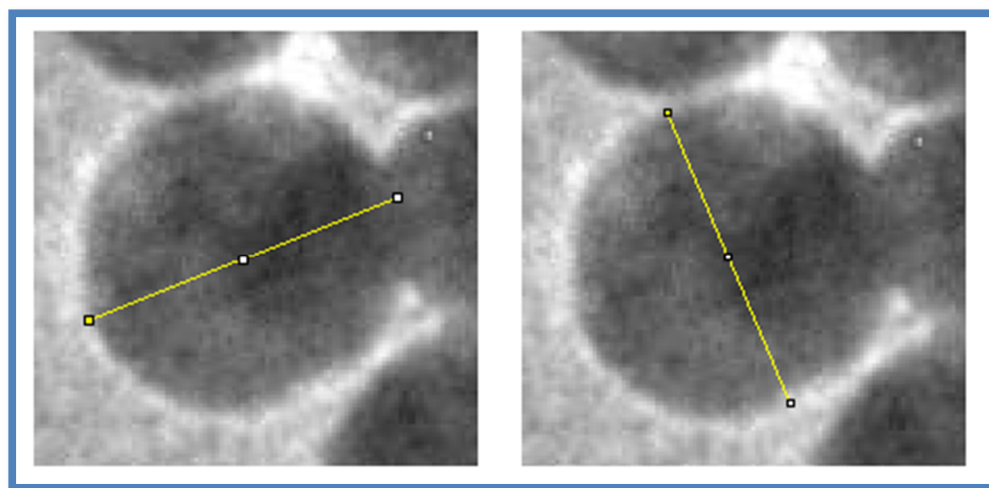
Fig.3-4. Measuring of major (left) and minor (right) axes in length.

3.1.3. DSC-TGA

Differential scanning calorimetry and thermogravimetric analysis (DSC-TGA) was performed on the AuNPs samples. This method examines the thermal properties using differencing measurement between reference and sample holding apparatus [56].

The instrument model SDT Q600 (TA Instrument) was used to complete the analysis (**Fig.3-5**). It contains sample holders and measuring sensors inside the furnace. Two pans (sample holders) are connected to particular cantilevers (**Fig.3-6**), and the system measures the weight and temperature of the pans. One of the pans functioned as a sample holder and the other as a reference. The pans were made of alumina, which has a higher melting point (2072 °C) than that of the gold bulk (1064 °C). The furnace was filled with nitrogen gas at a fixed concentration during the tests. The test temperature started at room temperature and was raised to 1500 °C at an incremental increase of 0.331 °C/sec (**Fig.3-7**). Due to the successive change of heat flow, the temperature incremental rate was not constant and it is shown as error bar in the figure. The weight resolution was 0.0001 mg and that of heat flow was 0.001 mW.

The test was repeated four times for a sample. The results will be stated in terms of critical points on test curves and their energy calculations. The initial weight of test sample was set to be the same. The average initial weight of each test set is shown in **Fig.3-8**.

Fig.3-5. TA Instrument SDT-Q600 DSC-TGA.
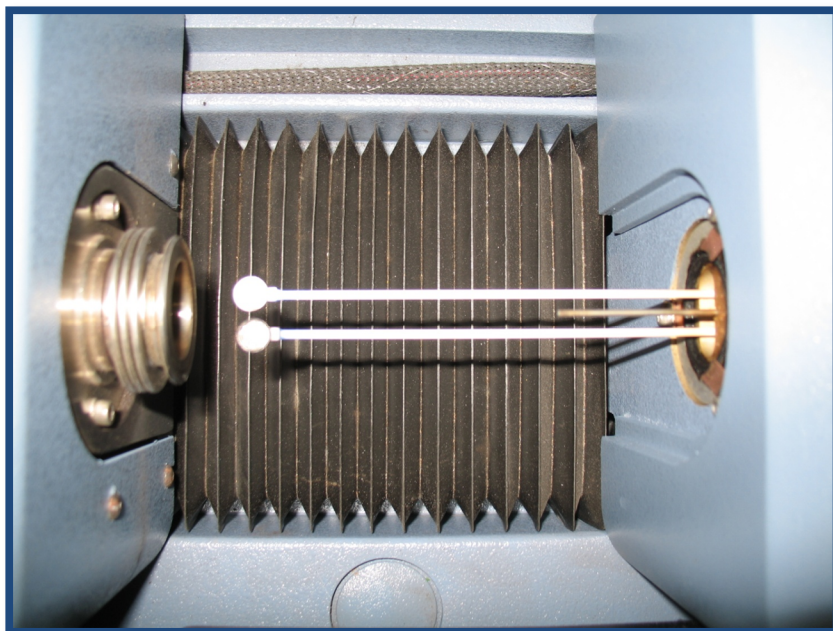
Fig.3-6. Sample holders and connected cantilever.
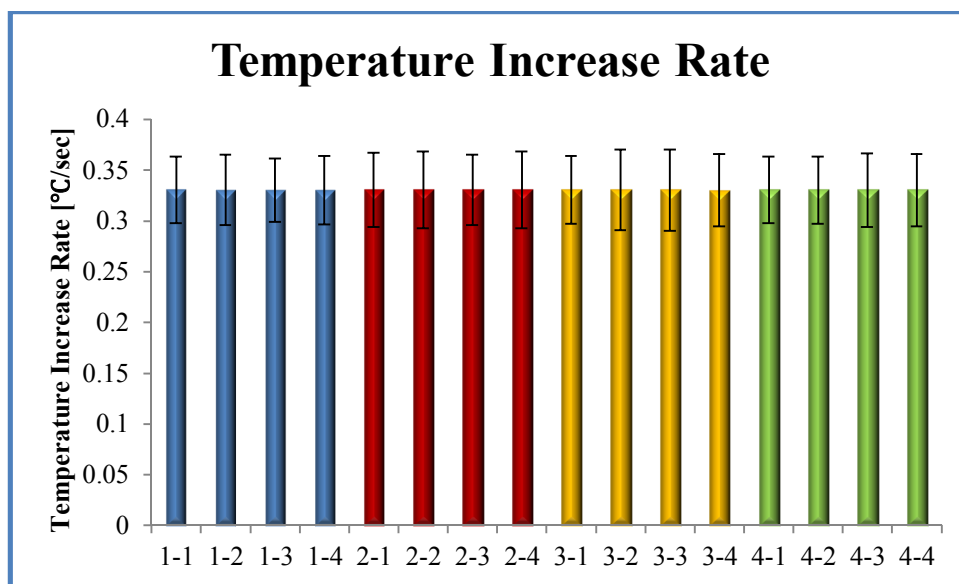
Fig.3-7. Average temperature increase rate for each test set.
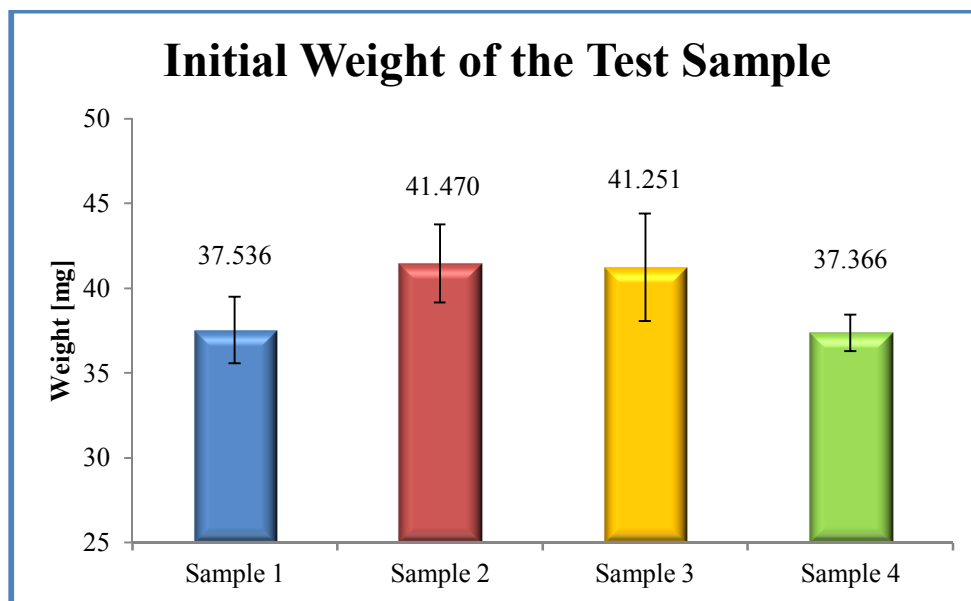
Fig.3-8. Initial weight of the test sample.

3.2. Microarc Oxidation Coating of Magnesium

3.2.1. Coating processes

The samples were prepared by our collaborator (Gebze Institute of Technology and Bogazici University Bebek, Turkey) with microarc oxidation method. A schematic description of the coating method is shown in **Fig.3-9**. A metallic substrate was steeped in an aqueous electrolyte. A power supply was connected to the anode (substrate) and cathode (stainless steel vessel). The high voltage power supply generated an electric arc that instantly melted the surface of the substrate. The melted substrate materials reacted with electrolyte materials and resulted in the coating on the substrate.
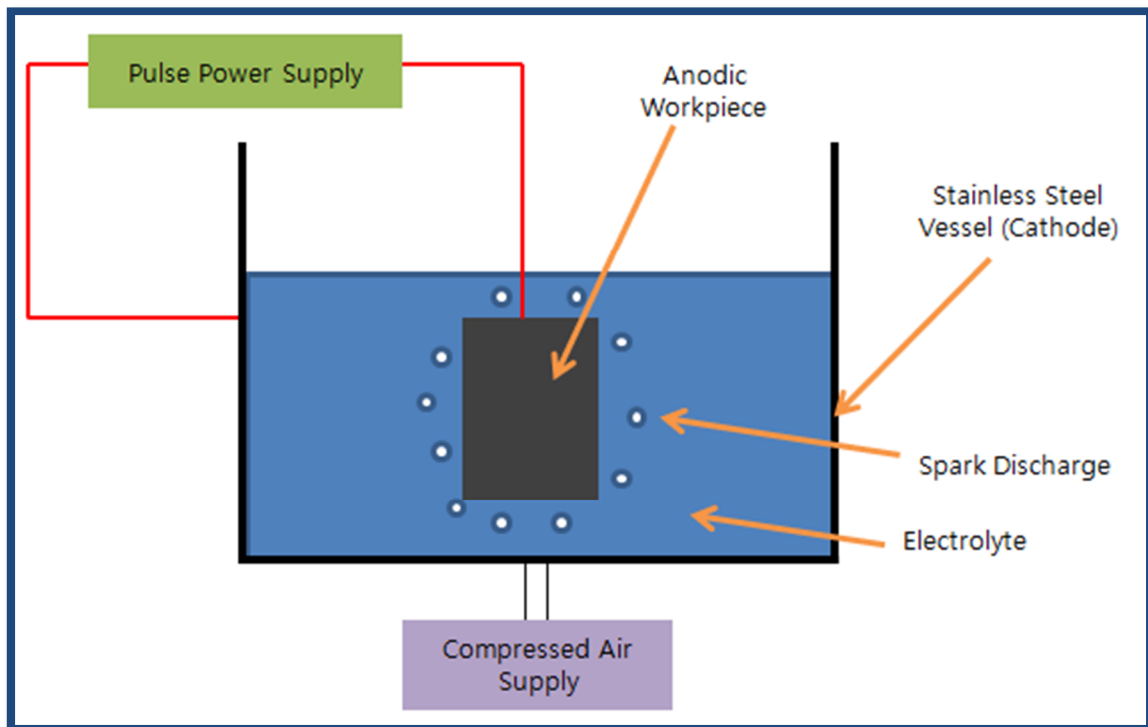
Fig.3-9. Schematic description of microarc oxidation coating.

For the sample preparation, 100 kW MAO machine with an AC power supply was used. The current densities applied were 0.06 or 0.14 A/cm^2 for different samples. The aqueous electrolyte contained KOH and $Na_2SiO_3 \cdot 5H_2O$ for making a particular type of samples, named 1C; while KOH and Na_3PO_4 were used to create an alternate type of samples, 2C. The coating procedure was conducted for 50 minutes for each sample.

The surfaces of the coatings were imaged using a Keyence VHX-600K optical microscope. **Fig.3-10** shows the surfaces' development of porous structures. This is thought that the high potential generated air bubbles and the coating materials solidified into pores [51, 57].

Roughness, hardness, coating thickness, and composition of coating material were measured for each prepared sample. The roughness test was measured with TR-1900 profilometer of Qualitest^{TM}. The roughness test was conducted with 0.4 mm × 5L scanning length and repeated 3 times (results shown in **Fig.3-11**). The Vicker's hardness tests were preceded by using a microhardness tester (Anton Paar MHT-10). The coating thickness was measured with Fischer Dualscope MP20 and the result is shown in **Fig.3-12**. The composition of materials was examined by XRD spectra with X-ray diffractometer, Bruker D8 Advance, and the spectra are shown in **Fig.3-13**. **Table 3-1** shows the coating conditions and the measured parameters mentioned above. From **Fig.3-11**, the coatings increased the surface's roughness. Comparing the coated samples, the samples with higher applied current density have higher roughness. In addition, the coatings of 1C are twice harder than those of 2C. In terms of coating thickness, high

coating current increased thickness. The samples of 2C composition have higher thickness compared to the other coated samples.

1C-0.06	1C-0.14
2C-0.06	2C-0.14
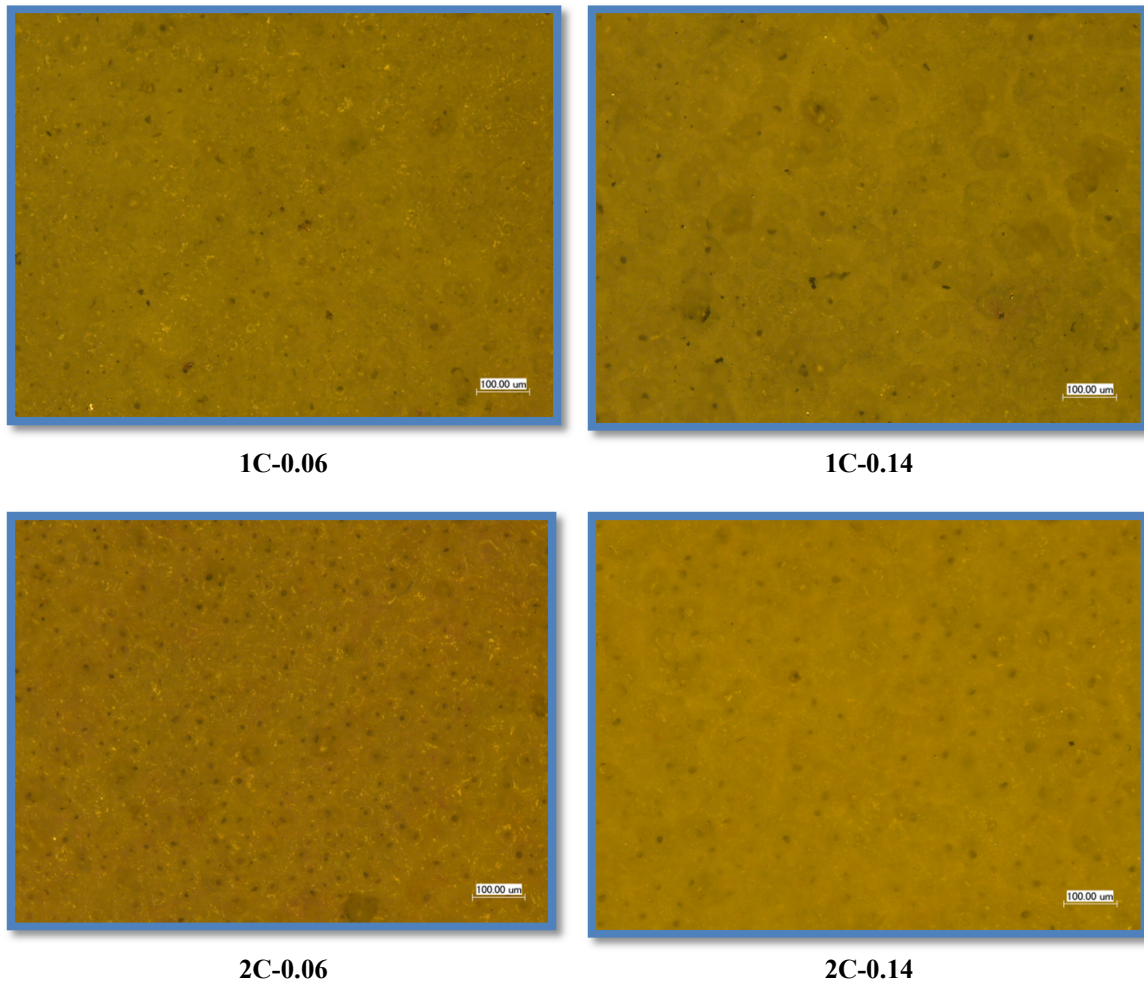
Fig.3-10. The optical micrographs of each sample coating surface with the magnification of 300.
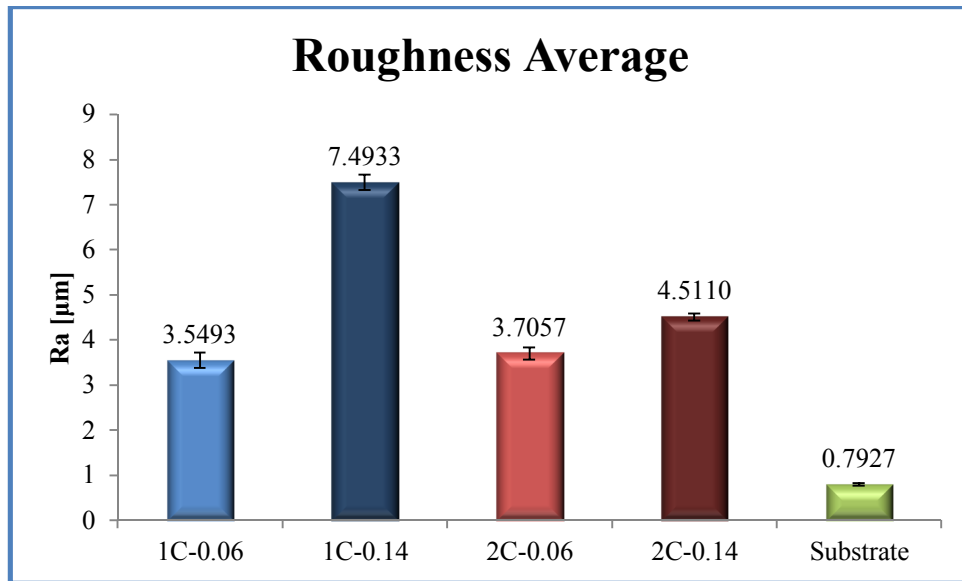
Fig.3-11. Roughness of coatings and the substrate surface.
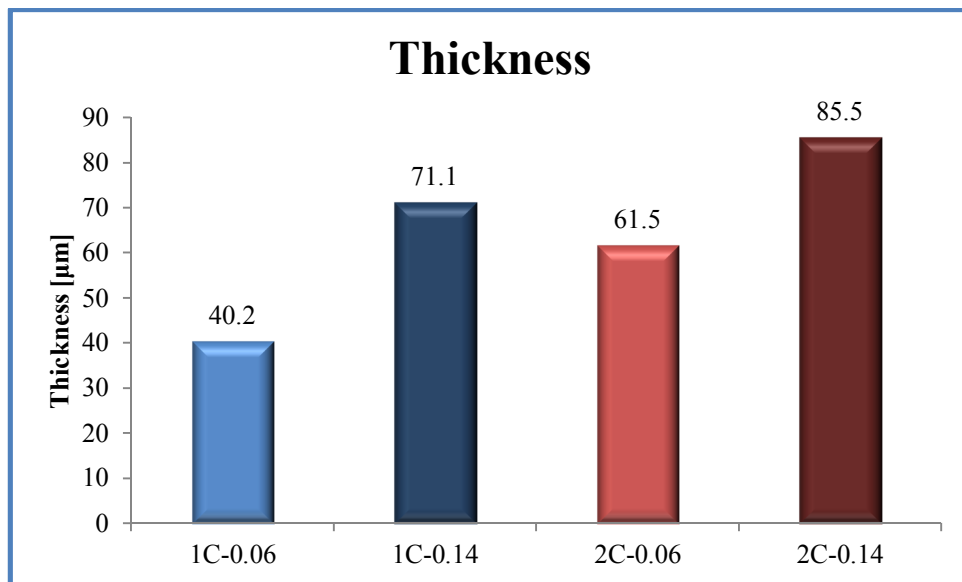
Fig.3-12. The thickness of coating.
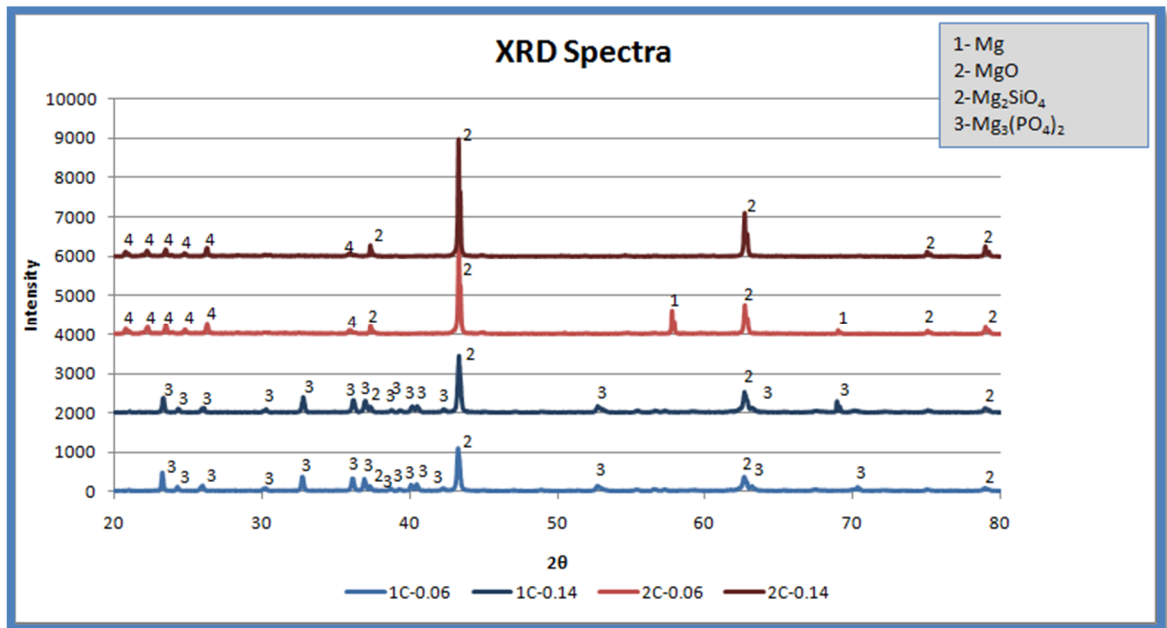
Fig.3-13. XRD spectra of each sample.

Table 3-1. The coating conditions and the coating properties of each sample.

Sample Number	1C-0.06	1C-0.14	2C-0.06	2C-0.14
Coating Solution	Na_2SiO_3 + KOH		Na_3PO_4 + KOH	
Coating Time [min]	50			
Current Density [A/cm^2]	0.06	0.14	0.06	0.14
Coating Thickness [μm]	40.2	71.1	61.5	85.5
Roughness Ra [μm]	3.5493	7.4933	3.7057	4.511
Hardness [HV]	534.6 kgf/mm^2		280.8 kgf/mm^2	
Composition	MgO, Mg_2SiO_4		MgO, $Mg_3(PO_4)_2$	

3.2.2. Tribotesting

A pin-on-disk tribotester (CSM Instruments) was used to examine mentioned materials. A reciprocating linear test mode was selected with amplitude of 6 mm. The maximum scanning speed (at the center of the stroke) was 2.5 cm/s and testing time was 4 hours in the case of the coated samples. However, because of the higher wear of the plain substrate, the uncoated substrate test was reduced to 1 hour due to the translational force limitation of the instrument. The selected test load was 5 N delivered using a D52100 bearing ball of 6 mm diameter. The test entailed no lubricant (dry condition), and the contacting surfaces were cleaned with acetone before the test. A schematic describing the test is shown in **Fig.3-14** and the testing conditions are presented in **Table 3-2**.

After the tribotests, the wear tracks of coatings and ball wears were observed by using an optical microscopy. A Keyence VHX-600K optical microscope was used for the optical microscopy. In order to calculate the worn volume of each sample's wear track, a TR-1900 profilometer was used to measure the profile of the worn surface. In order to measure the section perpendicular to the wear track's scanning direction, the profilometer measured along the direction shown in **Fig.3-15**. In addition, the figure shows the scanned locations to calculate the worn sections' area statistically.
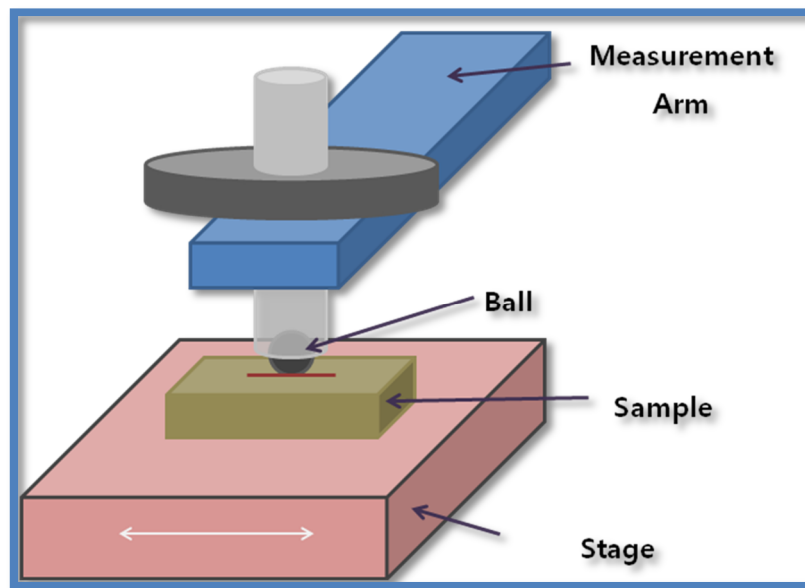
Fig.3-14. Schematic description of the tribotest.

Table 3-2. The tribotest conditions of microarc oxidation coating samples.

Mode	Maximum Scanning Speed [cm/s]	Amplitude [mm]	Load [N]	Time [hour]	Distance [m]	Scanning Partner
Ball-on-disk, linear	2.5	6	5	4 or less	229.2 or less	D52100 Bearing Ball Dia. 6 mm
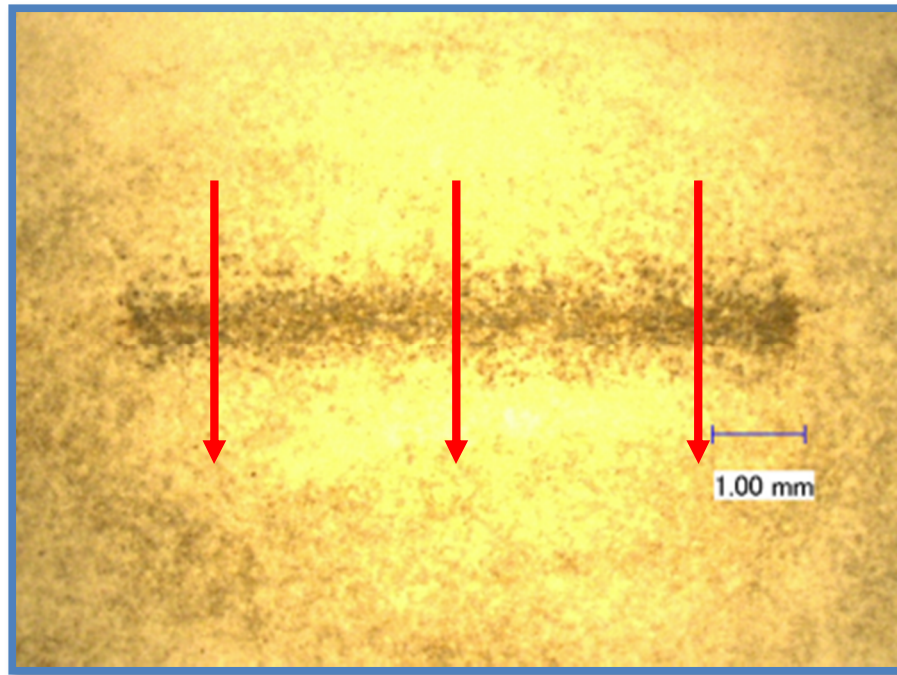
Fig.3-15. Scanning locations and directions for calculating the wear track section area.

3.2.3. Corrosion tests

To evaluate the anti-corrosion performance of the coated samples, a corrosion test was performed. Potentiodynamic polarization tests were conducted as shown in **Fig.3-16**. Gamry Instruments Reference600 was used as the potentiostat, while a saturated calomel electrode and a platinum wire were used as the counter and the reference electrodes, respectively. To control the contact area with the electrolyte, the sample block was sealed by applying nail polish to all surfaces except the testing area. The electrolyte was 3.5 %wt NaCl (EMD Chemicals Inc.) aqueous solution imitating sea water. After steeping for 30 minutes, potentiostat measured the current while varying the potential from -2 V to -1 V with a rate of 1 mV/s.
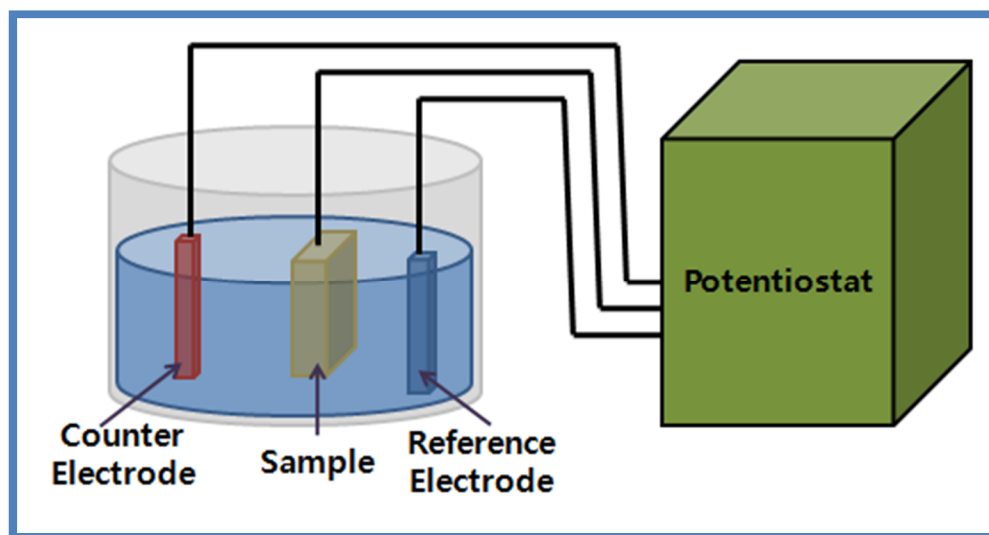
Fig.3-16. Schematic description of the corrosion test.

3.3. Nano-twinned Copper Film

3.3.1. Nano-twinned copper film coating

The samples were prepared with the physical vapor deposition (magnetron sputtering) method. Two different silicon wafers, i.e., (100) and (110) planed wafers, were used as substrates and 99.9999 %at of copper was used as the coating material. **Fig.3-17** shows the schematic description of the coating process. Before the coating, the surface of the substrate was etched with 10 %mol of HF. The coating was fabricated at room temperature, 40 sccm of argon gas in-let, vacuum pressure of $5 \times 10^{-8} \sim 1 \times 10^{-7}$ torr, and 10 Å/s of deposition rate.
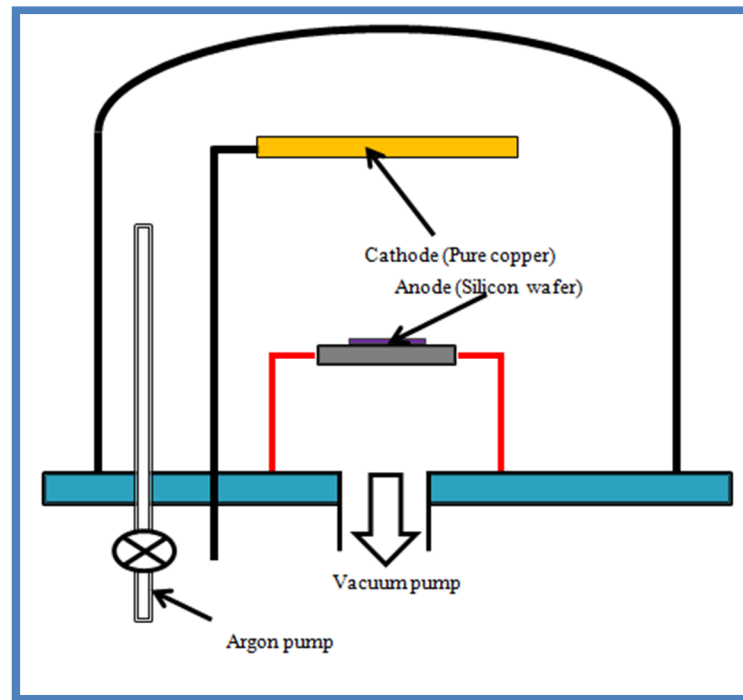
Fig.3-17. Schematic description of the coating method (physical vapor deposition).

The film created on the silicon plane (100) was grown to the direction of <100> and the silicon plane (110) made the copper film grown to the <111> direction, epitaxially. The samples were named Cu100 and Cu111 in accordance with the growing direction. The nano-twinned structure was discovered in the Cu111 samples. Before conducting the tribological experiments, hardness and film thickness were measured. The hardness was measured with Fischerscope MP2000 nanoindentor. The thickness was measured with a Veeco Dektak 150 surface profiler. The coating condition and the properties of the films are stated in **Table 3-3**.

Table 3-3. Coating conditions and properties of the samples, Cu100 and Cu111.

	Cu100	Cu111
Coating Method	Magnetron sputtering	
Coating temperature	Room temperature	
Vacuum pressure	$5\times10^{-8} \sim 1\times10^{-7}$ torr	
Argon gas inlet	40 sccm	
Deposition rate	10 Å/s	
Substrate	Silicon plate (100)	Silicon plate (110)
Film thickness	1.2 μm	
Film hardness (HIT)	1.5 GPa	2.8 GPa
Nano-twinned structure	Non-exist	Exist

3.3.2. Tribotests of the copper films

The tribotest was conducted to identify tribological performances of the nano-twinned material. From the two differently structured materials, coefficient of friction and wear resistance were examined. **Figs. 3-18** and **19** show the atomic structures of (111) and (100) planes based a face centered cubic structure. The sliding direction of the tribotests was expected to be different due to their atomic structures. Tribotests were conducted to verify the nano-twinned structure and effects of sliding on friction and wear.
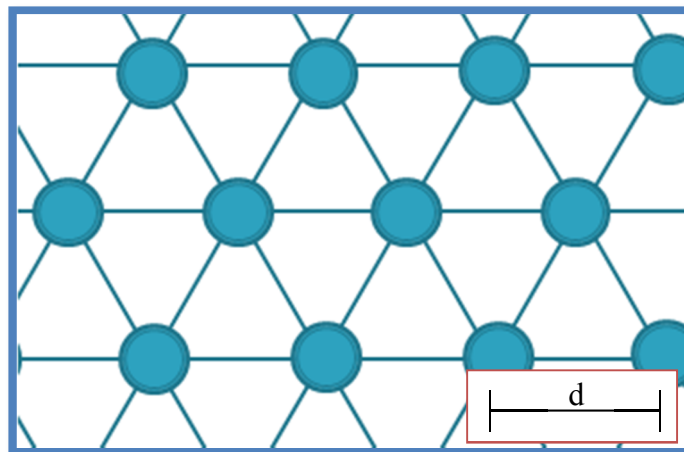
Fig.3-18. Atomic structure of (111) plane. d is the diameter of the atoms.
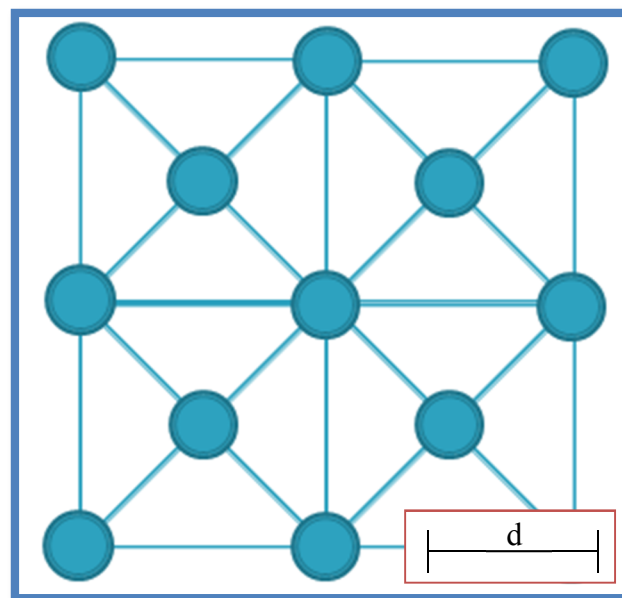
Fig.3-19. Atomic structure of (100) plane. d is the diameter of the atoms.

The tribotests were conducted on each sample. The schematic is the same as **Fig.3-15**. The test conditions such as sliding stroke speed, load, time, sliding distance,

and scanning direction were controlled and changed. The test conditions are summarized

in **Table 3-4**.

Table 3-4. Tribotest conditions of copper films.

Mode	Maximum Scanning Speed [cm/s]	Amplitude [mm]	Load [N]	Time [min]	Scanning Direction	Distance [m]	Scanning Partner
Ball-on-disk, linear	2.5	4	1	30 or less	Horizontal and Vertical	28.8 or less	D52100 Bearing Ball Dia. 6 mm

After the tribotests, coefficient of friction was analyzed by using the data

gathered from the controlling computer. The worn surfaces of samples were measured

by using a Keyence VHX-600K optical microscope, a Tescan USA VEGA-II VPSEM

scanning electron microscope, and a Veeco Dektak 150 surface profiler. The two

microscopes acquired micrographs of the wear tracks. The profiler was used for plotting

the wear track section profiles like the method described in **Fig.3-15**.

3.4. Summary

The three advanced materials, i.e., AuNPs, microarc oxidation coating of

magnesium, and nano-twinned copper film were introduced in terms of creating these

material. The specific experiment methods were delineated for each material. The

experimental results will be described and the results will be discussed in the following

three chapters.

CHAPTER IV

SIZE EFFECTS OF GOLD NANOPARTICLES ON THERMAL PROPERTIES

This chapter discusses the size effects of gold nanopaticles (AuNPs) on their thermal properties. The thermal properties, such as temperature, heat flow, and energy of phase changes, are discussed based on results obtained from the differential scanning calorimetry and thermogravimetric analysis (DSC-TGA).

The size distribution was firstly obtained through statistical analysis of high resolution images. During DSC-TGA analysis, the temperature, heat flow, and area of designated period were calculated. Results showed that thermal properties were affected by the size and the surface-to-bulk ratio.

4.1. Size Parameters

The measured particles were categorized by their size in diameter to chart the distribution. The distribution was obtained by dividing the particles as size using the successive 'IF' function of 'Microsoft Excel' and plotting the divided data of their size categories. Results are shown in **Figs. 4-1** to **4-4**. The average size of each sample was compared in **Fig.4-5**. The average size of the particles and the number of measured particle are shown in **Table 4-1**. As indicated in **Fig.4-5**, the particle size is consistent at different magnifications for samples 1, 2, and 3. However, sample 4 showed different dimension at the different magnification. This is due to the fact that the sampling number

of this particular specimen was smaller compared to the other samples. Thus, the size distribution of sample 4 is inconclusive. The further analyses were carried out using the lowest magnification because of the sufficient number of particles.
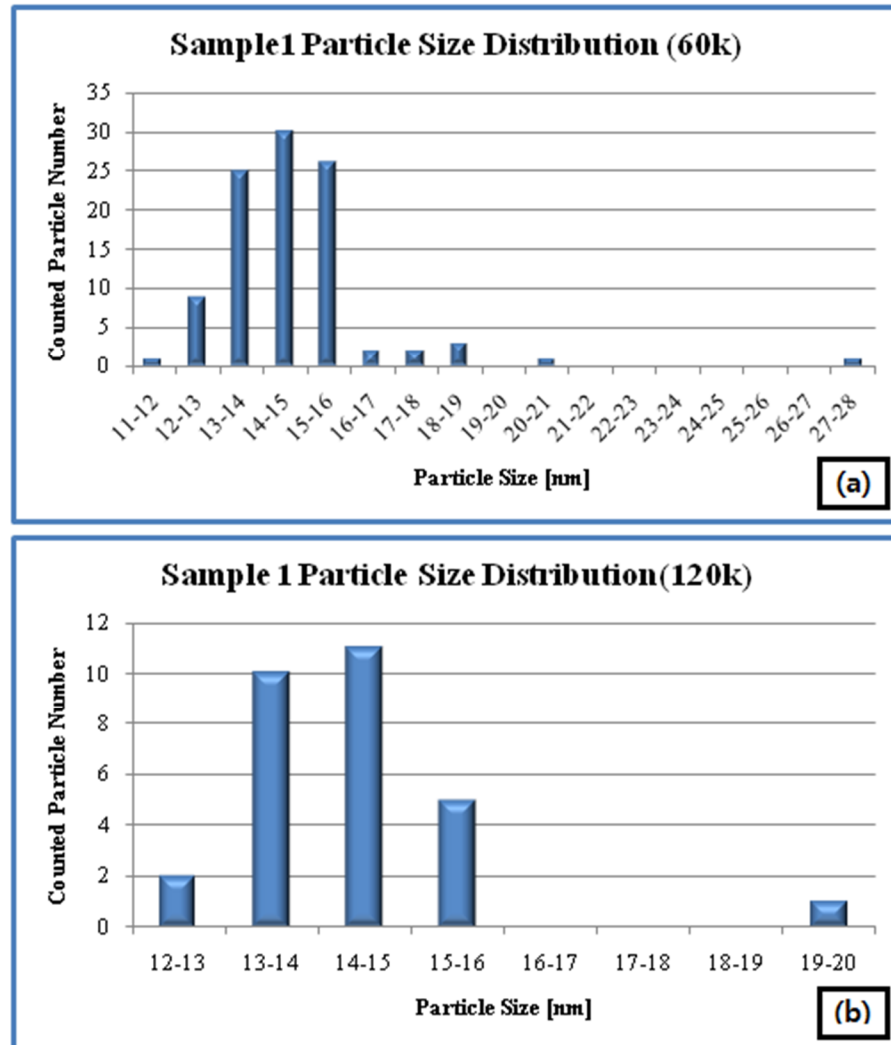
Fig.4-1. Size distribution of sample 1, measured by magnifications of 60,000 (a) and 120,000 (b).
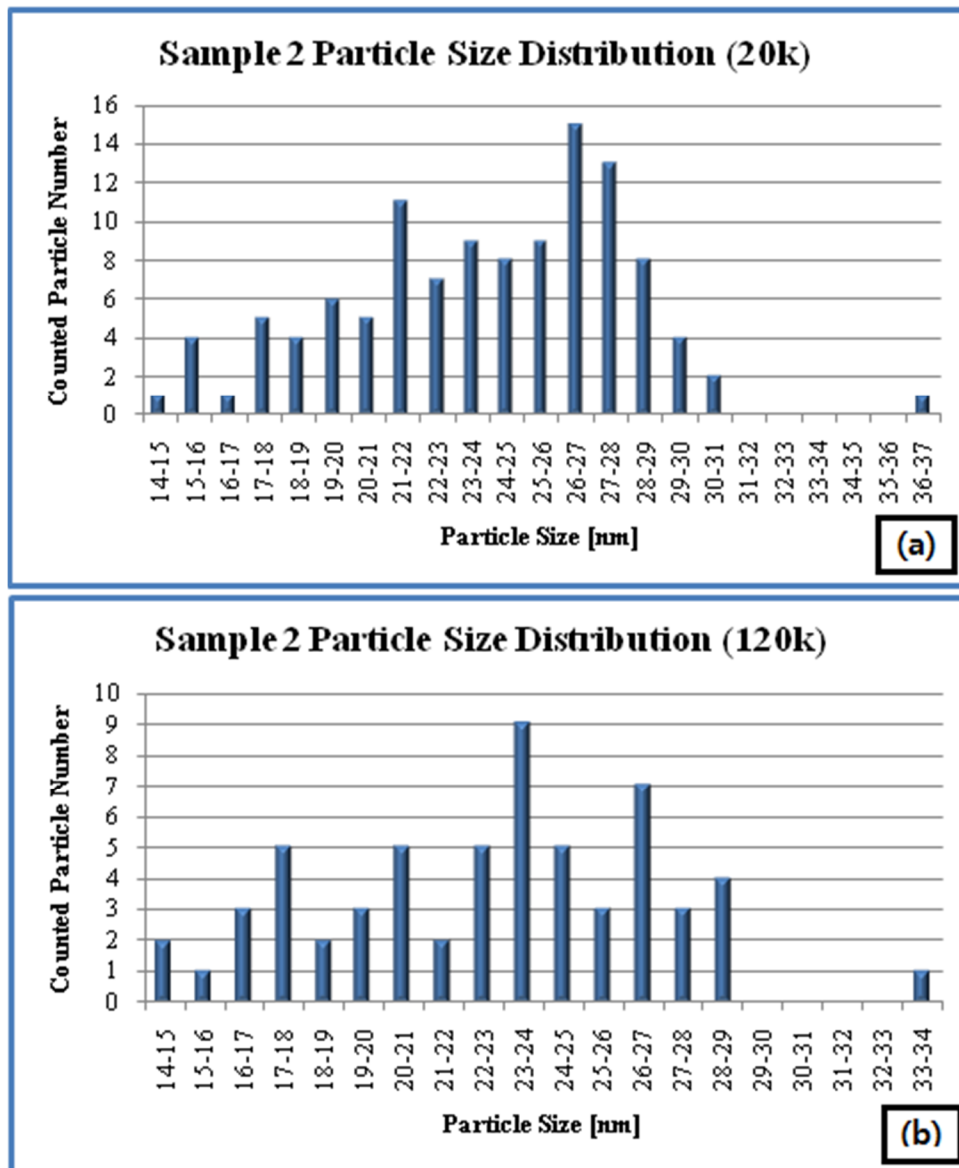
Fig.4-2. Size distribution of sample 2, measured by magnifications of 20,000 (a) and 120,000 (b).
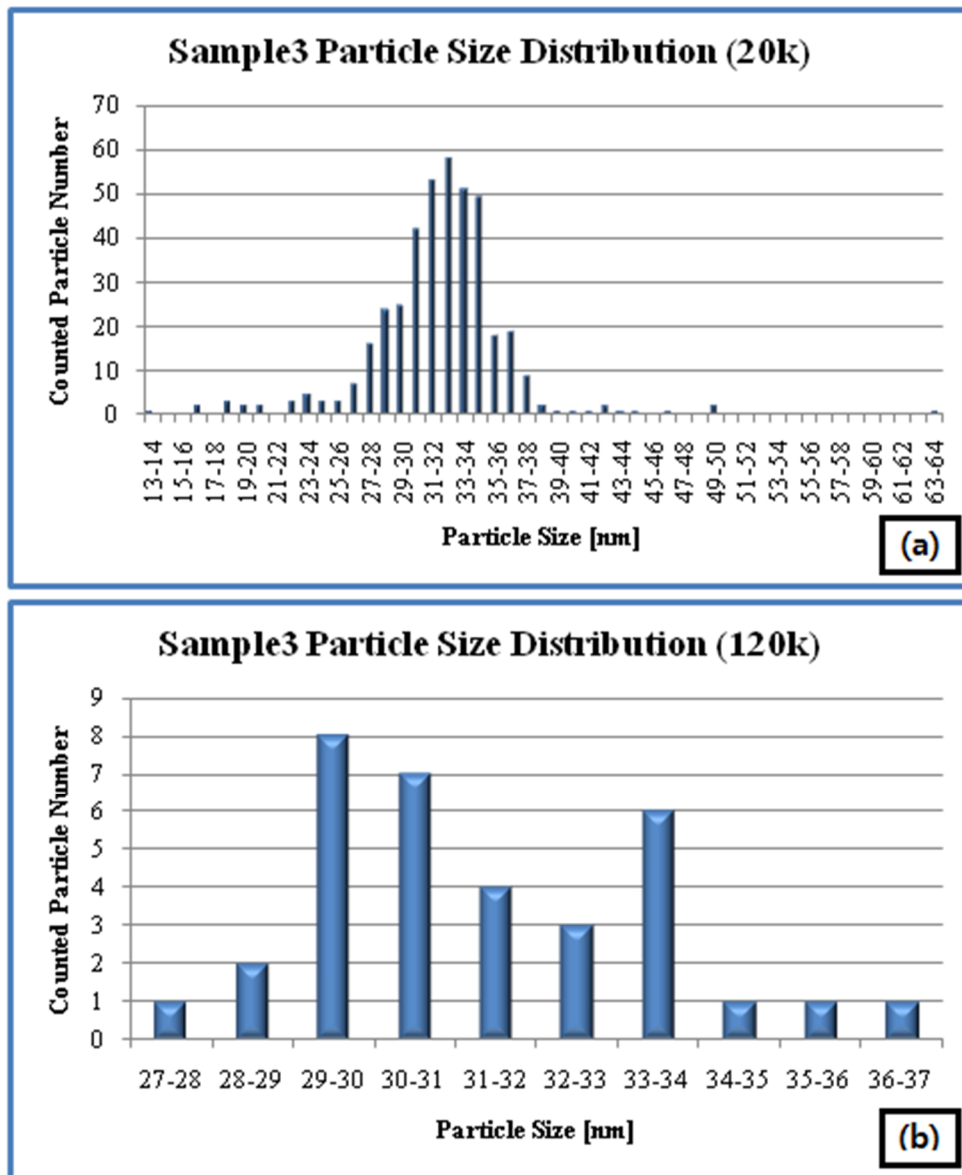
Fig.4-3. Size distribution of sample 3, measured by magnifications of 20,000 (a) and 120,000 (b).
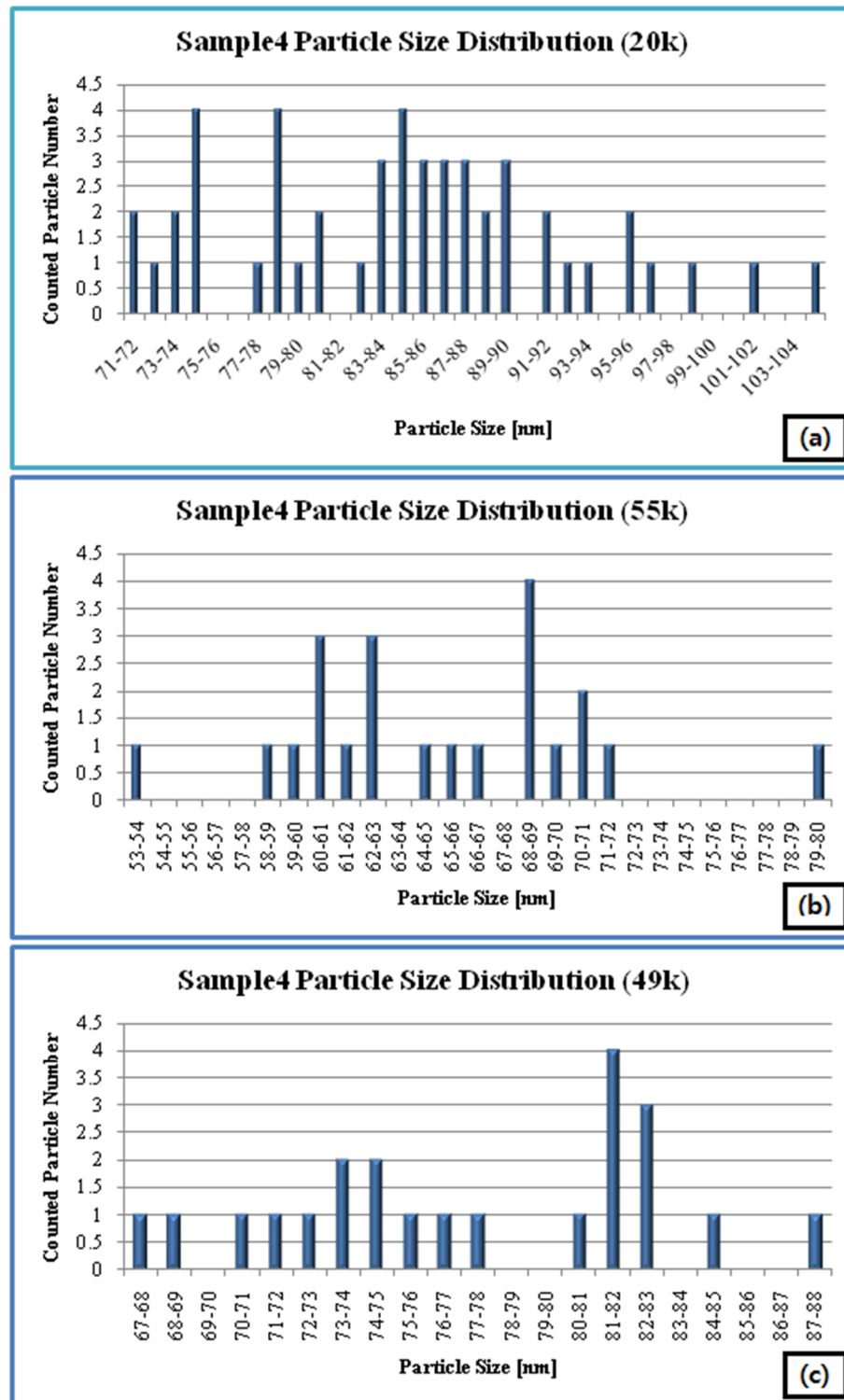
Fig.4-4. Size distribution of sample 4, measured by magnifications of 20,000 (a), 55,000 (b), and 49,000 (c).

Average Size of the Particle Measurements
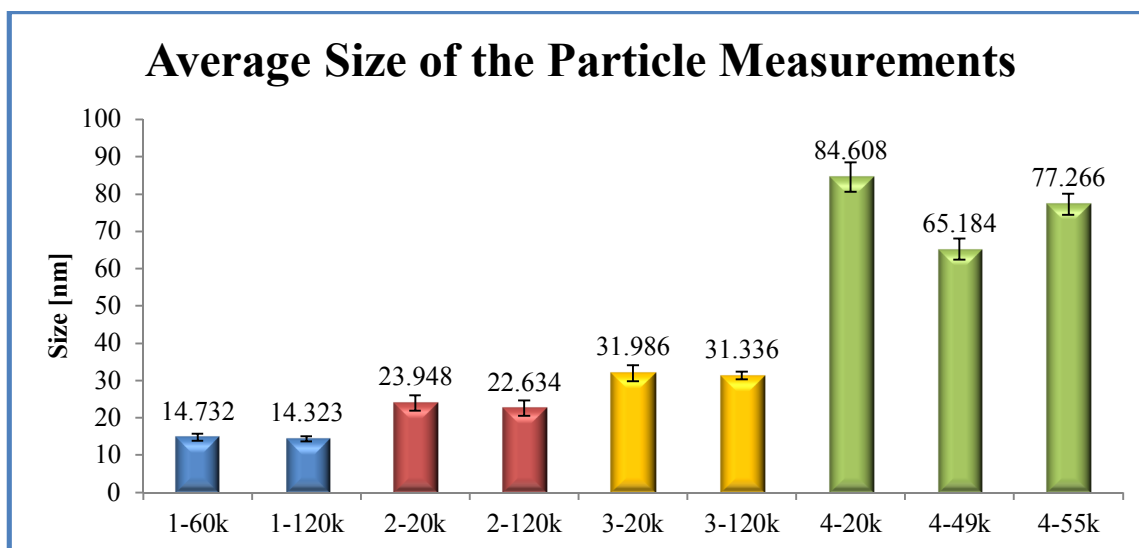
Fig.4-5. Average particle size (in diameter) of samples and measured microscopy magnifications. The labels on x-axis are the sample number and the magnification of the micrograph, each.

Table 4-1. Average particle size of each sample classified by microscope magnification and measured method, and measured number of particles.

Sample Number	Magnification	Major-axis [nm]		Minor-axis [nm]		Mean Size [nm]		Number of Particles Measured
		Average	StDev	Average	StDev	Average	StDev	
1	60k	15.811	2.597	13.774	1.571	14.732	1.843	100
	120k	15.240	1.784	13.483	1.081	14.323	1.285	29
2	20k	27.157	6.003	21.235	3.090	23.948	4.056	113
	120k	25.322	5.279	20.301	3.486	22.634	4.121	60
3	20k	36.620	5.920	28.050	3.894	31.986	4.361	408
	120k	35.443	3.566	27.796	2.200	31.336	2.173	34
4	20k	89.490	10.420	80.130	7.113	84.608	7.939	49
	49k	69.456	8.089	61.329	5.470	65.184	5.698	22
	55k	87.951	10.279	68.168	5.284	77.266	5.660	22

The volume of each particle was calculated using the average particle size in **Fig.4-6**. The surface area and the surface-to-bulk ratio are shown in **Figs. 4-7** and **4-8**. The surface-to-bulk ratio is used as the independent size parameter to be compared with the variables acquired from thermal analysis.
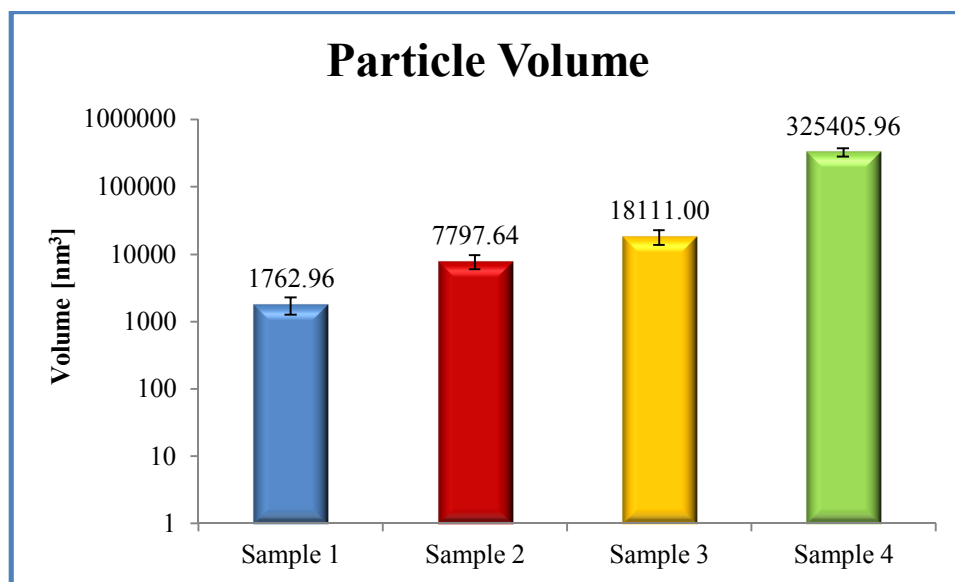
Fig.4-6. Average particle volume of each sample.
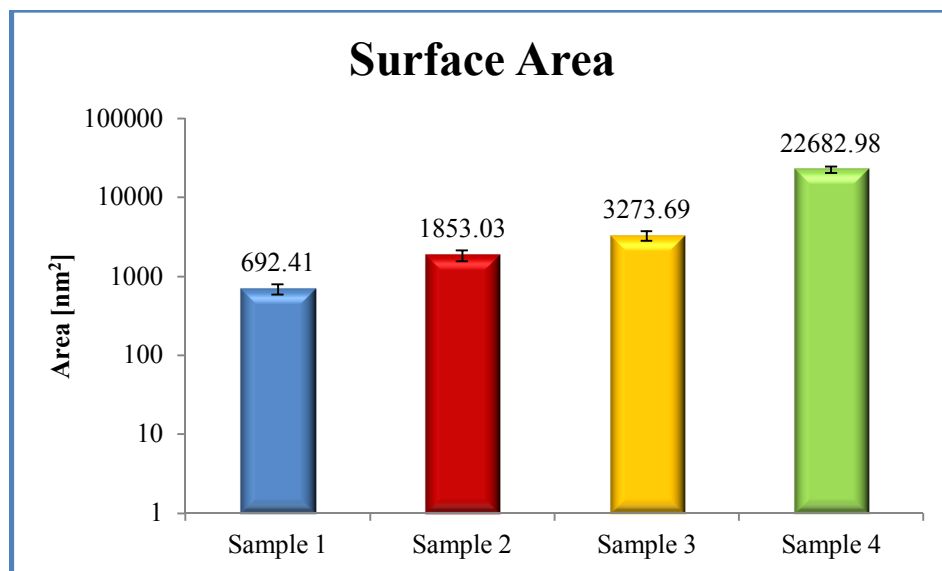
Fig.4-7. Surface area of each sample particle.
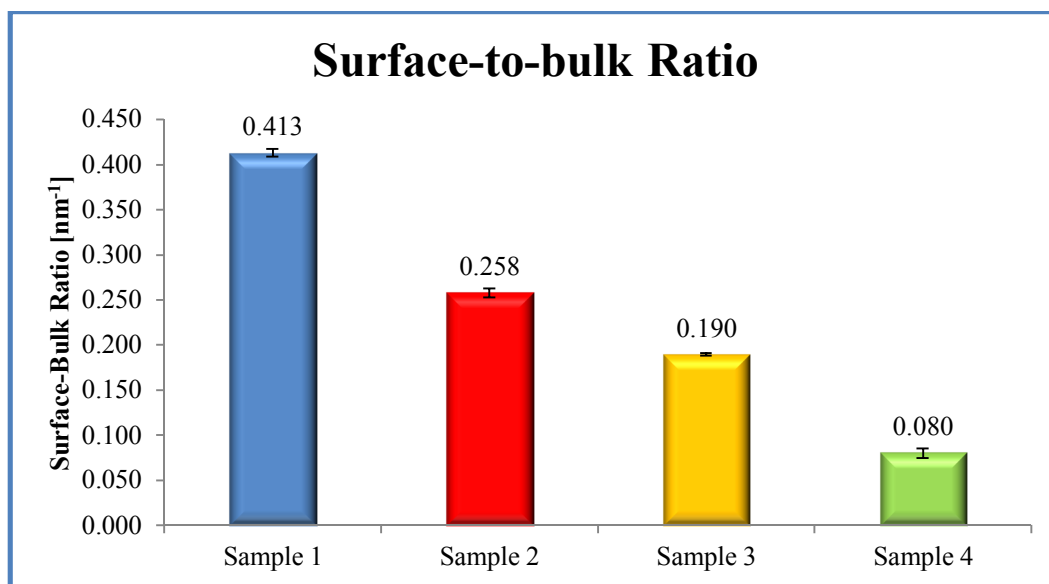
Fig.4-8. Surface-to-bulk ratio of each sample particle.

4.2. Differential Scanning Calorimetry-Thermogravimetric Analysis (DSC-TGA)

According to the DSC-TGA, weight and heat flow were plotted as shown in **Fig.4-9**. In this figure, the first trial result of the sample 1 was labeled as the same. The weight curve shows the weight of the tested remained in the sample holding pan. For heat flow curve in each plot, the positive value of the curve is the heat out-flow (exothermic process, dissipation) and the negative one is the in-flow (endothermic process, absorption) of the sample system.
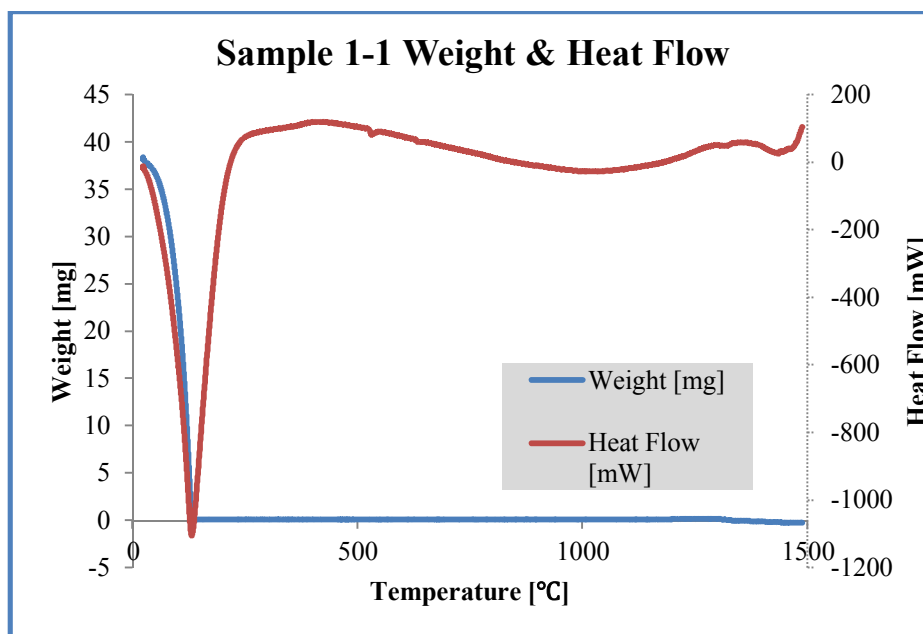
Fig.4-9. Weight and heat flow plots of DSC-TGA result (sample 1, trial 1).

4.2.1. Critical points identification

In **Fig.4-10**, four particular points are designated as points of interest. **A** is the point in sample weight loss at which the weight becomes stabilized due to the water drying out. Point **B** is the first critical point of heat flow curve and it is related to water vaporization (boiling point). Point **C** is the second critical point and it is regarded as an inflection point between two negative critical points, which are the points of phase changes. It will be used for energy calculation as a pivoting value of heat flow. Lastly, the third critical point **D** is related to the fusion of AuNPs. This point will be compared with the size dependent melting temperature of the AuNPs. Point **A** was found by tracing the values of weight derivatives by temperature, and the point has the derivative higher than -0.001 mg/°C. **B** was found by detecting minimum value of heat flow from 100 °C

to 200 °C. **C** is the maximum value found from 350 °C to 450 °C. The point **D** is the

minimum value detected from 1000 °C to 1100 °C. These critical points for each test are

tabled in **Table 4-2**.

Sample 1-1 Weight and Heat Flow

Point **C**

Point **D**

Point **A**

Point **B**

Weight [mg]

Heat Flow [mW]

Weight [mg]

Heat Flow [mW]

Temperature [°C]
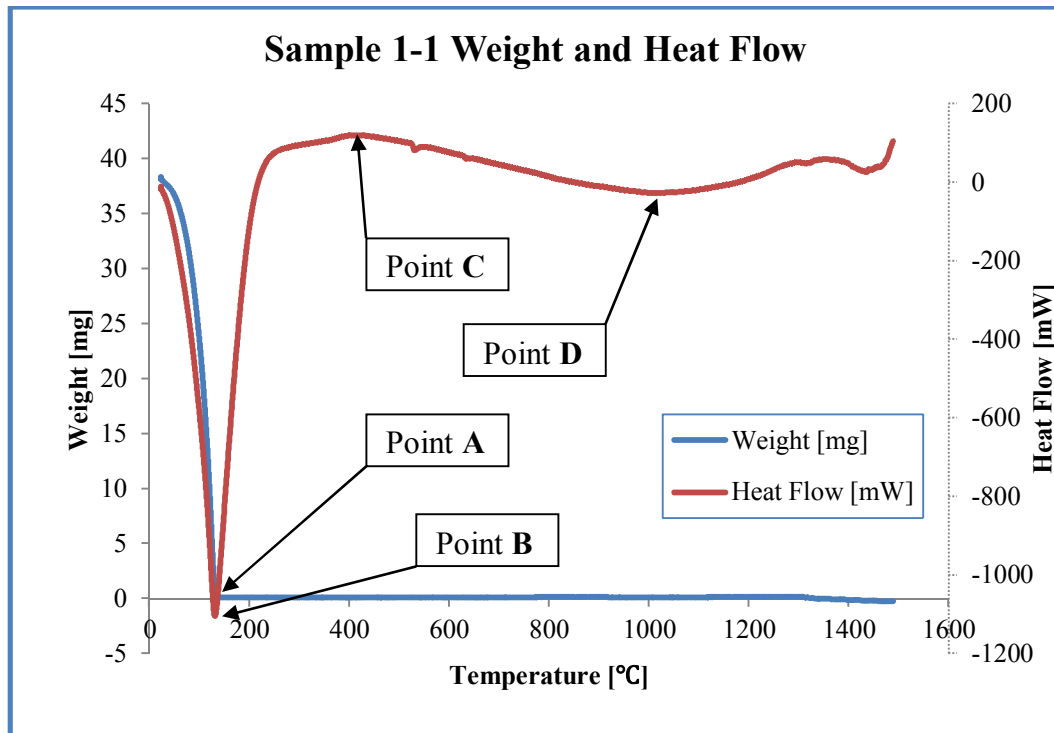
Fig.4-10. Critical points designation from the test plot.

Table 4-2. The critical points.

Sample Num.-Test Num.	Point **A**			Point **B**		Point **C**		Point **D**	
	T [°C]	m [mg]	dm/dT [mg/°C]	T [°C]	h [mW]	T [°C]	h [mW]	T [°C]	h [mW]
1-1	136.5213	0.13091	-0.00092	131.17	-1104.52	412.7725	120.3149	1019.386	-26.8689
1-2	136.9044	0.38532	-0.00025	134.0517	-1191.58	421.9724	126.8297	1048.226	-22.1915
1-3	133.6766	-0.0235	0.000759	131.7084	-1017.68	414.359	132.7441	1032.513	-9.2104
1-4	129.2883	-0.0951	0.000374	131.7084	-1067.55	390.3317	121.9564	1032.513	-25.7694
Average1	134.0977	0.0994	-9.25E-06	132.1596	-1095.33	409.8589	125.4613	1033.16	-21.0100
Standard Deviation	3.514686	0.2127	0.0007359	1.2867	73.37041	13.62337	5.5881	11.79752	8.1159
2-1	138.3079	-0.1653	-0.00019	135.3769	-1265.38	418.0075	127.8698	1050.537	-31.013
2-2	136.0499	0.0046	0.000198	132.9302	-1301.08	411.6174	126.0094	1056.501	-36.8223
2-3	130.0404	0.2005	-0.00077	127.1462	-1138.94	417.473	122.3157	1047.573	-37.5265
2-4	134.0258	-0.05847	0.000549	131.4878	-1228.97	396.4848	151.3133	1069.823	-3.2788
Average2	134.606	-0.0047	-5.33E-05	131.7353	-1233.59	410.8957	131.8771	1056.109	-27.1601
Standard Deviation	3.510459	0.1537	0.0005652	3.4550	69.63175	10.03383	13.1615	9.868096	16.1862
3-1	131.9861	-0.0472	-0.00093	127.7568	-1093.27	419.5156	127.1507	1030.513	-18.3698
3-2	138.7218	0.15142	-0.00097	132.4432	-1361.01	415.0053	127.6801	1054.04	-33.6006
3-3	134.1232	0.53627	-0.000049	131.5698	-1373.78	414.5567	127.2276	1042.583	-38.5700
3-4	129.8794	0.12960	-0.00064	127.477	-1134.87	386.5646	137.0437	1043.672	-31.9419
Average3	133.6776	0.19252	-0.000647	129.8117	-1240.73	408.9106	129.7755	1042.702	-30.6206
Standard Deviation	3.782856	0.24582	0.0004251	2.56185	147.3348	15.06468	4.8511	9.627686	8.6391
4-1	129.5259	0.10096	0.000514	127.4028	-1084.69	416.533	127.5703	1030.198	-19.1363
4-2	133.1756	0.02875	-0.00097	128.1814	-1102.2	419.5497	119.4715	1029.435	-29.1405
4-3	132.9986	-0.04889	-0.00048	129.8973	-1243.01	409.7353	113.9191	1035.105	-52.8258
4-4	130.5588	-0.03461	-0.00085	128.1424	-1175.71	391.2229	120.4181	1047.816	-54.8492
Average4	131.5647	0.01155	-0.000447	128.406	-1151.4	409.2602	120.3448	1035.639	-38.9879
Standard Deviation	1.809199	0.06849	0.0006734	1.0568	72.69616	12.70613	5.6055	8.498207	17.6458

4.2.2. Melting temperature of gold nanoparticles

It has been reported that the size of AuNPs influenced their melting temperatures [58-59]. The temperature of point **D** in **Fig.4-10** is melting temperature. The size dependence on melting temperature is given by equation (4.1),

$$\frac{T_m(r)}{T_m(\infty)} = 1 - \frac{4}{\rho_s L}\{\gamma_s - \gamma_l(\frac{\rho_s}{\rho_l})^{2/3}\}\frac{1}{d} \qquad (4.1)$$

here the variables of the equation is as follows: $T_m(r)$ is the melting temperature of a particle whose radius is r; $T_m(\infty)$ is the melting temperature of the bulk; ρ_s and ρ_l are the densities of the solid and liquid form of the material, respectively; γ_s and γ_l are the surface free energies of the solid and liquid state, respectively; L is the molar heat of fusion; and d is the size (diameter) of the particle. For gold, $T_m(\infty) = 1337.15$ K, $\rho_s = 19$ g/cm^3, $\rho_l = 17.3$ g/cm^3, $\gamma_s = 0.9\times10^3$ erg/cm^2, $\gamma_l = 0.74\times10^3$ erg/cm^2, and L=5.38$\times10^8$ erg/g. The melting temperature calculated using each sample by the equation above is shown in **Fig.4-11**. In order to identify factors affect the melting point, a parameter, the surface-to-bulk ratio was calculated and compared with the temperature of point **D** in **Fig.4-12**.
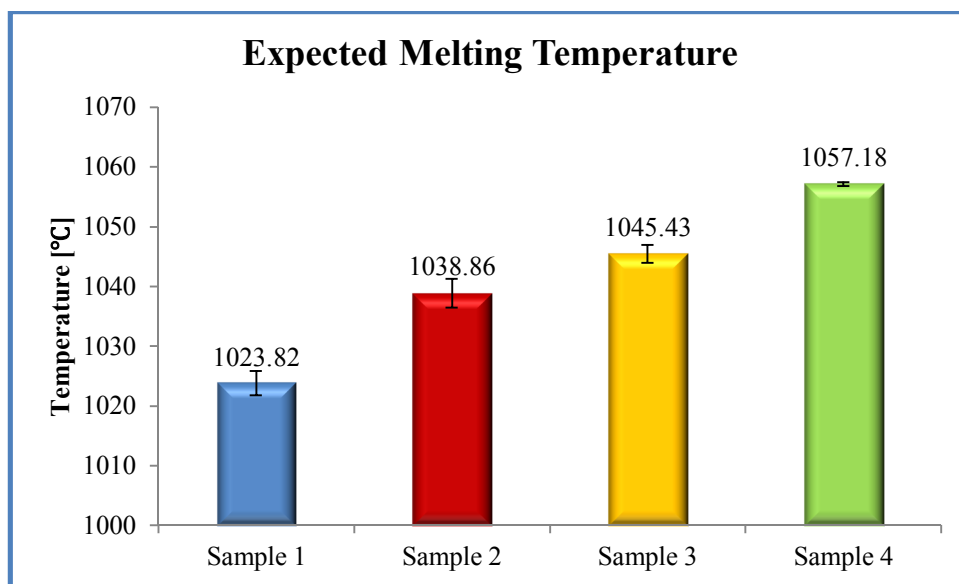
Fig.4-11. Expected melting temperature of each sample.
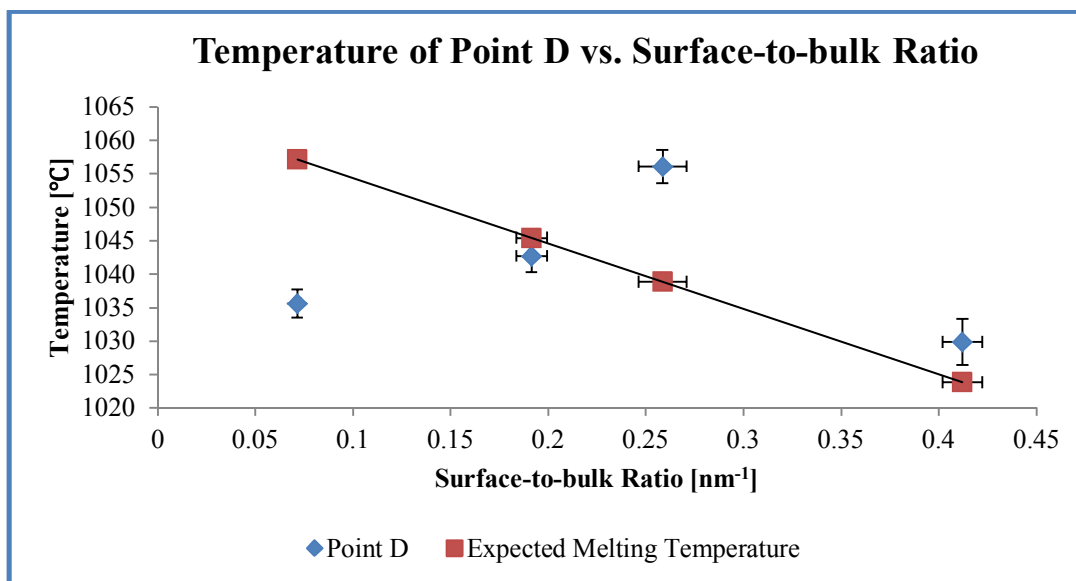
Fig.4-12. Temperature of point D and expected fusion versus surface-to-bulk ratio.

The figure above shows that the melting temperature and the temperature of critical point **D** approach within 25 °C from each other. The differences between these points are 6.04 °C, 17.25 °C, -2.72 °C, and -21.54 °C from sample 1 to 4. However, the temperatures of point **D** have no trend as the melting temperatures calculated by equation (4.1). This indicates that the critical points **D** are related to fusion of particles, and the trend of the temperature of D didn't follow the equation (4.1).

4.2.3. Unit heat flow and surface-to-bulk ratio

The heat flow value of each critical point is compared to the surface-to-bulk ratio. For size effect comparison of points **B** and **D**, the heat flow values were collected from different sized samples. The values of heat flow were normalized dividing by their initial test sample weights to remove the effects of initial weight. For point **B**, the heat flow was divided by total initial weight of the sample. For point **D**, the values were divided by the initial weight of AuNPs only, due to the fact that the water in the samples dried out at about the same time as point **A**. The initial weight of AuNPs was calculated using equation (4.2). It was assumed that the density of the AuNPs solution was approximately the same as the pure water.

$$\text{AuNPs weight} = \frac{246.208211\ [\text{mg}] \times \text{Total weight of tested solution}\ [\text{mg}]}{\text{Synthesized total weight of AuNPs solution}\ (50 \times 1000)\ [\text{mg}]} \quad (4.2)$$

As **Figs. 4-13** and **4-14** show, for point **B**, the unit heat flow linearly decreases as the surface-to-bulk ratio increases, and the trend of point **D** has a logarithmic decrease.

These two graphs indicate that the surface effect decreases the heat flow, which causes

the phase changes of the AuNPs system.
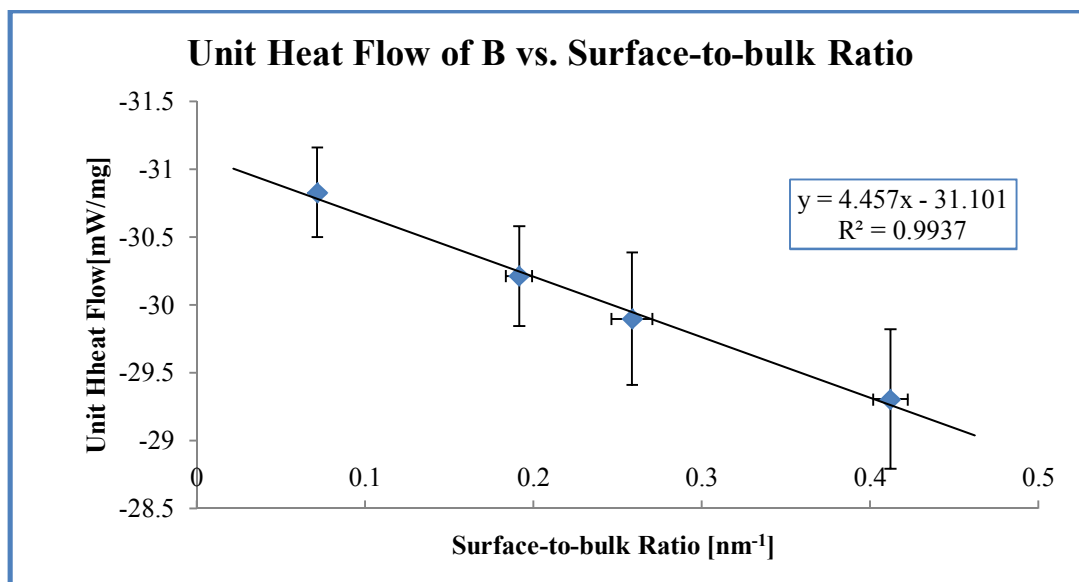
Fig.4-13. Unit heat flow of B versus surface-to-bulk ratio.
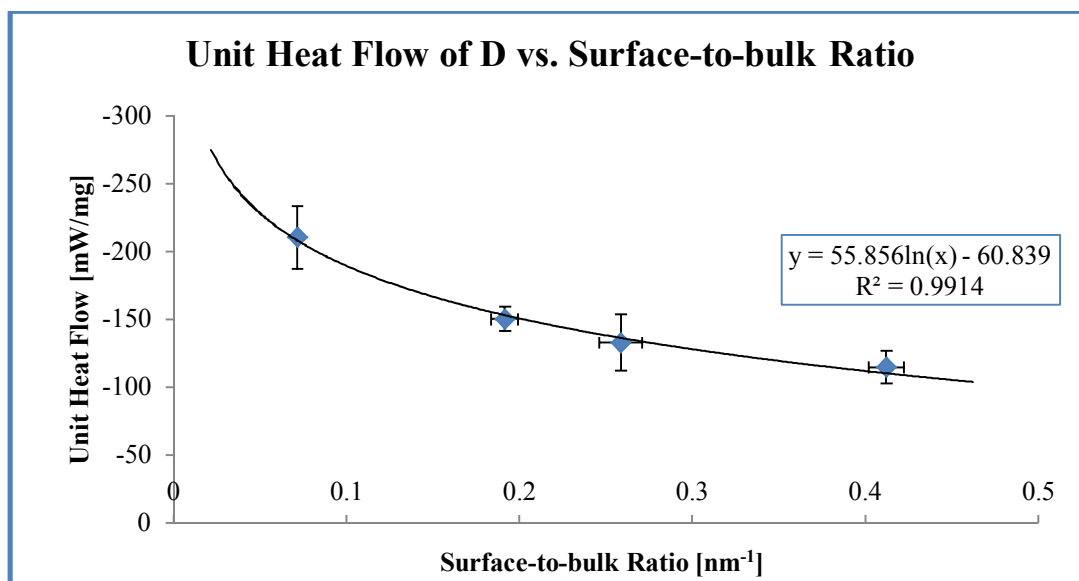
Fig.4-14. Unit heat flow of D versus surface-to-bulk ratio.

4.2.4. Energy analysis

Using the heat flow and time parameters, the energy calculation was conducted through approximated integration, Riemann sum. According to the plot of heat flow, the water vaporization and the particle fusion were identifiable through critical points **B** and **D**. The energy calculations were completed focusing on these two critical points. The heat flow value of point **C** was used as the pivoting point for the calculations.

Two areas were designated as shown in **Fig. 4-15**. The blue area (Area 1) is related to the water vaporization and the yellow area (Area 2) is related to the AuNPs fusion. Area 1 was calculated by right Riemann sum for the time period corresponding to the test temperature from 35 °C to the test temperature of point **C**. Energy calculation of Area 2 utilized the Dirac delta function simulation by the assumption that the fusion effect constructs the heat flow curve with the unitary peak. This is because the curve patterns around 1400 °C affect the calculation of energy without the simulation. The Dirac delta function is expressed in equation (4.3) below.
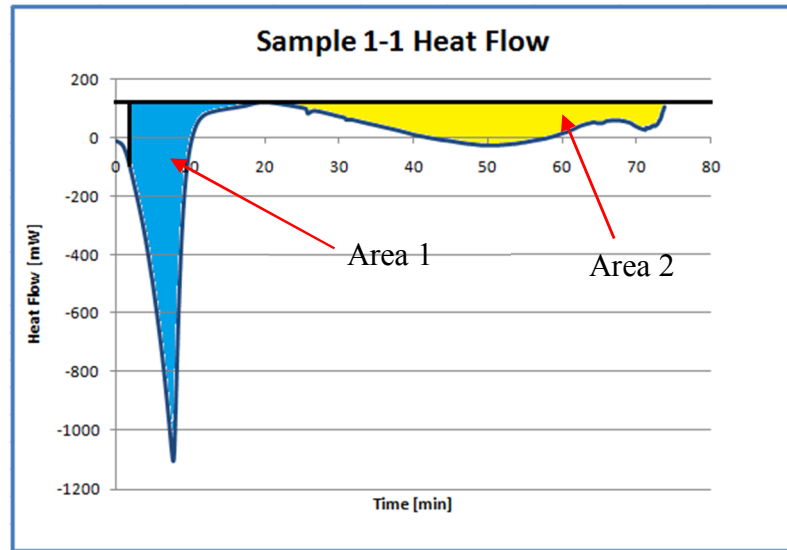
Fig.4-15. Designating two energy calculation areas. The blue area (Area 1) is related to the water vaporization and the yellow area (Area 2) is related to the particle fusion.

$$\delta_a\,(x) = \frac{1}{a\sqrt{\pi}}\ e\ \hat{}\ \text{-}\ \frac{x^2}{a^2} \tag{4.3}$$

where **a** is a constant decides the height and width of the function plot. To make this equation similar to the experimental curve, this equation was changed as follows,

$$\delta_a\,(T - T_D) = \frac{1}{a\sqrt{\pi}}\ e\ \hat{}\ \text{-}\frac{(T - T_D)^2}{a^2} \tag{4.4}$$

Here T is the independent variable (Temperature), and T_D is the temperature of point **D**. This equation changed the location of peak point from zero to the temperature of point **D** by x-axis translational movement, **a** was linearly adjusted from the temperature period value measured from **C** to **D**, and the value of **b** was numerically defined in order to

adjust the height of the peak point to be equal to the heat flow value of **D** subtracted from the heat flow value of **C**. After the simulation, the energy related to the particle fusion was calculated by the right Riemann sum for the total test time. The energies calculated from each test trial are summarized in **Table 4-3**.

Table 4-3. Calculated energies from trials of samples.

	Energy [mJ]			
Sample 1	Trial 1	Trial 2	Trial 3	Trial 4
Area 1	325117.26	351903.8	310630.64	274409.29
Area 2	266576.02	274753.08	260151.21	275821.95
Sample 2	Trial 1	Trial 2	Trial 3	Trial 4
Area 1	386991.56	385877.11	324430.99	326435.57
Area 2	294964.15	306363.09	296063.29	299406.7
Sample 3	Trial 1	Trial 2	Trial 3	Trial 4
Area 1	329085.11	403606.74	399133.66	291787.18
Area 2	264215.82	301481.41	306817.98	324528.9
Sample 4	Trial 1	Trial 2	Trial 3	Trial 4
Area 1	315209.72	328069.97	355912.05	301771.58
Area 2	267374.61	269460.2	308256.59	335801.42

The calculated energy was normalized by the initial weight of samples in order to find the effect of surface propertiy on the phase change. For normalization, the energy of Area 1 was divided by the initial sample weight and the energy of Area 2 was divided by the total initial particle weight. The calculated energies are plotted in **Figs. 4-16** and **4-17**. The two plots show that the energies required for the phase changes decrease as surface-to-bulk ratio increases. The unit energy for water vaporization decreases linearly and that of the particle fusion decreases logarithmically, which is the same for the unit heat flow value comparison of point **B** and point **D**.
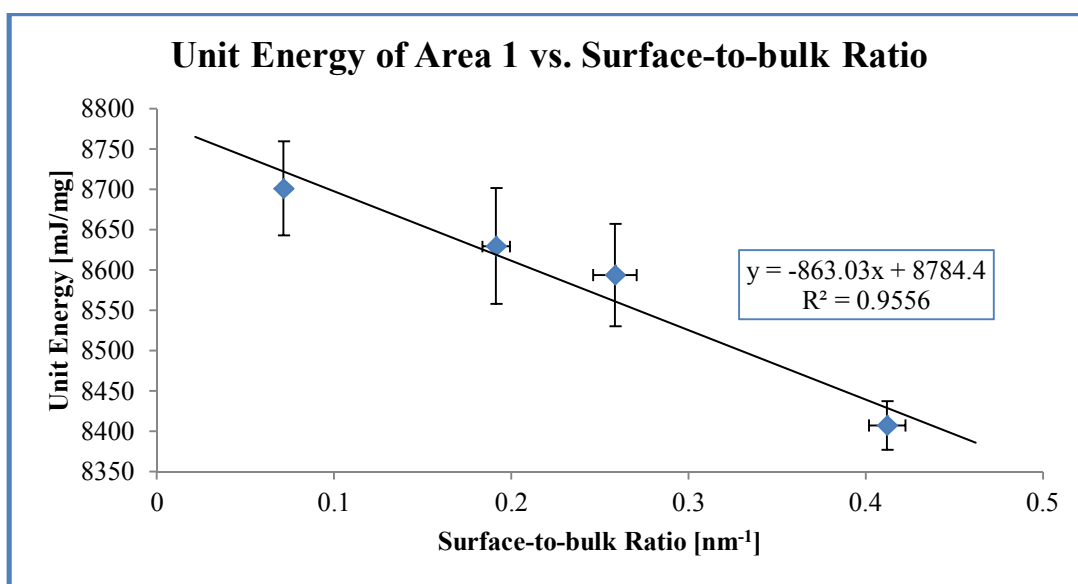
Fig.4-16. Unit energy of Area 1 versus surface-to-bulk ratio.
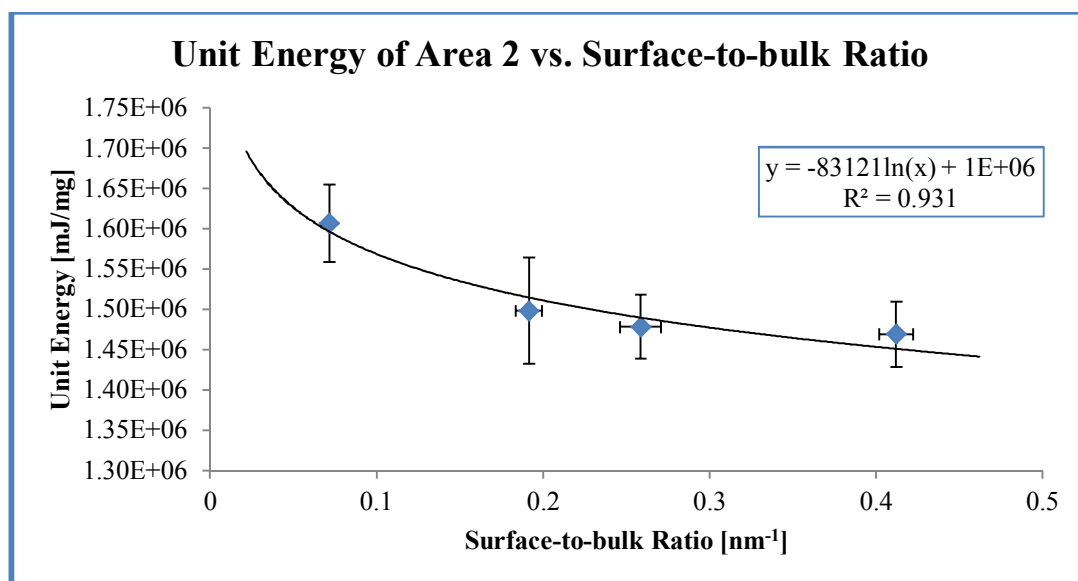
Fig.4-17. Unit energy of AuNPs fusion versus surface-to-bulk ratio.

4.3. Summary

All above discussion has shown that the surface-to-bulk ratio has clear effects on heat flow properties such as melting temperature, heat flow, and energy related to the phase change. The unit heat flow and energies decreased as the surface-to-bulk ratio increased. However, the critical point of **D** didn't show any size dependency of melting temperature.

CHAPTER V

TRIBOLOGICAL PROPERTIES OF MICROARC OXIDIZED COATINGS ON MAGNESIUM

This chapter discusses tribological behavior of surface coatings fabricated through microarc oxidation (MAO). The tribology and corrosion experiments will be conducted and results are discussed. The tribotests results are described in terms of friction coefficient, wear rate, and worn surfaces observation. Corrosion test result is shown by the tafel plot drawn by the two parameters, i.e., potential measured from the reference electrolyte and current density.

The tribological performance will be discussed in relation with surface properties, such as roughness and hardness.

5.1. Frictional Performance

The average friction coefficient results are shown in **Fig.5-1**. It can be seen that the friction coefficient of the uncoated magnesium substrate is lower than that of the coated samples. The Vickers hardness of the pure magnesium substrate is 40 HV, which is lower than that of the MAO coatings. This means that the magnesium substrate is abraded easily in comparison with coated ones. The low resistance of a soft material against sliding is expected to lead to low friction.

The hardness of samples of 1C is almost two times as that of samples of 2C.

However, there is no significant difference of the friction coefficient between these two groups. This indicates that the resistance of the coating materials to the sliding pin is similar to all samples. In comparison of the surface roughness of each pair, samples of 1C and 2C, the smother surface seems to present low friction.
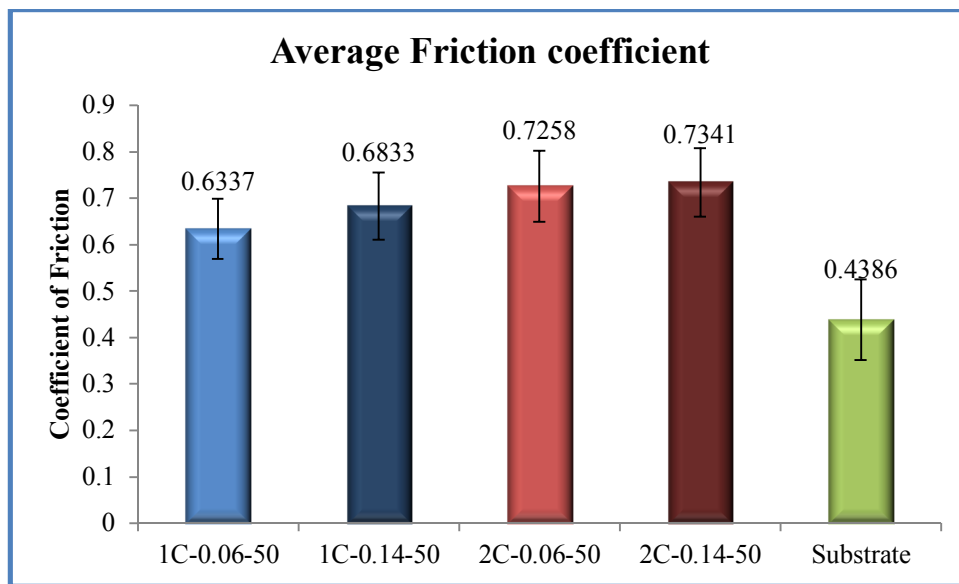
Fig.5-1. Average coefficient of friction of the linearly increased period.

5.2. Wear

After friction tests, the Keyence VHX-600K optical microscope was used to characterize the wear scars on the balls and wear tracks on the coated disks. The volumes of the wear scars were calculated by measuring their diameters. The profile of each wear track was measured by using the profilometer.

The wear scars on the balls are shown in **Fig.5-2**. Scratches can be seen clearly on all balls rubbed with coated samples. However, on the ball rubbed with the bare

magnesium substrate, no apparent scratch can be seen. This is consistent with our observation of low friction where the bare metal disk is expected to be abraded. In this figure, the ball is hardly worn while the debris is adhered to the ball surface. The debris is seen as the dark areas on the wear scar.
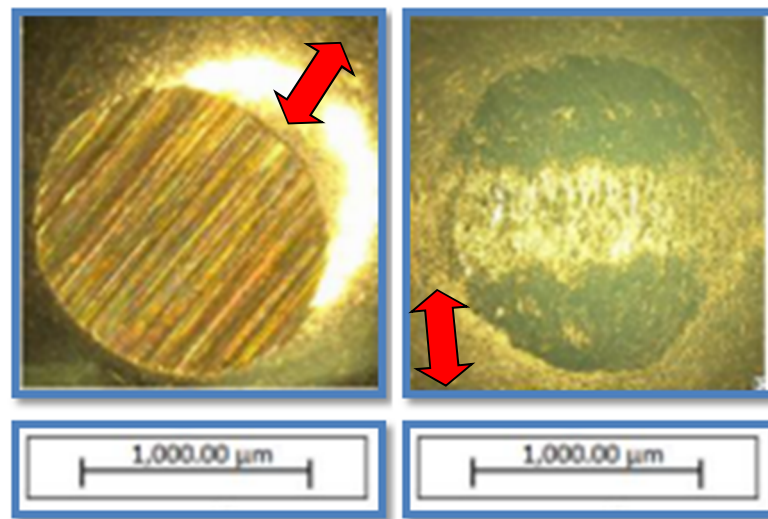
Fig.5-2. Counter partner surface micrographs of sample 1C-0.06 (left) and the uncoated substrate (right). The direction of grooves of the left micrograph indicates the sliding direction of the tribotest. For the micrograph of the right, black areas are the adhesion area and the debris was attached from the sample's end of the wear track.

In order to quantify the wear scars on the balls, the volume of each scar was calculated measured wear scar diameter as **Fig.5-3**. All scars were elliptical due to the alignment of the optical lens. For convenience, it was assumed that the scars were round and its diameter was the average of the major and minor diameters of the ellipse. The volume of the scar on the ball rubbed with the substrate was not measurable. **Fig.5-4** shows the volume of each wear scar on the balls. The volumes of the wear scars on

samples of 1C are bigger than those on samples of 2C. More material was worn from the balls rubbed with samples of 1C than from those of 2C due to the higher hardness of the corresponding coatings. This is in correlation with our observation in friction as discussed above.
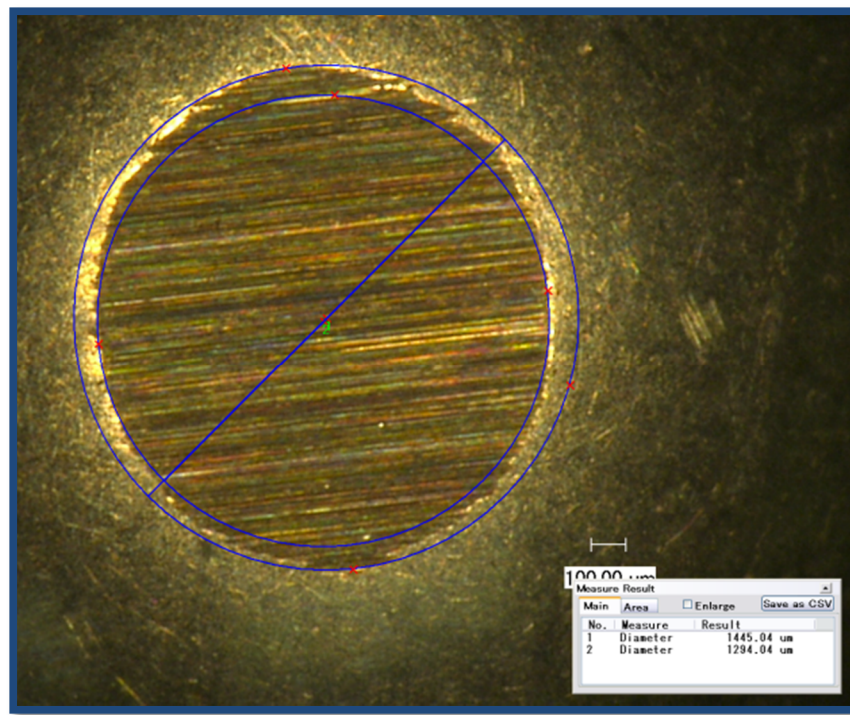
Fig.5-3. The worn surface diameter measurements of the counter scanning partner.
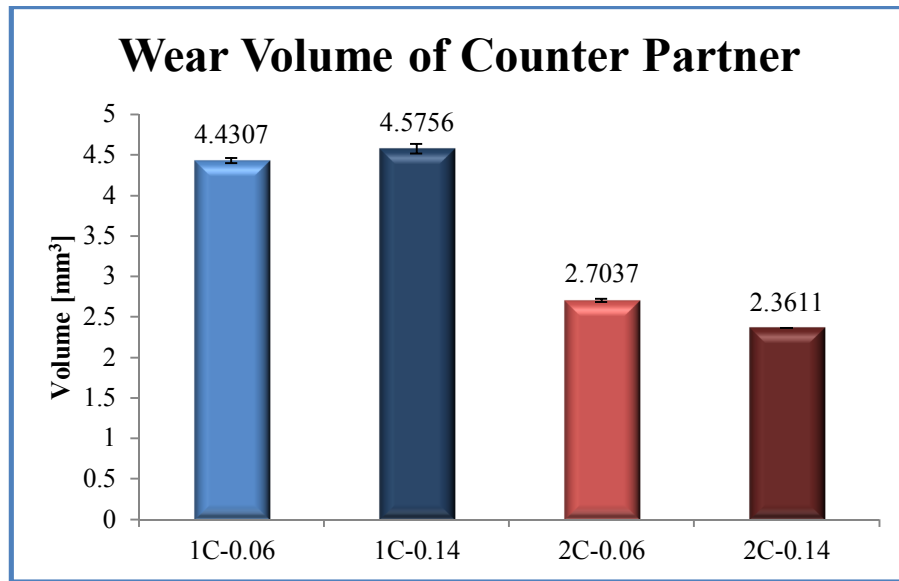
Fig.5-4. Wear volumes of the tested counter partners.

The profiles of the wear tracks on samples 1C-0.06, 2C-0.06, and uncoated substrate are shown in **Figs. 5-5, 5-6** and **5-7**. **Fig.5-8** shows the optical micrographs of the wear tracks on samples 1C-0.06 and 2C-0.06 as well as the substrate. Due to the same composition of the coatings on samples of 1C, they have the similar wear patterns. Similar was observed samples of 2C. Here we only show the data of samples 1C-0.06 and 2C-0.06. From the diagrams in **Fig.5-5** and **6**, no wear track was detected by the profilometer. That means that the anti-wear performance of the coatings is pronounced. In the optical pictures shown in **Fig.5-8**, no scratches are found on the coatings of samples 1C-0.06 and 2C-0.06, while on the uncoated substrate, scratches are visible. The black dots on samples 1C-0.06 and 2C-0.06 are wear debris.
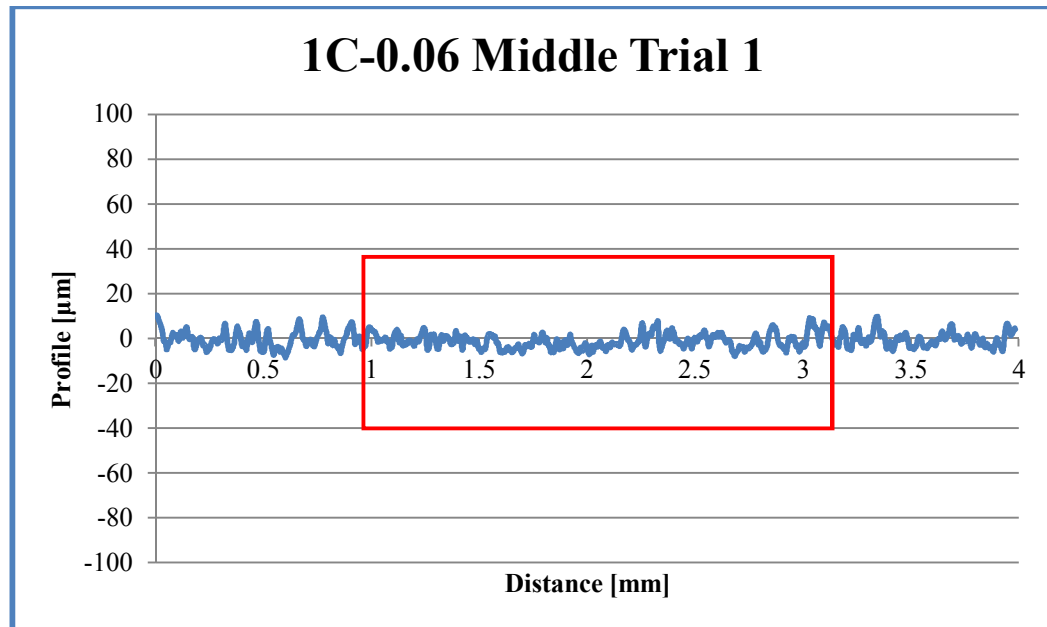
Fig.5-5. Wear track profile of the sample 1C-0.06. Wear track area is signed by a red square. The wear track was found by the less rough surface and the size of tested counter partner's worn surface size.
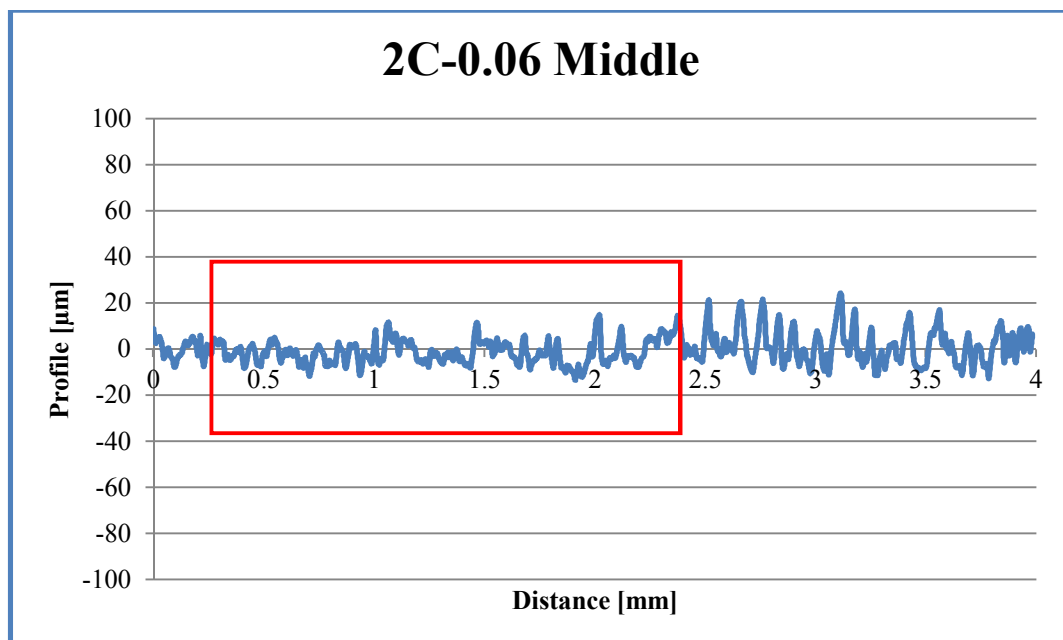
Fig.5-6. Wear track profile of the sample 2C-0.06. Wear track area is signed by a red square. The wear track was found by the less rough surface and the size of tested counter partner's worn surface size.
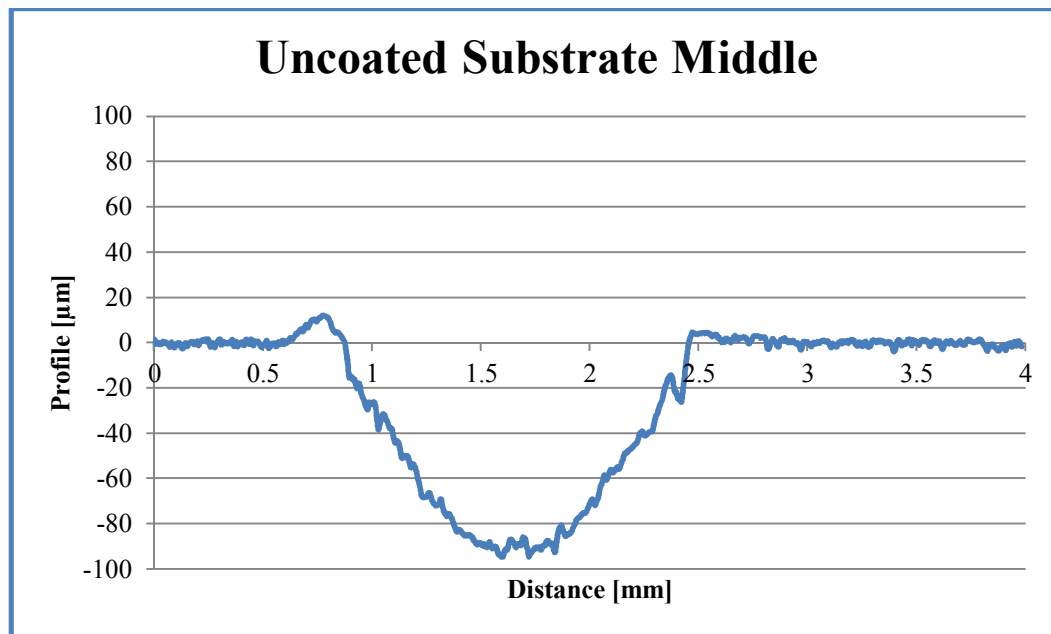
Fig.5-7. Wear track profile of the uncoated substrate.

5.3. Corrosion Test

The potentiodynamic polarization tests were carried out in aqueous NaCl solution. **Fig.5-9** shows the Tafel curves obtained in corrosion tests. The y-axis is the scanning potential, while the x-axis is the reaction current. Corrosion potential is the potential when the corresponding current is the minimum. The corrosion potential indicates the corrosion resistance of the material. The higher the corrosion potential, the better the resistance to corrosion. Additionally, the anodic reaction current which is induced when the scanning potential is higher than the corrosion potential also reflects the corrosion resistance. At the same anodic potential, the lower the reaction current, the better the corrosion resistance.
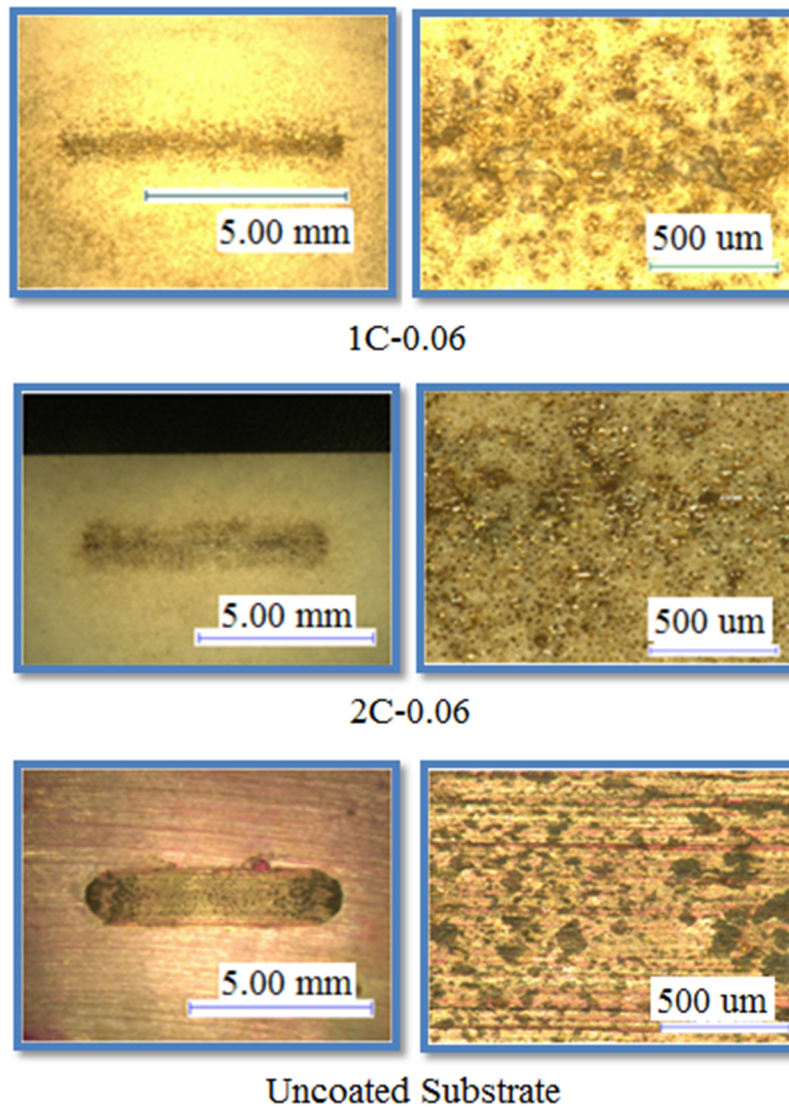
Fig.5-8. Optical micrographs of the wear tracks on the specimens. The magnitude of the left pictures is 20, while the right 200.

Comparing the curves of coated specimen and the bare substrate, the corrosion potential of the latter is lower than that of other samples. Furthermore, the anodic current of the uncoated substrate is higher than that of the coated specimens. That indicates that the corrosion resistance of the coated samples is better than that of the bare magnesium,

showing the anti-corrosion property of the coatings. The composition of the coatings can affect their anti-corrosive performance. The corrosion potentials of samples of 2C are lower than those of samples of 1C. In addition, the anodic current of the former is higher than that of the latter. As a result, the coatings on samples of 2C are not as resistant to corrosion as the coatings on samples of 1C.
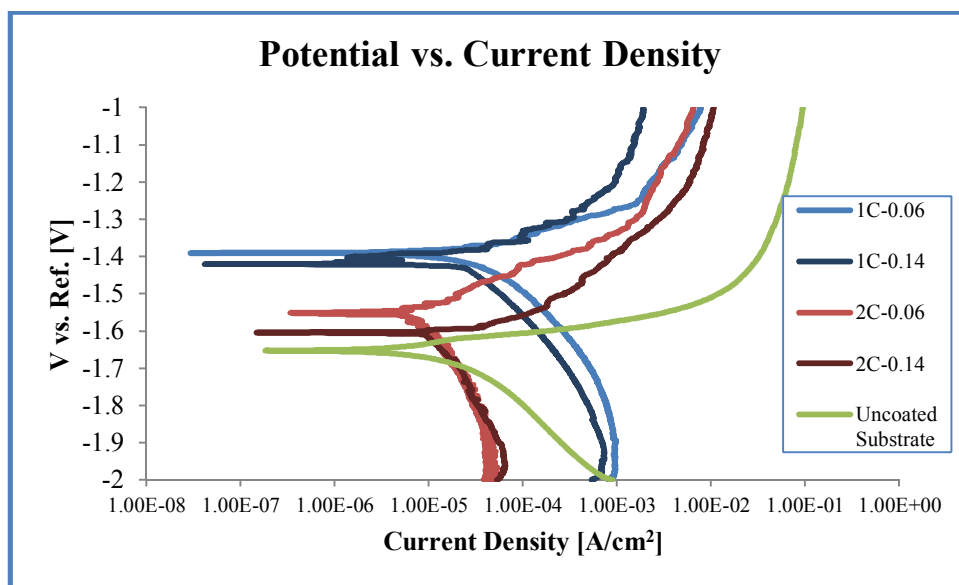
Fig.5-9. Potentiodynamic polarization curves of the coated specimens and substrate.

5.4. Summary

Two different coatings were produced on magnesium substrates by using microarc oxidation. Tribological tests on the coatings were carried out on a pin-on-disk tribometer in dry condition. The anti-corrosive performance of the coatings was examined by conducting potentiodynamic polarization tests. The following conclusions could be obtained:

1. The friction coefficient of the two types of coatings is higher than that of the bare magnesium substrate. The friction coefficient is not a function of coating composition, while it is a function of surface roughness. The lower the roughness, the lower the friction coefficient.

2. The resistance to wear on the coatings is better than pure magnesium due to the higher hardness of the former. No obvious wear track was observed on the coatings after friction tests.

3. The MAO coatings show better resistance to corrosion in aqueous NaCl solution than pure magnesium. Additionally, the coating consisting Mg_2SiO_4 is more resistant to corrosion than that containing $Mg_3(PO_4)_2$.

CHAPTER VI

TRIBOLOGICAL EVALUATION OF SINGLE-CRYSTAL COPPER FILMS

Epitaxial copper films on silicon substrate created by physical vapor deposition method were investigated using a tribological approach. Friction, wear, and surface properties were evaluated to study effects of nanocrystal structures on their tribological behaviors.

It was shown that the wear rate was dependent on the growth direction of single crystal copper films or twinned structures while the coefficient of friction had no visible effects.

6.1. Test Condition Design

In order to initially evaluate the film, the first test of each sample was conducted for 30 minutes and the friction coefficient plots are shown in **Figs. 6-1** and **6-2**. The wear profiles, measured in the direction perpendicular to the sliding direction of the tribotest, are shown in **Fig.6-3**. The profiles indicate that the copper films were broken and the substrates were partly worn. With these wear track profiles, the wear rate of the film could not be evaluated because the film layer was broken. Therefore, a test of shorter duration was required for the evaluation. Before conducting additional tests, the friction coefficient plots were used to analyze the tribological performances.
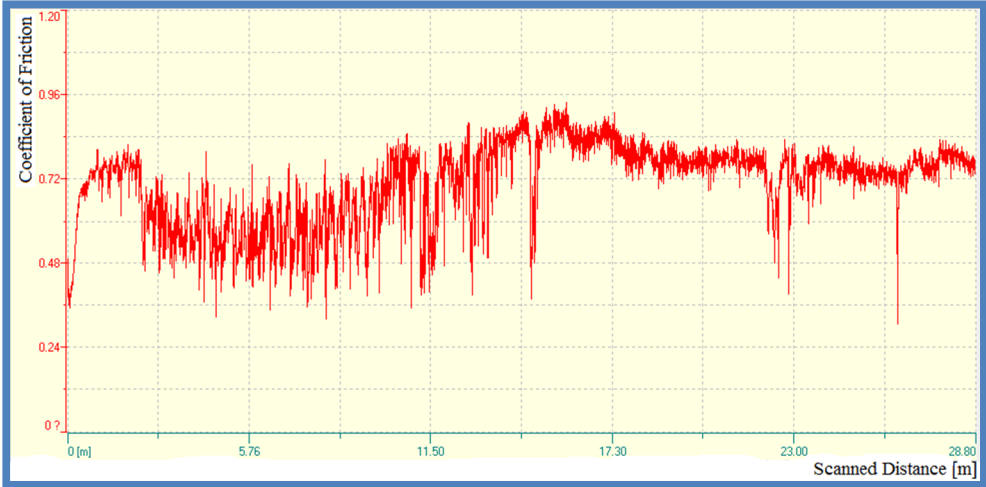
Fig.6-1. Friction plot of the sample Cu100, trial 1.
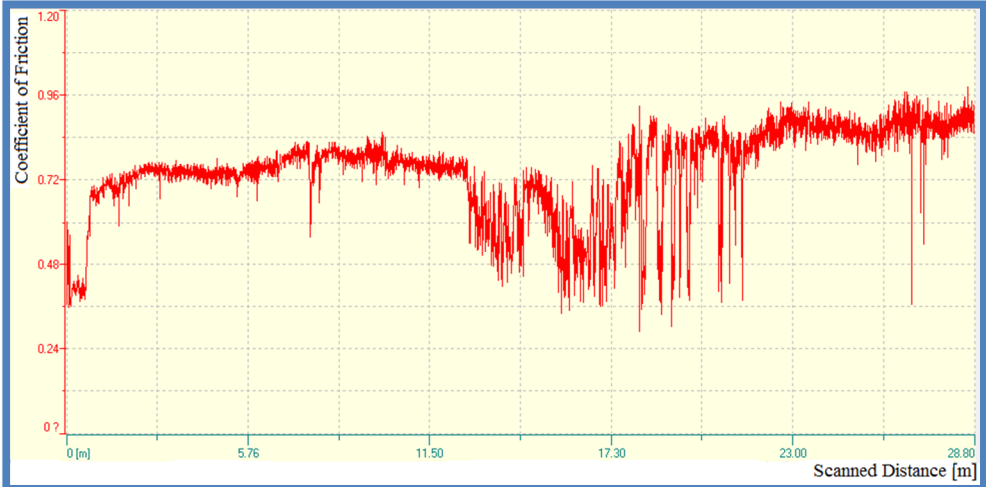
Fig.6-2. Friction plot of the sample Cu111, trial 1.
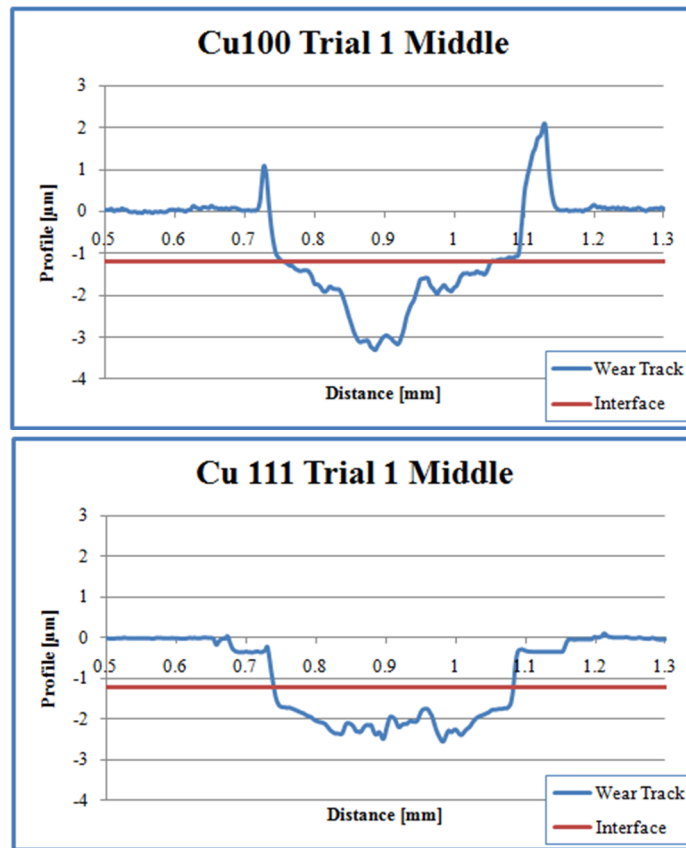
Fig.6-3. Wear track profiles of sample Cu100 and Cu111.

Fig.6-4 divided the friction coefficient into 4 periods: ① initial contact, ② contacting to the copper film, ③ breaking process of copper film (different wear type from the previous period), and ④ contacting the substrate. This dividing method was possible for the friction coefficient plots, which were tested for enough time regardless of sample test results. For friction analysis, the friction coefficient data of period ② were used and the wear rates were tried to be calculated with data from tribotests ending within period ②.
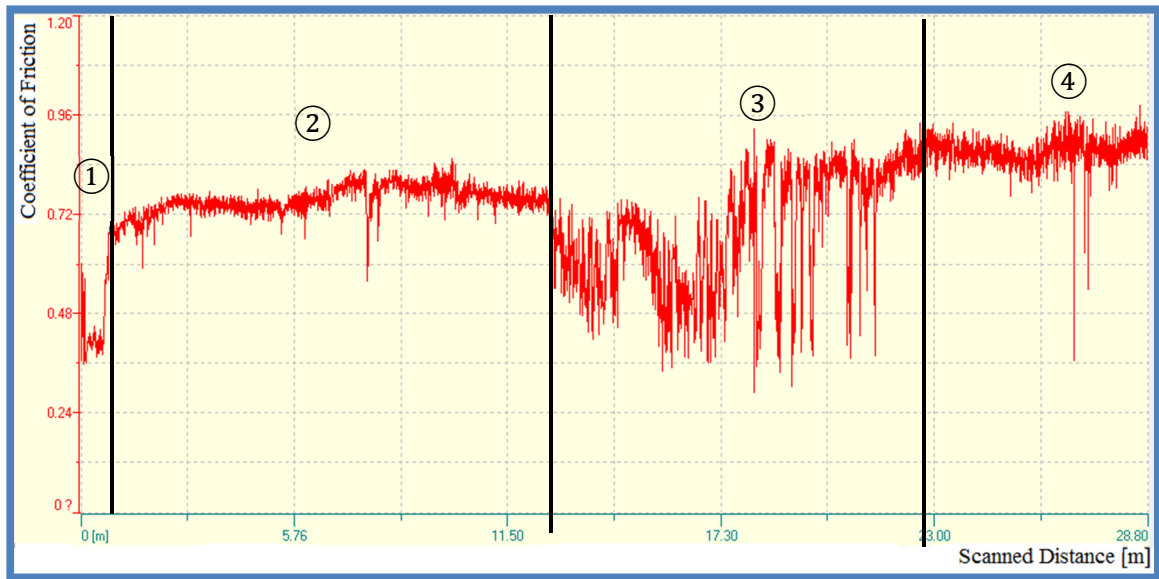
Fig.6-4. Dividing the period of friction coefficient, Cu111 trial 1.

Tribotests were repeated for several times on each sample in different sliding directions. **Fig.6-5** illustrates the wear tracks taken with the optical microscope, and **Table 6-1** lists the test time and sliding distance.
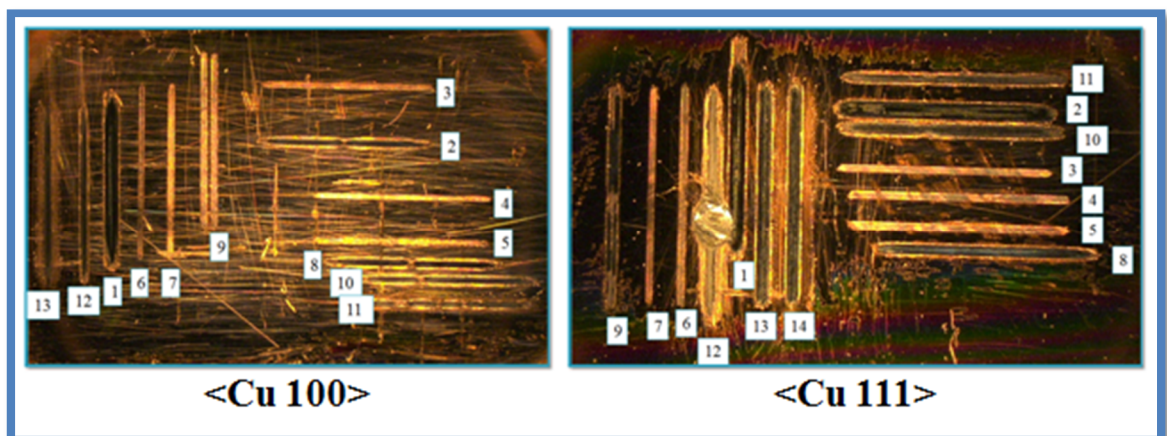
Fig.6-5. Wear tracks taken after total tribotests with 20 magnification.

Table 6-1. Time and sliding distance of each tribotest.

Cu100	Sliding Direction	Tested Time [s]	Sliding Distance [m]	Cu111	Sliding Direction	Tested Time [s]	Sliding Distance [m]
Trial 1	V	1832.49	28.80	Trial 1	V	1823.15	28.80
Trial 2	H	290.53	4.55	Trial 2	H	1831.76	28.77
Trial 3	H	84.22	1.32	Trial 3	H	222.45	3.50
Trial 4	H	82.86	1.30	Trial 4	H	533.41	8.37
Trial 5	H	127.94	2.01	Trial 5	H	193.45	3.04
Trial 6	V	127.18	2.00	Trial 6	V	457.21	7.18
Trial 7	V	118.57	1.86	Trial 7	V	127.02	2.00
Trial 8	H	244.46	3.84	Trial 8	H	611.06	9.60
Trial 9	V	243.94	3.84	Trial 9	V	610.63	9.60
Trial 10	H	244.63	3.84	Trial 10	H	611.56	9.60
Trial 11	H	244.53	3.84	Trial 11	H	611.29	9.60
Trial 12	V	244.46	3.84	Trial 12	V	611.09	9.60
Trial 13	V	244.37	3.84	Trial 13	V	611.13	9.60
				Trial 14	V	610.04	9.60

6.2. Friction Analysis

In each test, the friction coefficient of period ② was averaged. **Figs. 6-6** and **6-7** show the average friction coefficient for each test.
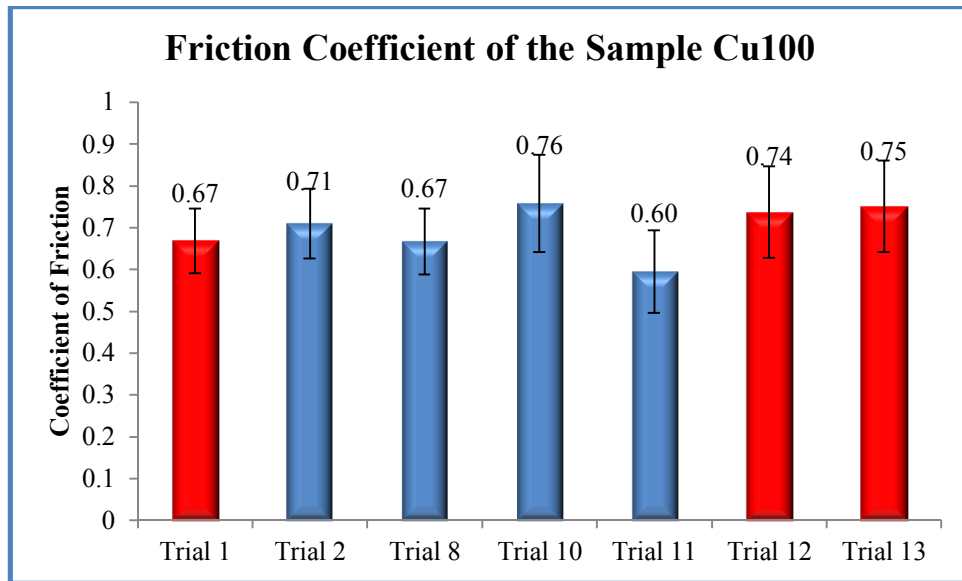
Fig.6-6. Friction coefficient of the sample Cu100. Trials of red bars were tested vertically and the blue ones were tested horizontally shown as Fig.6-5.
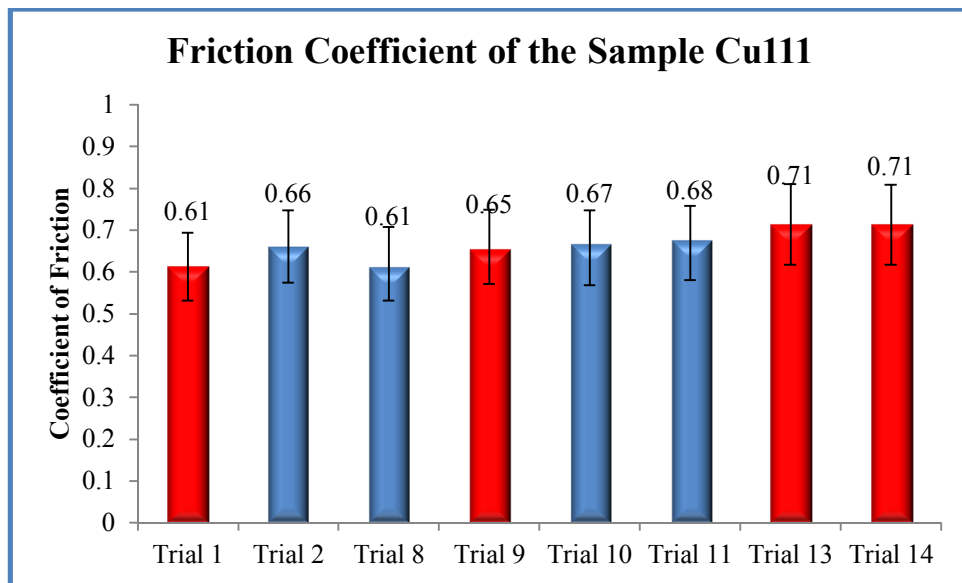
Fig.6-7. Friction coefficient of the sample Cu111. Trials of red bars were tested vertically and the blue ones were tested horizontally shown as Fig.6-5.

6.3. Wear Resistance

Wear rate is computed using equation (1.2). Only trials which sustained the copper film were selected for this calculation. The surface profiles showed no wear track. Rather, the wear track was raised compared with the non-tested surface as shown in **Fig.6-8**.

The wear resistance was compared by measuring the total sliding distance of period ②. The total sliding distance of period ② means the resistance to maintain the coating during the tribotest. **Figs. 6-9** and **6-10** illustrate the sliding distance for each test trial.
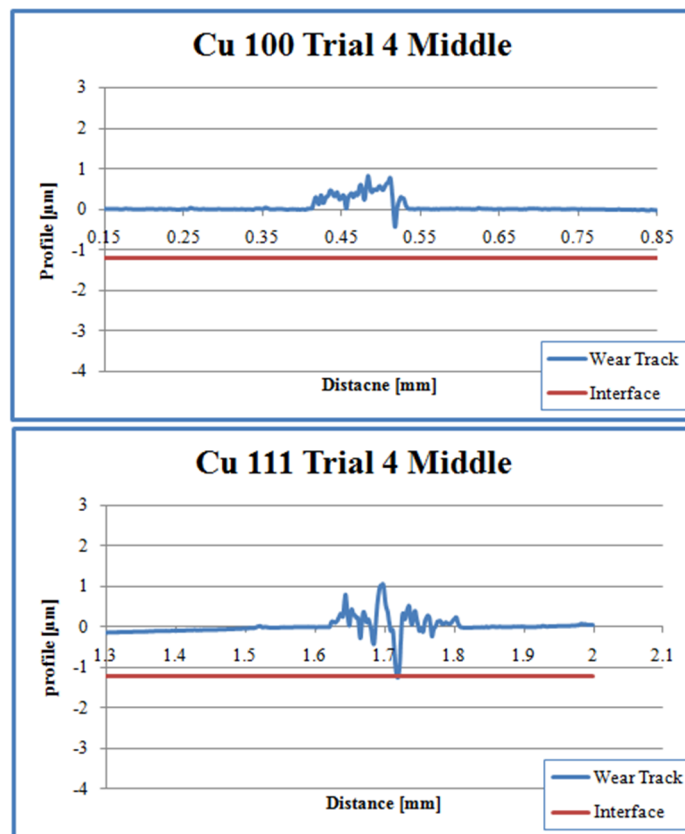
Fig.6-8. Wear track profiles of samples Cu100 and Cu111, trial 4, and sliding in the middle.
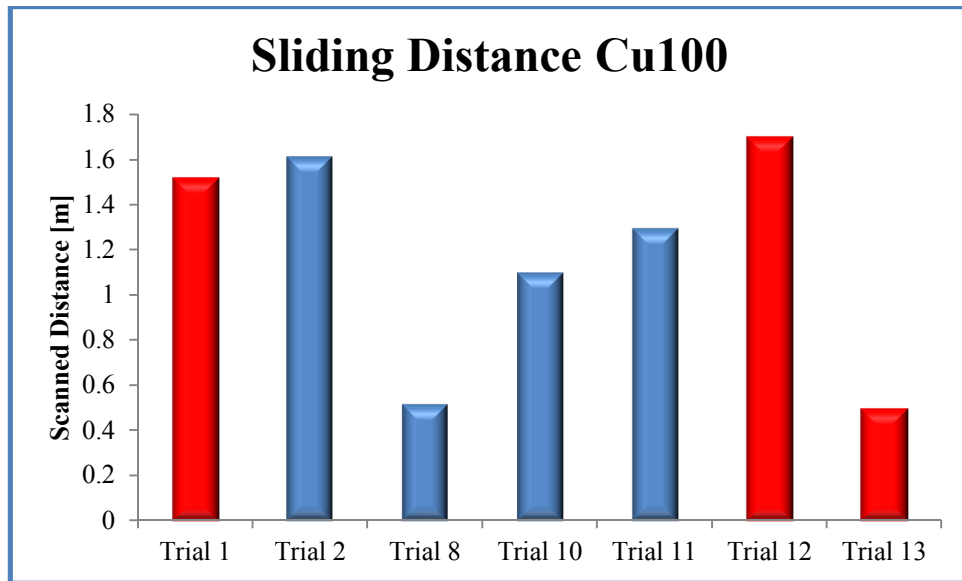
Fig.6-9. Sliding distance of the period ②, Cu100.
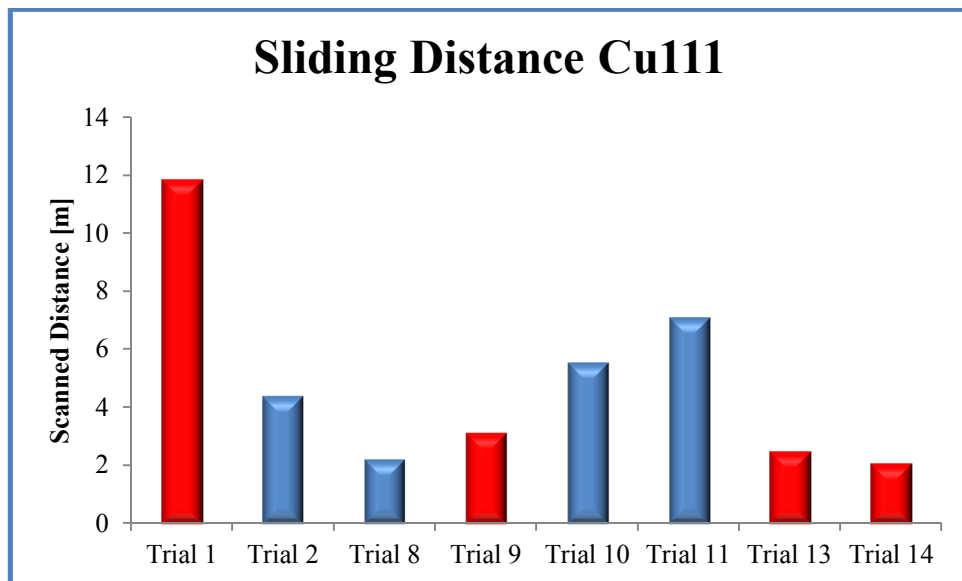
Fig.6-10. Sliding distance of the period ②, Cu111.

6.4. Directional and Structural Effects of Single Crystal Cu Film on Friction and Wear

6.4.1. Directional effects

According to the experimental results, average friction coefficient and the total sustained sliding distance were analyzed against sliding direction. **Fig.6-11** illustrates the average friction coefficient of tribotests with the same sliding direction. **Fig.6-12** shows the average sliding distances of period ② for each sliding direction. **Figs. 6-11** and **6-12** do not demonstrate different tribological properties caused by the different sliding directions. There are two possible reasons for this: the test scale and the test direction. First, the tests were conducted with a macro-scale tribometer. A 6 mm diameter bearing ball was used as a rubbing partner. The macro-scale tribotest is not sensitive to the atomic arrangement difference. Second, under the tribotest conditions, the angle between the two sliding direction was a right angle. For the sample Cu100, there is no difference in the atomic arrangement for the two directions because of the right angle symmetry.
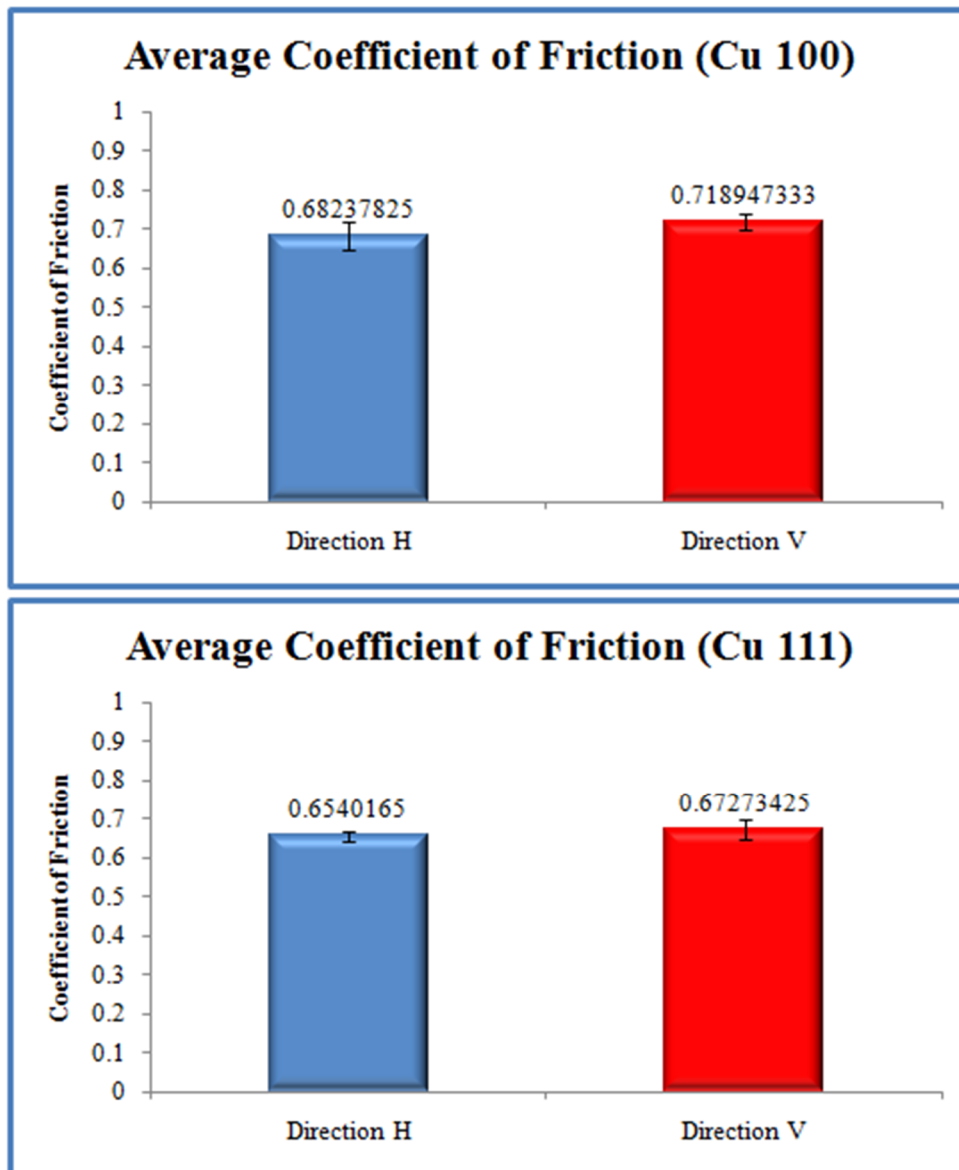
Fig.6-11. Average friction coefficient comparison of different test sliding directions.
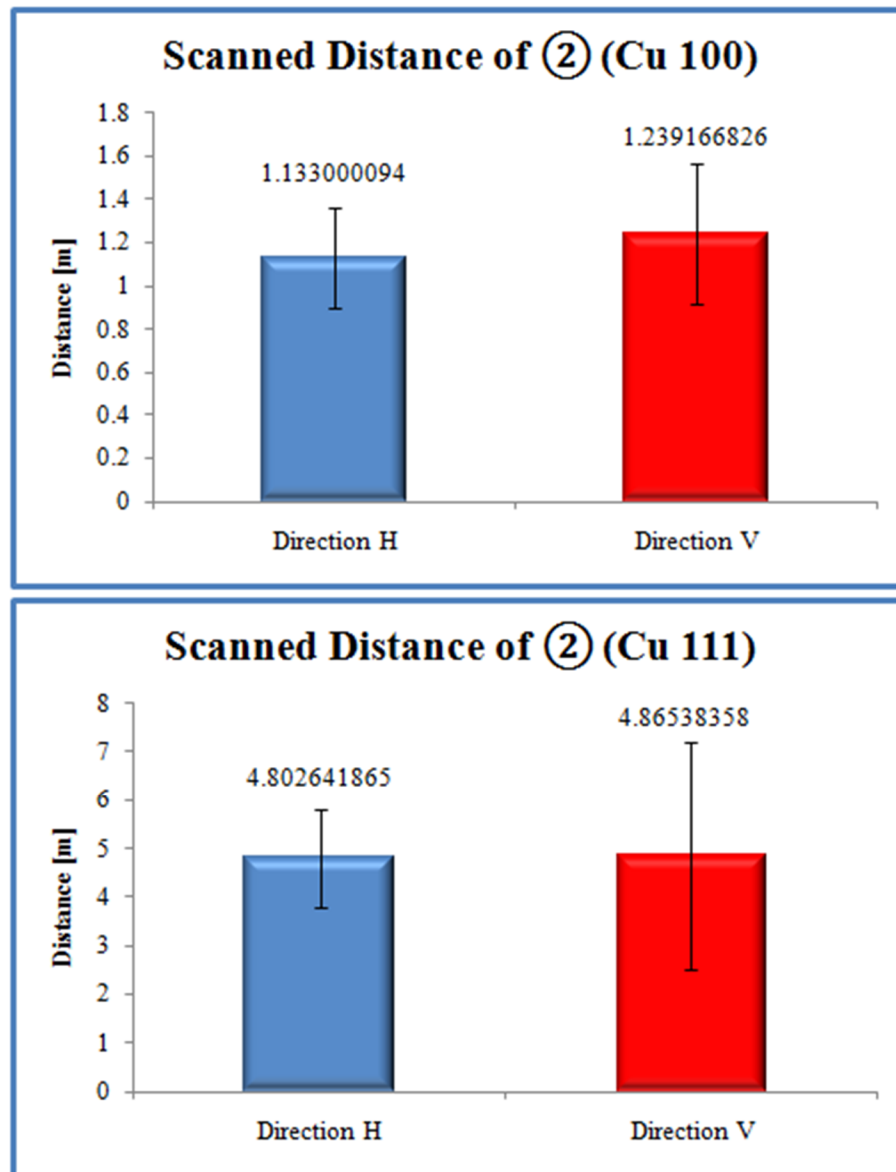
Fig.6-12. Sliding distance of the period ② comparison of different test sliding directions.

6.4.2. Structural effects

The difference between the two samples is the crystal structure. The structural difference of the tribological behaviors was examined by comparing the two tests. Friction coefficient and sliding distance of period ② were used for the comparison.

Sliding direction was not considered in averaging the friction and distance because the sliding directional effects were not found as stated above. **Fig.6-13** compares the average friction coefficient of each sample. The figure shows that the friction coefficient values were not significantly different. In **Fig.6-14**, the sliding distance of period ② was compared. The chart indicates that sample Cu111 achieved a larger sliding distance without breaking into the substrate and is therefore more wear resistant. Therefore, the nano-twinned structure gave no effect in the frictional force but it increased wear resistance.
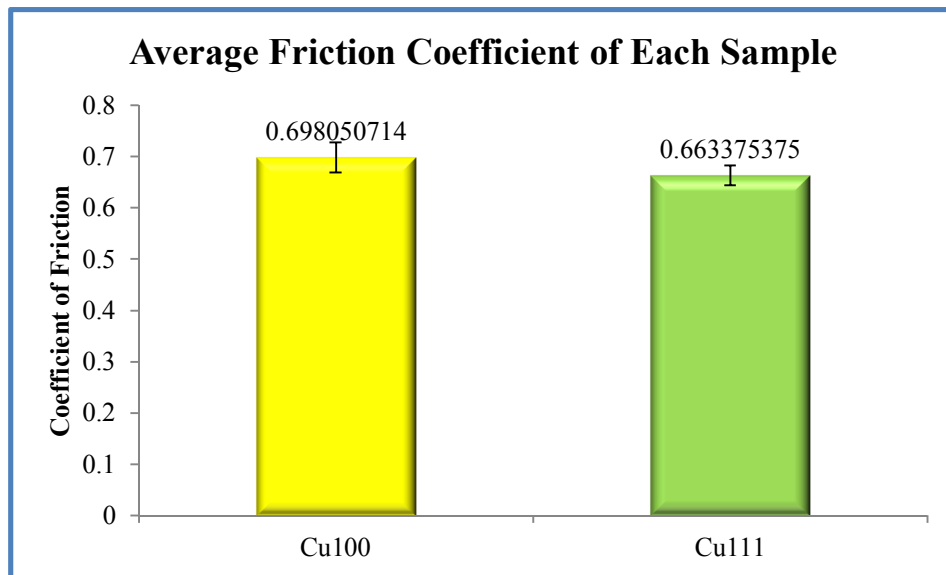
Fig.6-13. Average friction coefficient comparison of different samples.

Average Total Sliding Distance of the period ②
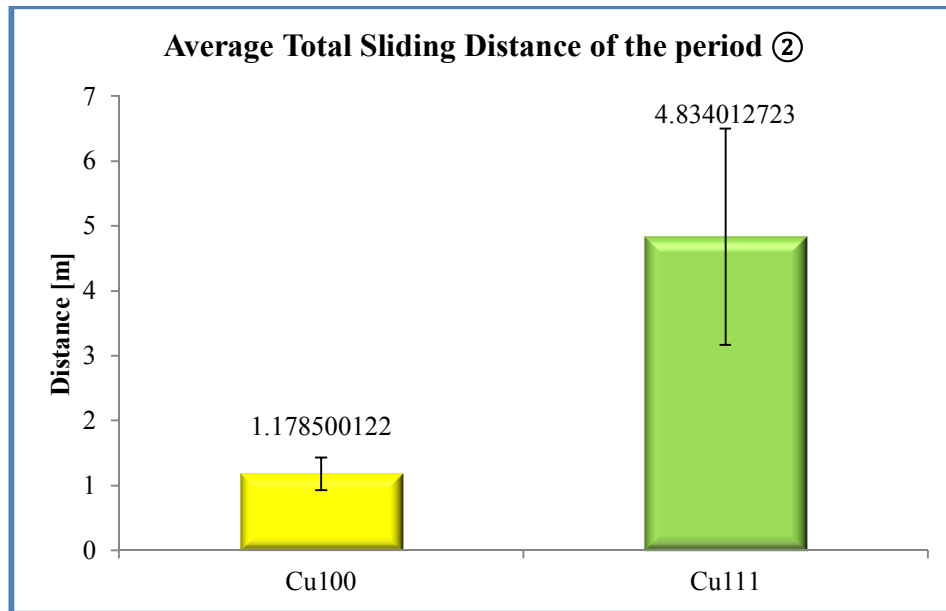
Fig.6-14. Average total sliding distance of the period ②.

6.5. Wear Mechanisms

Wear tracks were observed by using the optical and scanning electron microscopes mentioned above.

The worn-through test showed the two different layers in **Figs. 6-15** and **6-16**. From the scanning electron micrographs, there were debris build-up and grooves were detected around the wear track edges. On the unveiled surface of the silicon wafer, remained copper film was detected as shown in **Fig.6-17**.

The wear tracks with the film layer remaining were observed as shown in **Figs. 6-18** and **6-19**. Micrographs of the wear tracks reveal pores due to breaking of local films.

Fig.6-15. Optical micrographs of wear tracks. Cu100 trial 1 (left) and Cu111 trial 1 (right). The micrographs were measured in 500 of magnification.

Fig.6-16. Scanning electron micrographs of wear tracks. Cu100 trial 1 (left) and Cu111 trial 14 (right). The micrographs were measured in 20 kV of acceleration voltage; the magnifications of them are 2000 and 3000 for left and right ones, respectively. The bars in the micrographs shows different areas: red bar is the coated surface area, black one is the boundary, and the green one is the wear track.

Wear mechanisms are explained following periods ① through ④ as detailed in **Fig.6-4**. In period ①, the sample surface and its counterpart could not be in contact because of the wear-in process of the outer layer of the surface such as an oxide layer. After the outer layer was removed, the two surface materials were in contacted. This indicates the start of period ②. The surfaces of every wear track that sustained its copper film layer contain grooves as shown in **Figs. 6-15** and **6-16**. The grooves on the surface indicate that abrasive wear occurred on the surface of contact between the sample and counterpart. There were other behaviors noticed in this step. The figures mentioned above show broken films. The splits expanded to the interface located between the film and the substrate. The lump of the copper film was detached from the substrate. Period ③ started when Cu debris was dominant in the wear track. The debris built-up induced fluctuation of friction coefficient as shown in period ③ of **Fig.6-4**. During the successive period, the debris was ground to a small size or smeared on the surface of substrate. As the detached materials were removed from the contacted area, the substrate was unveiled. This state is period ④. In this, the small amount of the smeared copper layer affected the friction behavior as shown in **Fig.6-17**. As the wear continued, the contact between the silicon wafer and the bearing ball was concretely occupied. In brief, the wear mechanism is the mixture of abrasion and cracking.
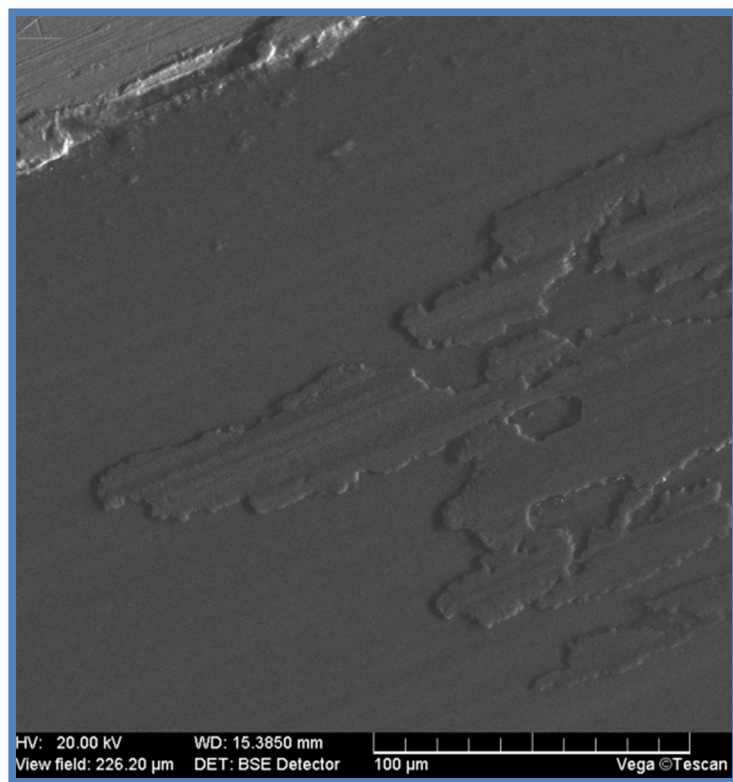
Fig.6-17. Smeared copper film layer in the wear track. This micrograph is taken on the sample Cu111, trial 2, 20 kV of acceleration voltage, and 1000 magnifications.
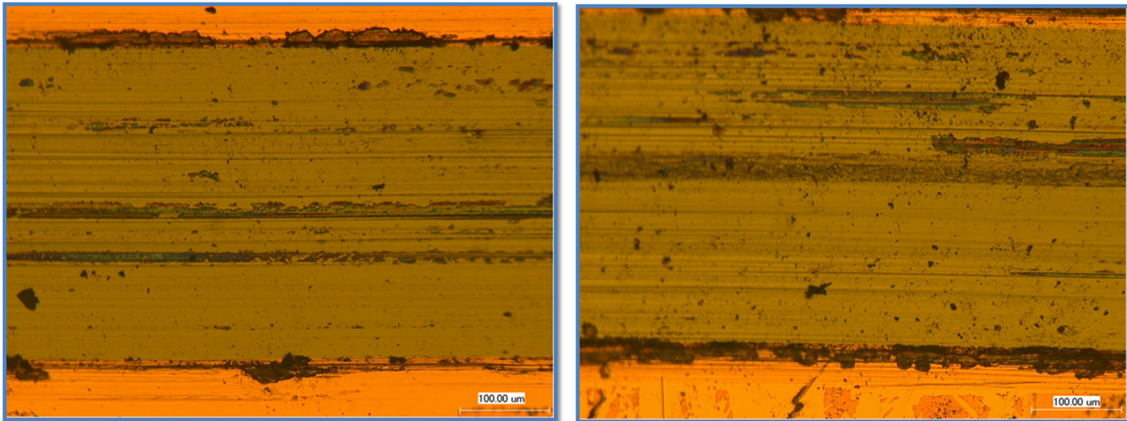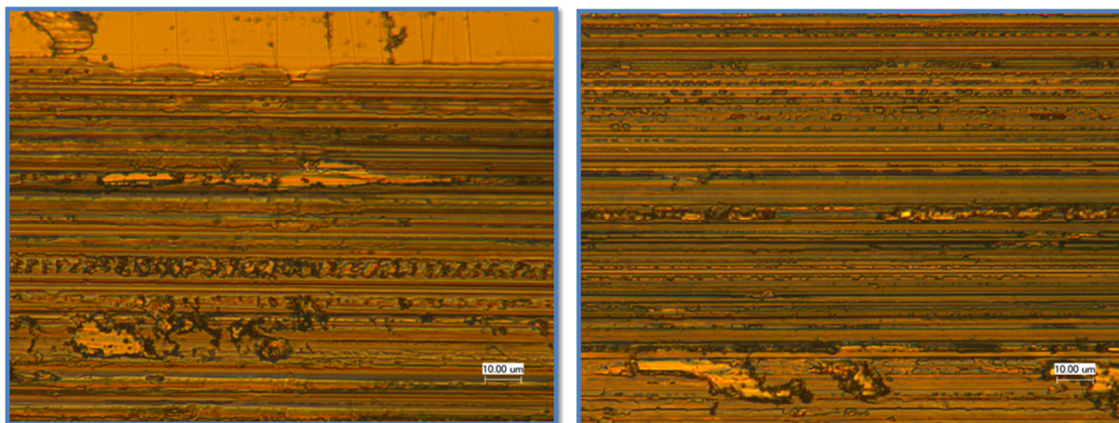

Fig.6-18. Optical micrographs of wear tracks. Cu100 trial 7 (left) and Cu111 trial 7 (right). The micrographs were measured at 2000 magnifications.
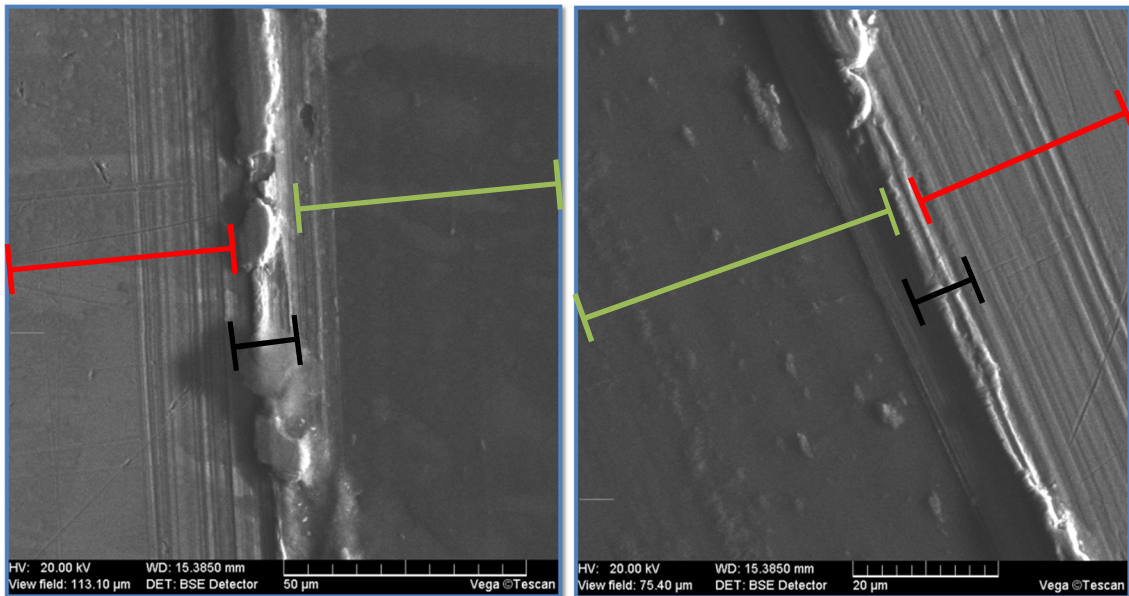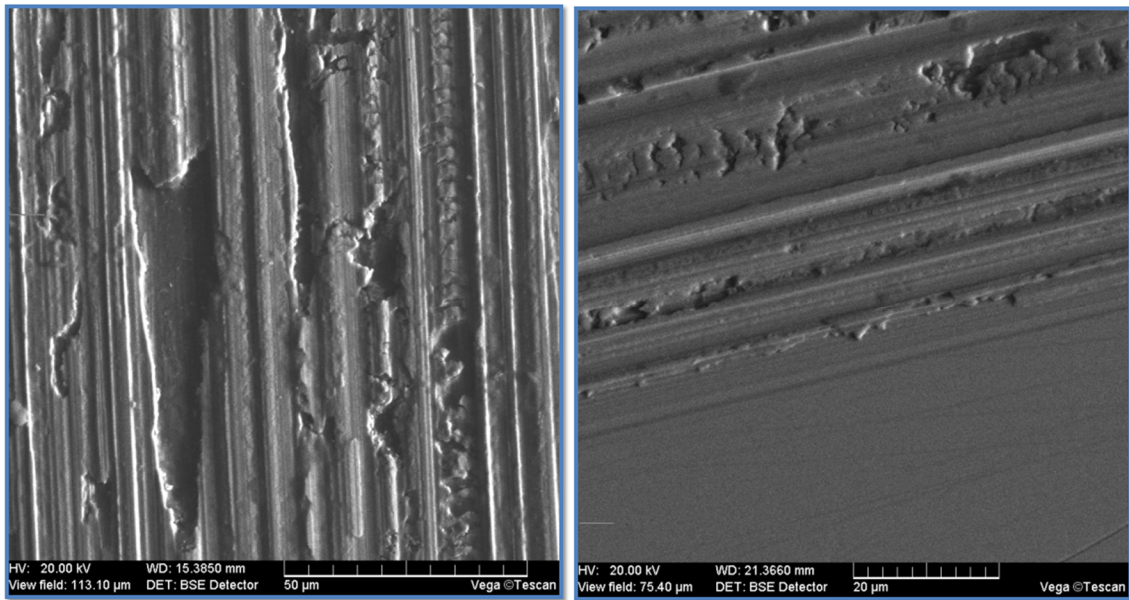
Fig.6-19. Scanning electron micrographs of wear tracks. Cu100 trial 7 (left) and Cu111 trial 3 (right). The micrographs were measured in 20 kV of acceleration voltage; the magnifications of them are 2000 and 3000 for left and right ones, respectively.

6.6. Summary

In this chapter, the single crystal copper films made by the physical vapor deposition method were evaluated in terms of tribological behaviors. Results showed that the crystal orientation has no effects on friction or wear. The nano-twinned structures, on the other hand, improved the wear resistance in comparison with other crystal structures.

CHAPTER VII

CONCLUSIONS AND FUTURE RECOMMENDATIONS

7.1. Conclusions

This research studied surface properties of three advanced materials for the purpose of reinforcing the gun barrel's performance. Thermal examination was conducted on different sized AuNPs. Tribology and corrosion experiments were carried out on the surface of microarc oxidation coating on magnesium substrate. Nano-twinned copper film was examined by tribotests.

There are three findings in this research:

1. AuNPs have size dependency in their thermal behavior. It was found that the amount of heat flow and energy was decreased with the increase in surface-to-bulk ratio. The melting temperature of the AuNPs decreased with the increase in particle size.

2. Microarc oxidation coatings of magnesium showed an increase in friction coefficient, decrease in wear rate, and increase in corrosion resistance. The parameters such as roughness and hardness had no dominant effects on friction and wear.

3. Nano-twinned copper film showed increased wear resistance. The wear mechanisms were described as a combination of abrasion and fatigue wear.

In gun barrel reinforcement, heat dissipation is expected to be enhanced by coating AuNPs on the outer surface of a gun barrel. Wear resistant materials, such as microarc oxidation coatings and nano-twinned films proven to be effective in increasing wear resistance. They are potentially good candidate in gun barrel and projectile.

7.2. Future Recommendations

Future recommendations lie in two areas, surface characterization and applications. Specially recommended items are listed in the following:

1. The precise value of thermal parameters is needed. For the DSC-TGA analysis, the heat flow and energies were calculated and compared. The energies for phase change could be calculated if the thermal parameters, such as heat flow and energies targeting merely phase change of the sample, are provided.

2. Tribotesting should be conducted on other materials and coatings in order to standardize coatings applied to weapons.

3. The materials needed to be tested in the projectile firing conditions. The conditions of a gun barrel in fire are high temperature, high gaseous pressure, high speed, and low sliding distance.

4. The applications have not been carried out in practice. It needs several processes in applications such as designing and modeling.

7.2.1. Potential applications

7.2.1.1. Coating the outer surface of a gun barrel

The present research found that the thermal properties of nanoparticles are effectively modified by their size. It is proposed that using nanoparticles could be effective in heat dissipation system of a gun barrel. Nanoparticles can work as miniscule cooling fins.

The fundamental conduction and convection equations are shown in equations (7.1) and (7.2). From the two equations, $\dot{Q}$ is heat flux, k is a thermal conductivity, A is a section area, T_1 and T_2 are temperatures of inside and out surfaces, h is a convection coefficient, T_s is the temperature of the convection surface, and T_f is the bulk temperature of the fluid. **Fig.7-1** shows the simplified barrel wall transfer comparing the coated surfaces with the uncoated surfaces. The coated surface is expected to increase the surface area (A) and the conduction coefficient (k). For the coated area, if nanoparticles were coated with the sintering method and the nanoparticle coatings were shaped as semi-hemispheres, the surface area is increased twice. For the bulk state gold and iron, thermal conductivities are 318 and 80.4 W/mK, respectively. Additionally, the thermal conductivity of nanoparticles was reported to increase higher depend on the particle sizes [60]. The nanoparticle coating system expects the conduction and convection enhancement even though the convection coefficient is regarded as constant.

$$\dot{Q} = -kA\frac{T_1-T_2}{d} \tag{7.1}$$

$$\dot{Q} = hA(T_s - T_f) \tag{7.2}$$
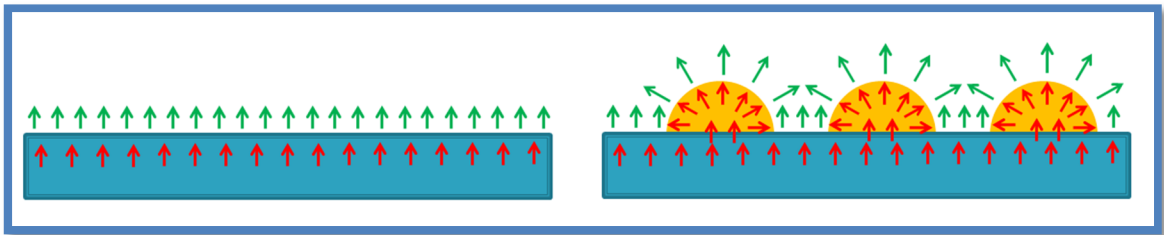
Fig.7-1. Illustration of heat transfer of a gun barrel wall: without coating (left) and coated by AuNPs (right).

This cooling system should be disputed. Firstly, whether or not the deformation mechanism caused by the thermal expansion can be facilitated should be considered. Secondly, the maximum temperature of the gun barrel's outer surface should be lower than nanoparticle temperature of fusion.

7.2.1.2. Coating the gun barrel surface

Coatings are found effective in improving wear resistance. It is attempted to coat the entire gun barrel surface (**Fig.7-2**). This coating method is an easy process. However, some coatings are brittle [48]. In explosion of propellant, the gun barrel's inner wall extends to the radial direction. This extension forces the coated wall to be deformed. This deformation results in crack propagation.

Another approach is to coat merely some areas of a barrel's inner surface. The inner barrel surface is coated partly on the area with which the projectile will contact (**Fig.7-3**).

The last method suggested is engraving the wire-shaped lining on the wall as shown in **Fig.7-4**. If the thickness of the coating's lining is enough to be geared as rifling,

rifled engraving of the coating can be used to generate the gyroscopic motion of the projectiles. In using this method, the coating materials, which force the sliding partner to have a higher wear rate, are better for the material selection.
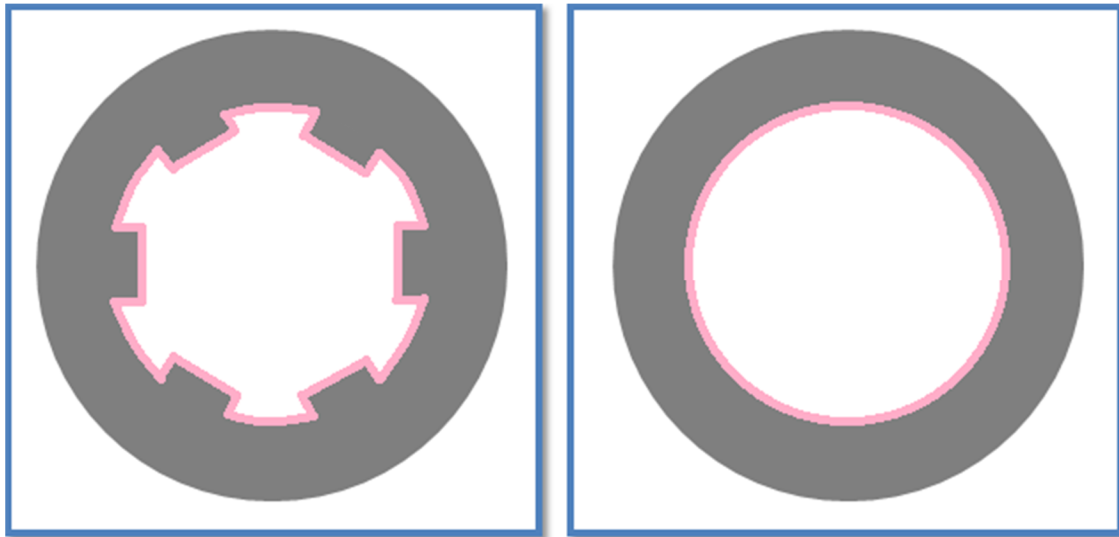
Fig.7-2. Micorarc oxidation coating on the barrel's entire inner surface: a rifled barrel (left) and smooth-bore barrel (right).
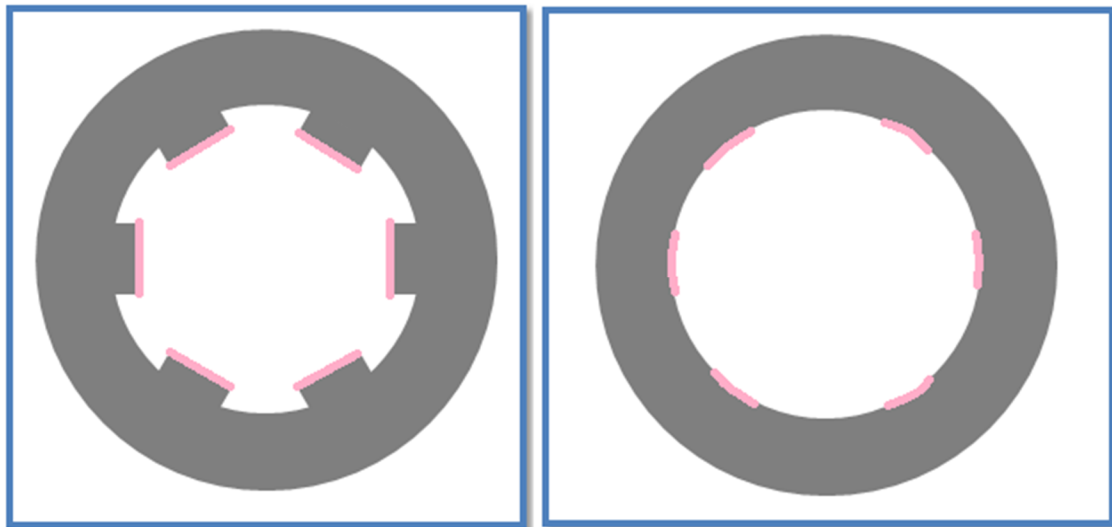
Fig.7-3. Microarc oxidation coating on the barrel's inner surface: coating on the land surface of rifled barrel (left) and coating on the some surfaces of a smooth-bore barrel (right).
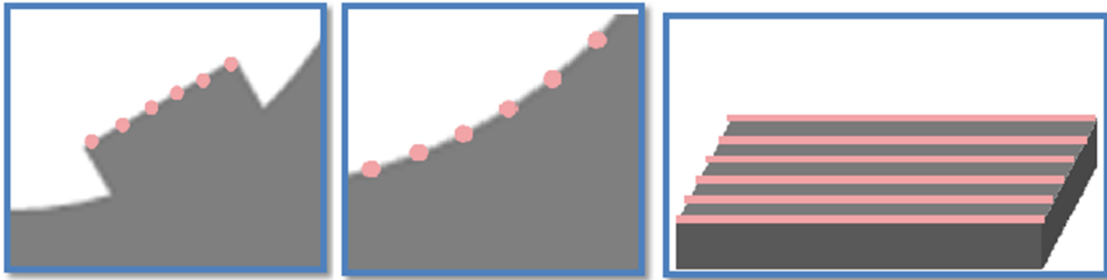
Fig.7-4. Microarc oxidation coating with wire-like shaped lining: coating on the land of rifled barrel (left), coating on the wall of the smooth-bore barrel (middle), and lining shown from above.

7.2.1.3. Non-uniform coating of the projectile surface

Coating on the surface of a projectile is considered with this material. **Fig.7-5** describes this idea. The material 1 and 2 were deposited on the surface of the projectile in accordance with the angle of rifling and the width of the rifles' land. Material 2 is more wear resistant than material 1. This design expects that the material 1 meet the lands of the rifles to wear with less deficiency of energy. Then, material 2, after the wear of material 2, functions as notches of gears. However, material 1 and 2 should be positioned in the rifle's land and rifle's groove, respectively, for the purpose of consistent ballistic behavior of projectiles.
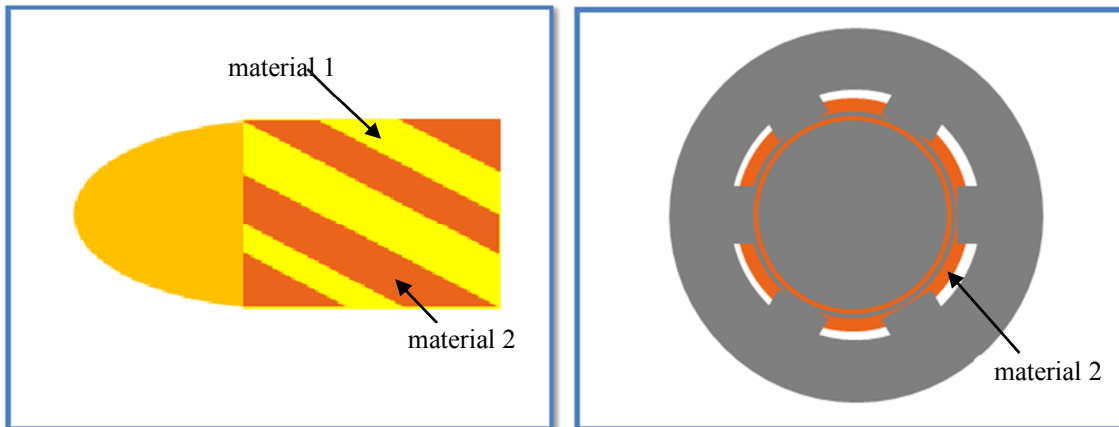
Fig.7-1. A coated projectile with different wear resistant material coating (left) and a description of a projectile geared with rifles in the barrel (right). The picture of right shows that the material 1 layers were worn out.

REFERENCES

[1] R.A. Rinker, Understanding firearm ballistics, Mulberry House Publishing, Clarksvile, IN, 2005.

[2] D.E. Carlucci and S.S. Jacobson, Ballistics-theory and design of guns and ammunition, CNC Press, Boca Raton, FL, 2008.

[3] D.H. Bacon, Ballistics of small-arms ammunition, Am. J. Phys. 12 (1944) 269 -278.

[4] T.F. Erline and M.I. Hathaway, Dispersion analysis of the XM881armor-piercing, fin-stabilized, discarding sabot (APFSDS) projectile, Tech. Rep. ARL-MR-433, Aberdeen, MD, 1999.

[5] G.F. Hull, Some aspects of physics in war and peace part I. Some applications of physics to war problems, Science 51 (1920) 221-233.

[6] V.I. Antonov, Relativistic precession of a gyroscope .1. Rotating orbit, Izvestiya Vysshikh Uchebnykh Zavedenii Fizika 4 (1981) 44-47.

[7] B. Porterie and J.C. Loraud, An investigation of interior ballistics ignition phase, Shock Waves 4 (1994) 81-93.

[8] D.K. Kim and J.H. Han, Establishment of gun blast wave model and structural analysis for blast load, J. Aircraft 43 (2006) 1159-1168.

[9] O. Baysal, Navier-Stokes analysis of muzzle-blast-type waves, AIAA J. 24 (1986) 800-806.

[10] Y. Junhui, Z. Jian, T. Hongzhi, and L. Feng, Modeling and simulation of gun barrel's lateral vibration, 2009 International Conference on Computational Intelligence and Software Engineering, Dec. 11-13, 2009, Wuhan, China, pp. 1-4.

[11] Y. Hui-jie and W. De-shi, On barrel vibration excited by accelerating projectile, J. Naval Univ. Eng. (China) 21 (2009) 12-17.

[12] P.F. Intrieri and and G.N. Malcolm, Ballistic range investigation of sonic-boom overpressures in water, AIAA J. 11 (1973) 510-516.

[13] K.S. Kumar and M.S. Dipietro, Ballistic penetration response of intermetallic matrix composites, Scripta Metallurgica Et Materialia 32 (1995) 793-798.

[14] G. Dyckmans, N. Ndompetelo, and A. Chabotier, Numerical and experimental study of the impact of small caliber projectiles on ballistic soap, Journal De Physique Iv 110 (2003) 627-632.

[15] D.V. Balandin, N.N. Bolotnik, and W.D. Pilkey, Capabilities of helmets for preventing head injuries induced by ballistic impacts, Shock Vib. 11 (2004) 547-562.

[16] J.Y. Zhang, N. Yonganandan, F.A. Pintar, Y. Guan, and T.A. Gennarelli, Experimental model for civilian ballistic brain injury biomechanics quantification, J. Biomech. 40 (2007) 2341-2346.

[17] V.S. Matveev and G.A. Budnitskii, Materials for protection from ballistic injury, Fibre Chem. 27 (1995) 147-149.

[18] F.L. Huang, H.J. Wu, Q.K. Jin, and Q.M. Zhang, A numerical simulation on the perforation of reinforced concrete targets, Int. J. Impact Eng. 32 (2005) 173-187.

[19] T.L. Teng, Y.A. Chu, F.A. Chang, and B. C. Shen, Penetration resistance of reinforced concrete containment structures, Ann. Nucl. Energy, 32 (2005) 281-298.

[20] C.Y. Tham, V.B.C. Tan, and H.P. Lee, Ballistic impact of a KEVLAR((R)) helmet: experiment and simulations, Int. J. Impact Eng. 35 (2008) 304-318.

[21] G.A. Holmes, J.H. Kim, W.G. McDonough, M.A. Riley, and K.D. Rice, A detailed investigation of the mechanical properties of polybenzoxazole fibers within soft body armor, J. Mater. Sci. 44n (2009) 3619-3625.

[22] D.K. Kankane and S.N. Ranade, Computation of in-bore velocity-time and travel-time profiles from breech pressure measurements, Defence Sci. J. 53 (2003) 351-356.

[23] E. Petitpas and B. Campion, Crack propagation in a gun barrel due to the firing thermo-mechanical stresses, J. Press. Vess.-T. ASME, 125 (2003) 293-298.

[24] C. Jinrong, W. Runsheng, and S. Limin, Research on failure mechanisms of gun barrel, Proceedings of the First International Conference on Maintenance Engineering, 2006, pp. 1051-1054.

[25] R.S. Montgomery, Muzzle wear of cannon, Wear 33 (1975) 359 - 368.

[26] O. Botstein and R. Arone, The microstructural changes in the surface-layer of gun barrels, Wear 142 (1991) 87-95.

[27] I.A. Johnston, Understanding and predicting gun barrel erosion, Tech. Rep. DSTO-TR-1757, 2005 (Edinburgh, South Australia).

[28] P.J. Cote and C. Rickard, Gas–metal reaction products in the erosion of chromium-plated gun bores, Wear 241 (2000) 17-25.

[29] J.H. Underwood, G.N. Vigilante, and C.P. Mulligan, Review of thermo-mechanical cracking and wear mechanisms in large caliber guns, Wear 263 (2007) 1616-1621.

[30] Y. Hwang and S. Deng, Applying neural networks to the solution of the inverse heat conduction problem in a gun barrel, J. Press. Vess. 130 (2008) 1-8.

[31] M.J. Adams and H. Krier, Unsteady internal boundary-layer analysis applied to gun barrel wall heat-transfer, Int. J. Heat Mass. Tran. 24 (1981) 1925-1935.

[32] P.J. Conroy, Gun tube heating, Tech. Rep. BRL-TR-3300, Aberdeen, MD, 1991

[33] H.L. Lee, Y.C. Yang, W.J. Chang, and T.S. Wu, Estimation of heat flux and thermal stresses in multilayer gun barrel with thermal contact resistance, Appl. Math. Comput. 209 (2009) 211-221.

[34] G.W. Stachowiak and A.W. Batchelor, Engineering tribology, Elsevier, Burlington, MA, 2005

[35] D.A. Rigney, Viewpoint set on materials aspects of wear - introduction, Scripta Metallurgica Et Materialia 24 (1990) 799-803.

[36] P.J. Blau, The significance and use of the friction coefficient, Tribol. Int. 34 (2001) 585-591.

[37] Iv. Kraghels, Calculation of wear rate, J. Basic. Eng-T. ASME 87 (1965) 785-790.

[38] M.A. Moore, A review of two-body abrasive wear, Wear 27 (1974) 1-17.

[39] P.L. Hurricks, Some metallurgical factors controlling adhesive and abrasive wear-resistance of steels - Review, Wear 26 (1973) 285-304.

[40] M. Roy, Elevated temperature erosive wear of metallic materials, J. Phys. D Appl. Phys. 39 (2006) R101-R124.

[41] K. Kato, Classification of wear mechanisms/models, P. I. Mech. Eng. J-J. Eng. 216 (2002) 349-355.

[42] R.D. Jones and A. White, Jane's guns recognition guide, Smithsonian, New York, 2008.

[43] Department of the Army(ed.), FM 3-33-68 crew-served machine guns, 5.56-mm and 7.62-mm, Headquarters, Department of the Army, Washington, DC, 2008.

[44] H.X. Xu and M. Kall, Modeling the optical response of nanoparticle-based surface plasmon resonance sensors, Sensor Actuat. B-Chem. 87 (2002) 244-249.

[45] R. Asthana, A. Kumar, and N.B. Dahotre, Materials processing and manufacturing science, Elsevier, Burlington, MA, 2006

[46] M.B. Karamis, A. Tasdemirci, and F. Nair, Failure and tribological behaviour of the AA5083 and AA6063 composites reinforced by SiC particles under ballistic impact, Compos. Part A-Appl. S. 34 (2003) 217-226.

[47] R. Darin, M. Flinders, A. Angela, C. Raymond, C. Jamnes et al., Effect of microstructure and mechanical properties on the ballistic performance of SiC-based ceramics, Ceram. Eng. Sci. Proc. 27 (2007) 85-96.

[48] W.S. Rosset and M.j. Audino, Advanced gun barrel materials and manufacturing technology symposium-overview and perspective, 2006, Mat. Manuf. Process, St. Michaels, MD, pp. 571-572.

[49] Y. Hoshi, M. Naoe, and S.I. Yamanaka, Thin film coating techniques on wires and inner walls of small tubes via cylindrical magnetron sputtering, Electr. Eng. Jpn. 103 (1983) 73-80.

[50] G.N. Vigilante and C.P. Mulligan, Cylindrical magnetron sputtering (CMS) of coatings for wear life extension in large caliber cannons, Mater. Manuf. Process, 21 (2006) 621-627.

[51] A.L. Yerokhin, X. Nie, A. Leyland, A. Matthews, and S.J. Dowey, Plasma electrolysis for surface engineering, Surf. Coat. Tech. 122 (1999) 73-93.

[52] X. Zhang, O. Anderoglu, R.G. Hoagland, and A. Misra, Nanoscale growth twins in sputtered metal films, JOM-US, 60 (2008) 75-78.

[53] O. Anderoglu, A. Misra, F. Ronning, H. Wang, and X. Zhang, Significant enhancement of the strength-to-resistivity ratio by nanotwins in epitaxial Cu films, J. Appl. Phys. 106 (2009) 1-9.

[54] O. Anderoglu, A. Misra, H. Wang, F. Ronning, M.F. Hundley et al., Epitaxial nanotwinned Cu films with high strength and high conductivity, Appl. Phys. Lett. 93 (2008) 083109-1-3.

[55] J. Turkevich, P.C. Stevenson, and J. Hillier, A Study of the nucleation and growth processes in the synthesis of colloidal gold, Discuss. Farday Society 11 (1951) 55-75.

[56] S.C. Mojumdar, R. Prasad, L. Sun, J.E.S. Venart, S.H. Eichhorn et al., An introduction to thermodynamic modeling, thermal analysis and calorimetry, Res. J. Chem. Environ. 13 (2009) 86-103.

[57] F. Chen, et al., Tribological behaviour of the ceramic coating formed on magnesium alloy, Plasma Sci. Technol. 9 (2007) 587-590.

[58] K. Dick, T. Dhanasekaran, Z.Y. Zhang, and D. Meisel, Size-dependent melting of silica-encapsulated gold nanoparticles, J. Am. Chem. Soc. 124 (2002) 2312-2317.

[59] P. Buffat and J.P. Borel, Size effect on melting temperature of gold particles, Phys. Rev. A 13 (1976) 2287-2298.

[60] N. Shalkevich, W. Escher, T. Burgi, B. Michel, L. Si-Ahmed et al., On the thermal conductivity of gold nanoparticle colloids, Langmuir 26 (2010) 663-670.

VITA

Name: Huisung Yun

Education:
- B.E., Mechanical Engineering, Korea Military Academy, Republic of Korea, 2005
- M.S., Mechanical Engineering, Texas A&M University, 2010

Experience:
- Graduate research assistant, Liang research group, Mechanical engineering department, Texas A&M University, January, 2009~July, 2010
- Aide de Camp, Cadets' Corps, Korea Military Academy, Republic of Korea Army, June, 2006 ~October, 2007
- Platoon leader, 15th Infantry division, Republic of Korea Army, July, 2005~June, 2006

Contact methods:
- Email Address: kmasniper@gmail.com, ar-18@hanm ail.net
- Address: 10 Tong 3 Ban 1425-1, Ju An 2Dong, Nam Gu, Incheon, 402-855, Republic of Korea